CRANFIELD UNIVERSITY

PETER KING

FORM MEASUREMENT AND DURABILITY OF MIRROR SURFACES FOR CONCENTRATING SOLAR POWER APPLICATIONS

SCHOOL OF AEROSPACE, TRANSPORT AND MANUFACTURING

PhD Thesis
Academic Years: 2011 - 2014

Supervisors:
Dr Chris Sansom
Dr Paul Comley

November 2014

CRANFIELD UNIVERSITY

SCHOOL OF AEROSPACE, TRANSPORT AND MANUFACTURING

PhD Thesis

Academic Years 2011 - 2014

PETER KING

Form measurement and durability of mirror surfaces for concentrating solar power applications

Supervisors:
Dr Chris Sansom
Dr Paul Comley

November 2014

ABSTRACT

Concentrating solar power systems currently have a high capital cost when compared with other energy generating systems. The solar energy is captured in the form of thermal energy rather than directly electrical, which is attractive as thermal energy is easier and currently cheaper to store in large amounts. It is also used directly as processing heat including desalination and water purification. For the technology to compete against other generating systems it is important to reduce the electrical energy cost to the $0.05 per kilowatt-hour level. One of the significant capital costs is the solar field, which contains the concentrators. To reduce the cost of this field, novel constructions and improvements to the durability and lifetime of the concentrators are required. Techniques for characterising the shape, durability and optical properties of such novel mirrors are the focus of this thesis.

The thesis describes the development and validation of an inexpensive, highly portable photogrammetry technique, which has been used to measure the shape of large mirror facets for solar collectors. Photogrammetry has demonstrated its versatility and portability by successful measurements across concentrating solar power sites globally. The accuracy of the technique has been validated to show a measurement capability of better than 100 µm using a large coordinate measuring machine. Measurements performed on novel thin glass mirrors and their comparison with conventional thick glass mirrors are presented, showing that the increased flexibility of thin mirrors is an important consideration during installation, but that it is possible for such novel mirrors to perform to the same level.

An ageing technique using an erosion rig to simulate sandstorms is presented which, by using climate data for Egypt, was able to investigate the effect of sand impact on the mirror surface. Little damage was seen at wind speeds of 10 m/s, typically found in an average sandstorm, however significant damage is seen at wind speeds greater than 15 m/s, which are seen during gusting winds. An attempt was made to simulate a year of exposure, corresponding to 46 hours' worth of sandstorms, over the course of a few minutes. However, the sand particles adhered themselves strongly to the mirror surface and a thick layer quickly developed, preventing further sand from impacting the surface. To simulate extended periods of time it is therefore

important to consider than there are long periods of ‘clean’ air and frequent washing of the mirrors, which prevent such a build-up occurring. To be able to simulate such periods of time it is necessary to modify equipment to incorporate such ‘clean’ air and washing phases. The mirrors exposed to higher wind speeds, with low sand mass, to simulate the gusting conditions, showed a loss of hemispherical reflectance of less than 5% and a loss of specular reflectance exceeding 14%. The greater loss of specular reflectance shows that the dominant mechanism is scattering over absorption of the light.

ACKNOWLEDGEMENTS

I would like to express my thanks to my supervisors, Dr Christopher Sansom and Dr Paul Comley for their guidance and support throughout my research.

I would also like to thank the academic and technical staff and students in the Precision Engineering Institute at Cranfield University for sharing their knowledge and time to help me in my research. Additionally I am very grateful to Arthur Hawkins for operating the erosion rig on my behalf and his time spent was very much appreciated.

My thanks to Waqar Bokhari from COMSATS Institute of Information Technology, Islamabad, Pakistan; Alberto Giaconia from ENEA, Italy; and Loreto Valenzuela from CIEMAT-PSA, Spain for kindly allowing access to their equipment and facilities for collector measurements, as well as sharing their expert knowledge and experiences.

Finally I would like to recognise the funding provided by the "*Multipurpose Applications by Thermodynamic Solar"* (MATS) and the *"Scientific and Technological Alliance for Guaranteeing the European Excellence in Concentrating Solar Thermal Energy"* (STAGE-STE) projects, which are funded under the European Seventh Framework Programme (FP7).

TABLE OF CONTENTS

LIST OF FIGURES

LIST OF TABLES

LIST OF ABBREVIATIONS

CMM	Coordinate Measuring Machine
CSP	Concentrating Solar Power
CSY	Coordinate System
DNI	Direct Normal Irradiation
ENEA	Italian National agency for new technologies, Energy and sustainable economic development
HTF	Heat Transfer Fluid
MATS	Multipurpose Applications by Thermodynamic Solar
MENA	Middle Eastern and North African
MIL	Military standard: MIL-STD-810G
PSA	Plataforma Solar de Almería
PV	Photovoltaic
RMS	Root Mean Square
SEGS	Solar Energy Generating Systems
SEM	Scanning Electron Microscope
STAGE-STE	Scientific and Technological Alliance for Guaranteeing the European Excellence in Concentrating Solar Thermal Energy
VSHOT	Video Scanning Hartmann Optical Testing

1 INTRODUCTION

The estimated global power use is 140,000 TWh per year (BP, 2011; EIA, 2009), with over 90% generated from non-renewable sources such as fossil fuels and oil. The price of oil has increased by a factor of 5 in the last 50 years (BP, 2011) and will continue to increase as the supplies are exhausted. The energy incident on the Earth from the Sun is 1 billion TWh per year (Schnatbaum, 2009) which is much larger than the power used globally. So if only a small proportion of this energy is harvested, this would be enough to provide power globally.

Solar energy does not adversely affect the environment by pollution. The ideal locations for installation of solar energy harvesting facilities are commonly in areas of desert or similarly hostile environments for life, where the Sun's radiation is strongest. For example, much of central and northern Africa has a yearly solar total irradiation of approximately 2,300 kWh/m^2 compared with much of Europe at only 1,000 kWh/m^2 annually (SolarGIS, 2014). Facilities in these locations can therefore significantly increase the economic value of land, which would otherwise be unused.

The majority of large scale solar energy harvesting uses concentrating solar power (CSP) plants. These operate by using mirrors to concentrate large areas of sunlight onto much smaller areas, achieving concentration ratios of up to 1:1500 (Kalogirou, 2004), in order to produce high temperatures which can then be used to generate electricity by conventional generator methods, including the use of steam turbines. The heat energy contained can also be stored using molten salts for later use when the solar power reduces towards the evening and into the night (Herrmann, Kelly and Price, 2004). This storage is an important advantage of CSP plants over photovoltaic (PV) plants where there is typically no storage and the output of such a PV plant is limited to daylight hours.

CSP plants have four main configurations which are: parabolic troughs, linear Fresnel collectors, central towers and parabolic Stirling dishes, as shown in Figure 1.1 (IEA, 2010). All of these configurations require precise mirror surfaces to ensure that the solar energy is extracted as efficiently as possible. A major factor in this efficiency is the quality of the focus that can be achieved by the collector surface,

where the tighter the focus the higher the temperature that can be reached for a given area of collector.

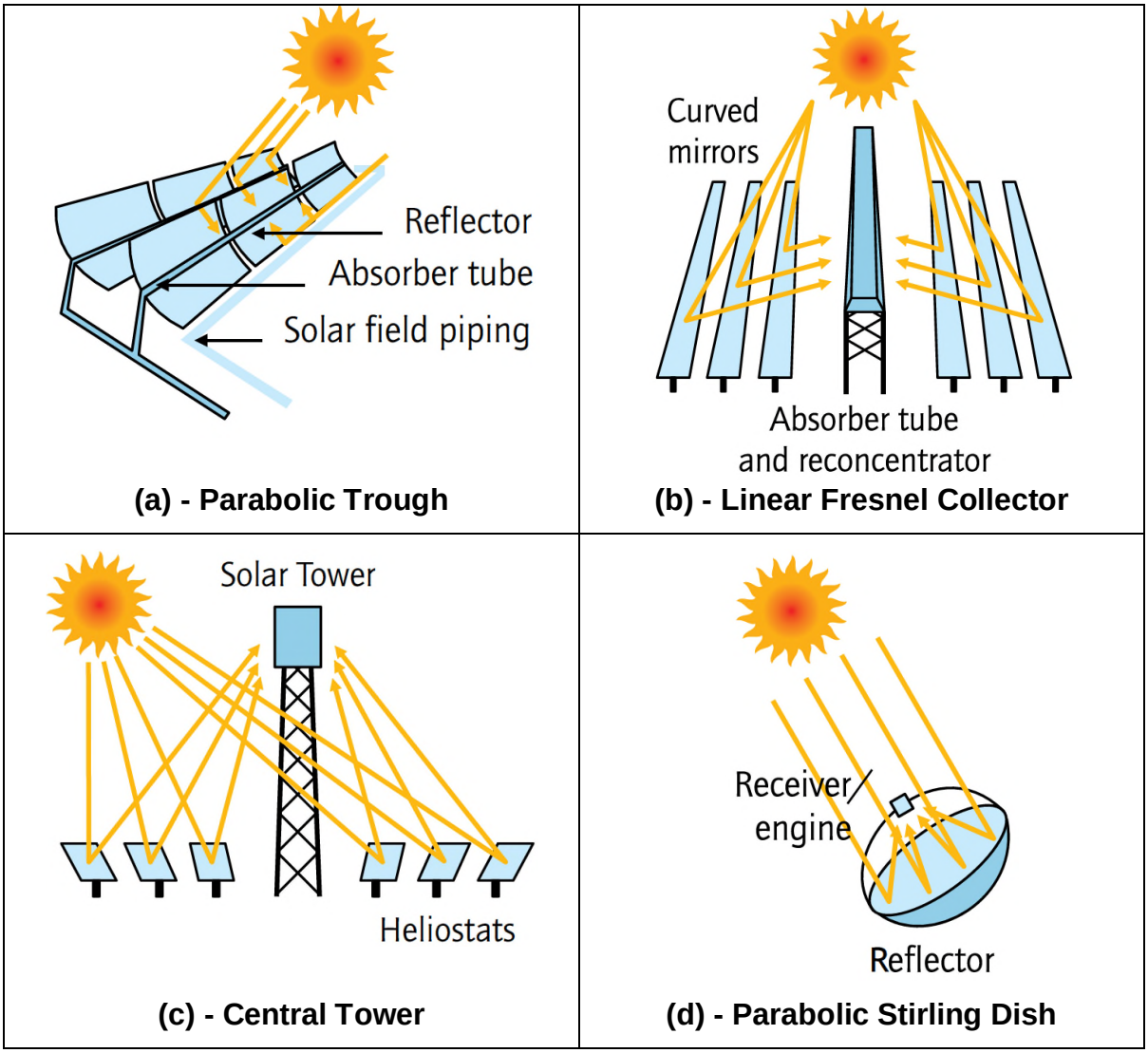

Figure 1.1 - CSP main configurations

To compete with other forms of energy it is important to reduce the cost as much as possible to attract investment and push the technology forward. A major cost of CSP is in the collector field, often consisting of hundreds of mirrors spread over square kilometres of land. Two ways to reduce the cost of these mirrors are to change their construction and to improve their lifetime. This thesis details techniques which may be used to characterise the mirrors both in their shape and optical properties and how these change over time. The particular CSP technology that this project investigates is that of the parabolic trough surfaces.

The shape is ideally a parabolic one whose focus is at an absorber tube, however this shape will deviate due to stresses from the support structure, the weight of the mirror itself and external factors such as wind and thermal effects. It is important to understand and predict how this shape changes with such factors over time and throughout a normal day, as this has a large impact on the efficiency, lifetime and ultimately how cost effective the power plant is.

The optical properties of the mirror are also crucial in determining the efficiency, as these determine the proportion of the light that is specularly reflected and so the amount of heat that can be obtained. The amount of light that is reflected is directly linked to the surface roughness of the mirror. If the surface is very rough then the light will be refracted at varying angles and this will then lead to diffuse scattering. If the surface is smooth then there will be consistent refraction and so the reflection angle will be constant and all of the light will be directed toward the focus as shown in Figure 1.2.

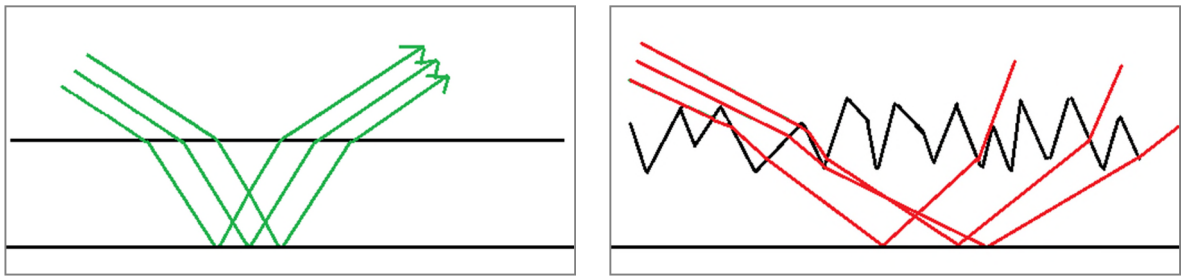

Figure 1.2 - Scattering from a rough surface

The locations that are best suited for CSP plants, when considering the solar radiation potential, are usually hot and dry environments where sand and dust cover the ground. This sand and dust will be picked up by the wind and will impact the surface of the mirrors, causing surface damage and a build-up of dirt. This surface damage is in the form of an increase in surface roughness as the mirror ages and any dirt present on the surface will absorb the sunlight, reducing the amount of reflected light. Samples of CSP mirrors were obtained and techniques were developed to characterise their form and to artificially age the mirrors by sand impact. Photogrammetry was validated against a large coordinate measuring machine, the accuracy of which is traceable to the International Organization for Standardization standard 10360-2 (ISO, 2009). This enables the use of

photogrammetry, a highly portable technique, to measure fully installed mirror facets on the CSP plant with a traceable uncertainty in its measurement results.

The mirror facets tested are innovative in that they are thin mirror panels, 1 mm thick, mounted onto a 3 mm parabolic pre-formed backing structure which has a number of 21 mm reinforcing ribs built in as shown in Figure 1.3. Typical mirror panels that are currently in operation are 3 to 4 mm thick glass with painted back layers and the parabolic shape is held by the steel support structure of the trough. This change to thin mirrors with the formed backing structure should reduce the distortions seen caused by the weight of the thick glass. Additionally as the entire mirror is fully attached to the back structure any breakage of the glass will not shatter the whole panel, only introduce cracks. The thicker glass panels are typically held by 4 to 6 support pads, offering little strength to the mirror if a crack occurs and the whole panel may shatter.

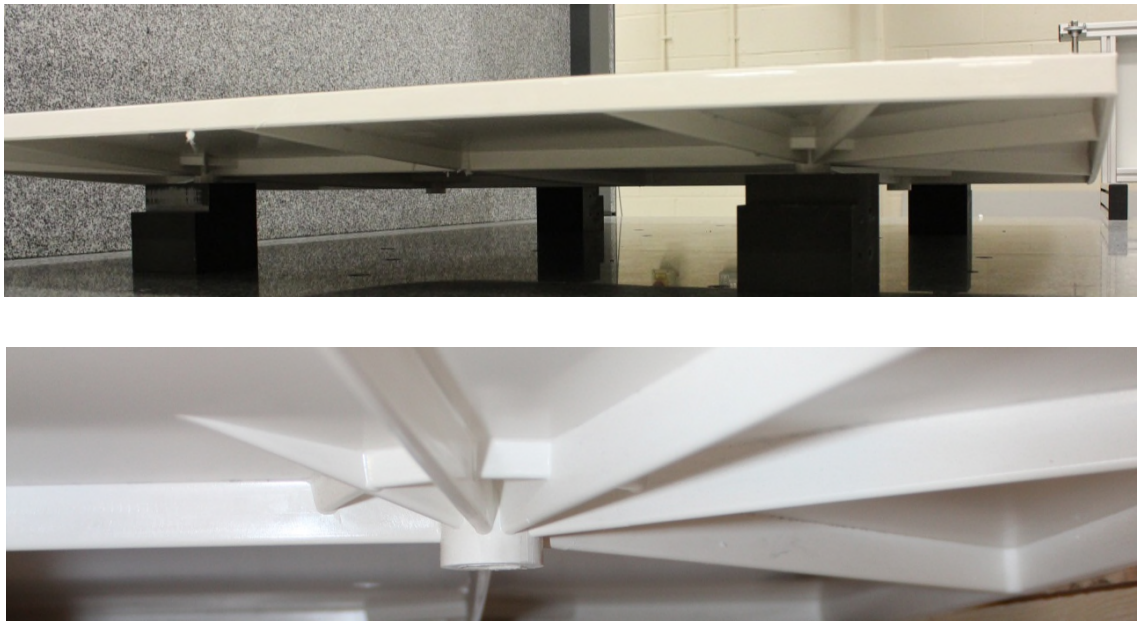

Figure 1.3 - Mirror support structure

The parabolic trough arrangement (Figure 1.1a) consists of large parabolic curved mirrors, each up to 12 m long with 6 m apertures, usually aligned along a north-south axis in large commercial solar thermal power plants. They may also be aligned east-west in experimental facilities or where a more stable energy output through the year is desired. These large mirrors are rotated around this single axis by motors attached to their support structure allowing the troughs to track the Sun’s position as it moves

through the sky from the east to the west. These mirrors concentrate the sunlight to a linear focus where an absorber tube is placed, through which a heat absorbing fluid is pumped. The absorber tubes are connected along loops covering many parabolic troughs so that the fluid can be heated up from typically 290°C up to 390°C or higher. This hot fluid may then be pumped to a storage tank where it may be kept at high temperature until it is needed to generate electricity at the turbine.

An approximation to the parabolic trough, with a focus to a linear absorber, is used in linear Fresnel collectors (Figure 1.1b) where the parabolic mirror is split into many smaller plane or slightly curved mirrors to make up a Fresnel arrangement. This has the advantage of not requiring large single facets of precisely curved mirror, therefore may be more suitable to smaller scale domestic solar energy harvesting such as solar cookers (Bokhari, 2011).

The central tower arrangement (Figure 1.1c) uses a large number of mirrors called heliostats; these may be flat or slightly curved and can vary in size from a few square metres to over 100 m^2 each (Pitz-Paal, Botero and Steinfeld, 2011). They are mounted on foundations in a large field and each heliostat individually tracks the sun by using two rotational axes per mirror and they reflect the light onto a central receiver tower where the fluid is heated.

The parabolic Stirling dish systems (Figure 1.1d) contain individual parabolic dishes, which also track the sun on two axes, and focus the light onto a receiver containing a Stirling engine at each focal point, generating electrical power at each dish.

The second chapter of the thesis is a literature review covering details of the different configurations of collectors; further details on the specific parabolic trough configuration; methods for assessment of surface form including photogrammetry; damage caused by sandstorms and the effect on glass. The third chapter details the methodology for the development of the techniques and its use both in the laboratory and at CSP sites. This contains information regarding the photogrammetry technique as well other techniques which were considered for use. Ageing using an erosion rig and damage assessment by reflectance measurement and microscopy are also covered. The results and discussion of the measurements and ageing tests are contained within chapter 4 dealing with both laboratory measurements and outdoor

site tests. The thesis concludes with chapter 5 detailing the findings and further work which may be possible, to build on the work done within the thesis.

2 LITERATURE REVIEW

This literature review details the current state of CSP technology with a focus on the parabolic trough configuration. This is the most common type and is the main target of the characterisation techniques reviewed. Potential form measurement techniques are reviewed to determine which have been used and their advantages and disadvantages. Finally, work on the effect of sandstorms on glass is investigated and important parameters which require consideration are explored.

2.1 Overview of CSP

The Sun is a blackbody which radiates according to Planck's Law (Rybicki and Lightman, 2008)

$$B(\nu,T) = \frac{2h\nu^3}{c^2}\frac{1}{e^{\frac{h\nu}{kT}} - 1} \quad \textbf{(2.1)}$$

where $B(\nu,T)$ is the power emitted normal to the surface per unit solid angle per unit frequency ν at temperature T, h is Planck's constant, c is the speed of light in a vacuum and k is the Boltzmann constant. This may then be used to derive the Stefan-Boltzmann law for the total energy radiated over all frequencies per unit area, P_s, such that

$$P_s = \frac{2\pi^5 k^4}{15c^2h^3} \times T^4. \quad \textbf{(2.2)}$$

Using 5778 K as the effective temperature of the Sun according to NASA (2013), and the values for the fixed constants, the power output of the Sun is 63.2 MW/m^2. The flux, F, arriving at the Earth's atmosphere at a distance, d, of 1 Astronomical Unit is

$$F = \frac{4\pi R_s^2 P_s}{4\pi d^2} = 1{,}368\ W/m^2, \quad \textbf{(2.3)}$$

where R_s, the radius of the Sun, is 696,000 km (NASA, 2013) and the mean distance between the Earth and Sun is 149.6x10^6 km.

This power density is reduced by a number of factors before arriving at the surface of the Earth. One of these is that the surface of the Earth is spherical in nature, and as such the area over which a beam of a certain width will fall varies according to the cosine of the incidence angle. Another consideration is the absorption of energy as the light passes through the atmosphere, which will depend on the distance over which the light travels through the atmosphere. These factors lead to the northern and southern latitudes receiving less power than the equatorial regions: the incidence angle is higher and there will be a thicker atmosphere for the light travel through. This leads to a maximum of around 1000 W/m^2 at the surface when the Sun is normal and unobstructed.

Sunlight therefore is a key source of renewable energy with annual energy averages of up to 2,500 kWh/m^2 across parts of Central Africa and in excess of 3,500 kWh/m^2 in South America. The energy supply is also more predictable when compared to other renewable sources such as wind, as shown by the direct normal irradiation (DNI) maps of the world such as Figure 2.1 (SolarGIS, 2014).

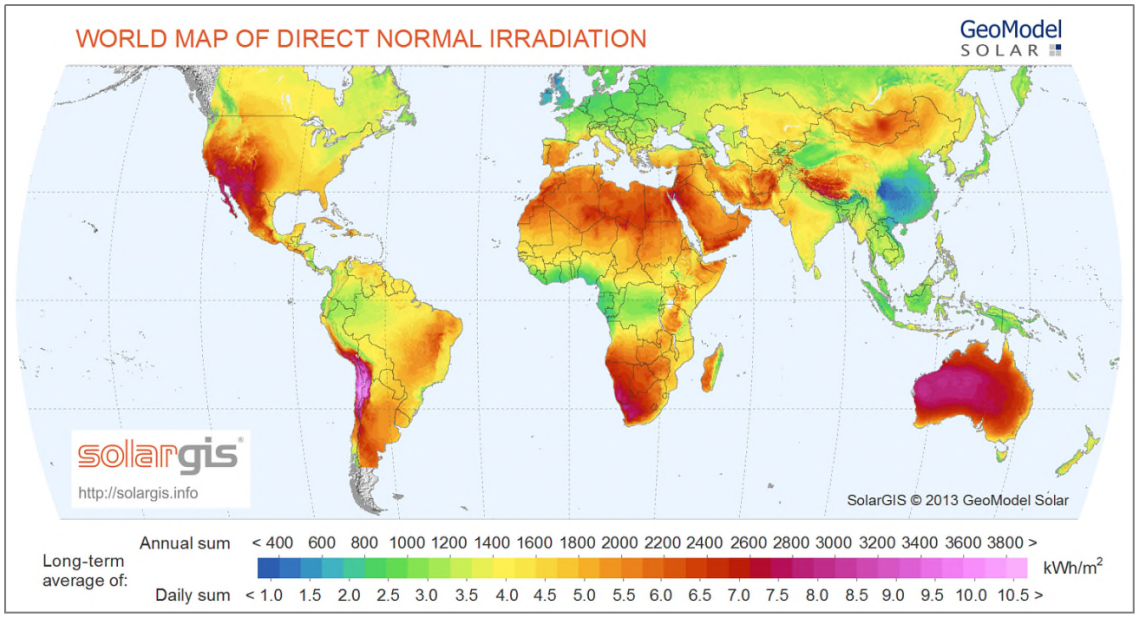

Figure 2.1 - World Map of Direct Normal Irradiation

In Figure 2.1 the DNI increases from blue to pink with the highest radiation levels located in Chile. Such maps are used to plan the position of solar power plants with many of the Middle Eastern and North African (MENA) countries either actively pursuing or beginning to invest in solar energy generation (Ibrahim, 2011; Jablonski et al., 2012; Patlitzianas, 2011; Trieb et al., 2012; Trieb, Müller-Steinhagen and Kern, 2011; Tsikalakis et al., 2011). Countries such as India and Pakistan also have high DNI and there is research into utilising the available solar energy on domestic and community levels, where access to clean water and the ability to heat food is limited (Bokhari, 2011; Mahavar et al., 2012; Panwar, Kaushik and Kothari, 2012).

To utilise the energy contained within sunlight it must be converted into a useful form, such as heat or electricity. There are currently two main methods used for this conversion, the first a conversion from sunlight to electricity is photovoltaic (PV) and the second a conversion from sunlight into heat is solar thermal. PV uses the photoelectric effect, where electrons contained within a semiconductor, typically silicon based, are liberated when excited by incoming photons. These electrons are then free to flow and cause a current. Solar thermal uses the energy contained within the photons to heat up light-absorbent materials, the heat from which is then extracted by fluid flow which can be stored, used as heat or converted to electricity through turbines. Concentrated solar power is where a large area of sunlight is captured and then focussed onto a smaller area where the absorbent material is placed. By focussing a large area, sunlight concentration factors of 1:2000 and more (Kalogirou, 2004) and temperatures higher than 1000ºC (Forsberg, Peterson and Zhao, 2007) can be achieved.

The focussing nature of CSP implies that this method of solar energy harvesting requires a high level of direct solar radiation, whereas PV panels are able to collect diffuse light from all directions. This limits the efficient use of CSP to those countries with high DNI and few overcast days, with locations subject to higher cloud cover able to use PV systems (Quaschning and Muriel, 2001). PV panels are self-contained in that the useful energy in the form of electricity is generated within the panel making them highly modular and allowing their use

in small domestic and large power plant applications. CSP however, is more suited to the large scale power plants due to a need for storage and power generation systems, although small scale CSP systems are becoming available for domestic use such as solar cooking (Bokhari, 2011).

The larger commercial solar thermal power plants have been in operation for over 25 years since the first of the Solar Energy Generating Systems (SEGS) plants were built in the Mojave Desert in 1984 (Quaschning and Muriel, 2001). Nine such power plants were built there in the period 1984 to 1991 providing over 350 MW of electrical power to the grid in total.

Other such power plants have been and are being built at a rapid rate across many of the 'sun-belt' countries, where the DNI is highest. Spain is the current European leader in this area of renewable energy with approximately 2.3 gigawatts of operational solar thermal power plants (ProtermoSolar, 2014). The majority of these are of a parabolic trough design. In MENA countries, the World Bank has given funding to Morocco towards the development of CSP plants with a total power of about 500 MW (World Bank, 2012a). Egypt and Tunisia also have World Bank proposals for their own CSP plants (World Bank, 2012b, 2012c).

2.2 Types of collector

All concentrating solar thermal power plants follow the same principles in that they use a large area of highly reflective material, usually back silvered glass, though other materials such as silvered or aluminized polymers have been investigated (Fend et al., 2003), to concentrate the sunlight onto smaller receiver areas. The arrangement of the reflective surfaces and receivers varies between four main configurations (Barlev, Vidu and Stroeve, 2011; Kalogirou, 2004) which are: parabolic trough, central receiver tower, linear Fresnel and parabolic Stirling dish.

The most common of these configurations is the parabolic trough design, consisting of rows of large parabolic troughs with liquids, the so called "working

fluids", flowing along the absorber tubes to the power plant. At the power plant the thermal energy from the working fluid is extracted to generate steam which drives a turbine and generates electrical power. The working fluid may also transfer the thermal energy collected at the solar field to a thermal storage medium, which is kept in thermally insulated tanks. This stored thermal energy may be used later to generate power when the direct solar radiation is not available.

According to the US Department of Energy, the first use of solar power engines was in the 1860s by August Mouchet, who used parabolic troughs to heat water to produce steam. The parabolic trough was first patented in 1907 with the first power plant built by Frank Schuman in Egypt in 1912. This plant had a power of 73 kW and was used to pump water from the Nile to irrigate the surrounding fields. The first commercial electrical grid connected parabolic trough power plants (SEGS) were built in the 1980s in California and are still in operation today reaching temperatures of up to 395°C using a synthetic oil as the working fluid. An example of a parabolic trough plant is shown in Figure 2.2 with a typical collector and support shown in Figure 2.3 (Solar Millennium, 2012).

Figure 2.2 - AndaSol plant in Spain

Figure 2.3 - Large parabolic trough and support structure

The second most common configuration is the central tower or central receiver, see Figure 2.4 (Torresol Energy, 2012). This design consists of a large number of flat or slightly concave mirrors, the heliostats, attached to individual base supports. These base supports move the mirrors in two axes so that the

sunlight from each mirror is focused at a common point. At this focal point there is a central tower containing an absorbent material and a steam generator capable of producing steam at high temperature and pressure. The steam can be generated either directly in the receiver (in this case liquid water is fed into the receiver and converted into steam as it passes through the receiver) or in a heat exchanger (in this case the fluid circulating through the receiver is not water) thermally fed by the hot fluid delivered by the receiver. This steam may be sent directly to the power block where electricity is generated or it can be stored to generate electricity later. At present, commercial solar thermal power plants with central receiver use water or molten salt in the receiver. Other working fluids (e.g. supercritical CO_2) are being investigated at experimental level. The tower may have a cylindrical receiver, and so have heliostats located on all sides as is the case in Figure 2.4; or all heliostats can be on the side opposite to the sun, e.g. north for northern hemisphere, and the absorber may be on a single side only.

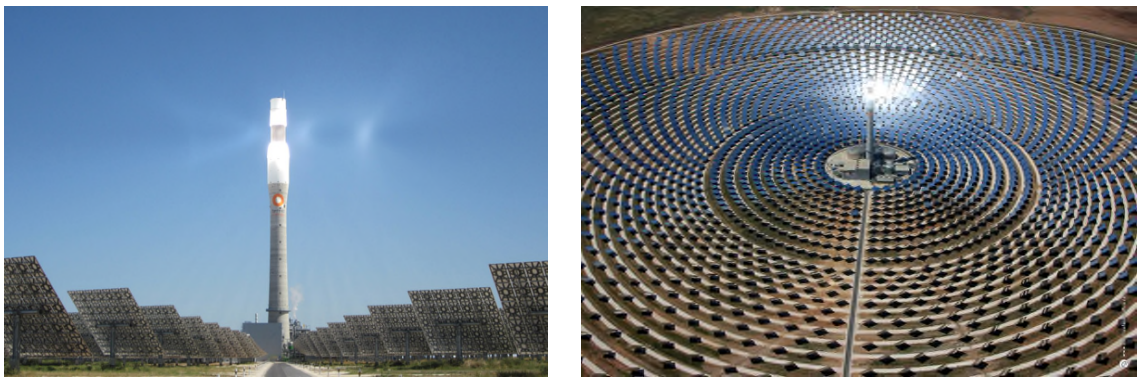

Figure 2.4 - GemaSolar central tower plant, Spain

A disadvantage of central tower systems is the need for individual two-axis control of the heliostats whereas the parabolic troughs move only along a single axis. As the size of the mirror field increases there is a greater need for higher accuracy heliostat mirrors, as any small slope errors present will lead to larger focal errors over the greater distances.

As the light passes through the air it is absorbed and scattered by dust particles that are present. By increasing the amount of atmosphere through which the light must pass after reflection, more light will be lost before it reaches the

absorber. There are also shading and blocking losses, caused by close packing of the mirrors needed to minimise land use (Ali, 1990). Shading losses occur when part of one mirror is not exposed to the Sun due to being in the shadow of an adjacent mirror. Blocking losses occur when the light that is reflected from one mirror strikes the back of an adjacent mirror instead of reaching the tower. Such effects vary according to the position of the Sun throughout the day and the time of year. Complex mathematical models are used to optimise the field layout in order to produce the most power, whilst minimising land use.

Advantages of heliostats include the single receiver to minimize thermal losses in transport of fluid, high concentration ratios and the manufacture of flat mirrors rather than highly curved parabolas. Due to the high concentration ratio, very high temperatures are possible at the absorber leading to more efficient power generation.

Figure 2.5 - Areva Solar Linear Fresnel collectors

The third design is the linear Fresnel, see Figure 2.5 (Areva Solar, 2012). These are currently used in smaller applications than the parabolic trough and central tower. This design uses many strips of flat or nearly flat mirror arranged such as to reflect the light from each strip onto an absorber tube in the same manner as the parabolic trough. For linear Fresnel collectors, the mirrors do not need to be in a parabolic arrangement in space. The mirrors each have their own parallel axes of rotation and can be collectively controlled to track the sun.

As the strips can be flat, while still achieving a good focus, the mirror cost is reduced when compared to the large precisely curved parabolic trough facets. As the strips are not generally curved to reduce cost, the concentrated light will have a minimal focal size determined by the width of the strip. It is therefore common to have a secondary concentrating mirror above the receiver in order to capture more of the light. An important issue in building linear Fresnel collectors is the need to avoid shading between strips of mirror as they lie in the same plane and are angled. This can be avoided by either raising the height of the absorber tube, or by spacing the strips. However a balance must be met between covering a high percentage of area, important towards noon, and attempting to capture low angle sunlight, occurring during mornings and evenings. Tracking the Sun can be relatively simple with a linear Fresnel system by mechanically linking the strips at their ends and using a single linear driver to rotate all the mirrors together. The positioning of the mechanical link and speed of the driver can be calculated so as to rotate the strips at the correct speed to track the Sun. However, large Fresnel collectors usually have independent drive units for each mirror strip. With the reduced cost of the mirrors compared to other solar collectors, linear Fresnel systems are important in developing countries where small scale and domestic power and heat generation is required. Compact and rooftop examples of such systems are becoming common for cooking, water heating and industrial process heating (Bokhari, 2011; Snidvongs, 2012).

The fourth type is the Stirling dish, where a large parabolic dish tracks the sun on two axes. Such dishes may be up to 25 m in diameter (Burgess et al., 2009) with a 500 m^2 collection area. The sunlight is focused by the dish onto a receiver where it is converted into electricity by a Stirling engine. These are efficient with the high thermal gradients available from the high concentration ratios. Although these dishes are not widely used in power plants they have the highest efficiency of the four types converting over 30% of the solar energy into electricity (Taggart, 2008).

A disadvantage of this type of system is the direct conversion from thermal to electrical energy. This means that there is no heat storage capability

commercially available and that the system cannot generate electricity after sunset, as is the case for other CSP systems. Energy storage therefore currently relies on expensive batteries, however investigation of thermal storage options are currently underway in several R&D projects. Two axis tracking is also an added complexity and expense, especially when the dishes are large. The requirement for a large paraboloid, typically made from mirror sections is also more expensive than either the single curve parabolic trough shape or the nearly flat mirrors of a linear Fresnel.

An advantage of this system is the ability of having decentralised power generation in that each dish is a self-contained unit generating electricity. Other systems which rely on central power plants, such as the parabolic trough systems and central receiver, are larger by nature and the power generated typically is fed into a network grid.

Technology	**Parabolic Trough**	**Central Tower**	**Linear Fresnel**	**Stirling Dish**
Concentration ratio	30-100	300-1500	30+	500-1500
Temperature (°C)	100-400+ (HTF dependent)	150-800	100-300	500-1500
Electrical power range (MW)	0.05-100	0.5-100	0.05-100	0.025-100
Capital cost ($/kW installed)	2300-3972	4000+	Lower	12,578
Operating cost per unit ($/kWh)	0.012-0.02	0.034	Lower	0.21
Land use (m^2/MWh/yr)	3.2	4.6	1.8	4.15

Table 2.1 - Comparison between CSP technologies

There are a number of key parameters in a comparison of these current leading technologies. The concentration ratio is a measure of the ratio of the collector aperture and the receiver size. Higher concentrations indicate higher temperatures and efficiencies. The different requirements of electricity

generation against process heating means that the temperatures achieved within the receivers are important. The electrical power which may be generated by a typical power plant along with the installation and running costs against land use, are important economic factors.

A comparison between the technologies was done by Nixon et al. (2010) to determine the optimal technology for installation in north-west India. Table 2.1 details some of the factors considered.

2.3 Parabolic trough

The parabolic trough configuration is made from a three main elements: the collectors, the absorbers and the power plant. The collectors and their absorbers are typically manufactured in units, which are then placed together end on end to form rows, with the absorber tubes of two such rows connected in a single loop to increase the heating of the flowing liquid medium. The whole layout can measure 1.5 km square with a total collector area over 500,000 m^2 as at the AndaSol 1 plant in Spain (Herrmann and Geyer, 2002). The troughs are positioned in either a north-south direction, tracking the sun as it moves east-west; or in an east-west direction, tracking the sun north-south. Each orientation produces a different amount of energy dependent on the time of year, making the positioning of the troughs a situation dependent parameter (Kalogirou, 2004).

The trough collectors can vary in size depending on the intended use, with aperture sizes typically from 0.5 m up to 6 m wide and focal lengths up to 2 m for large power plants. They may also be much smaller if the requirements are for less energy and cost. The larger troughs are built in 12 m long units which may then be organised together into rows stretching many hundreds of metres in length. Each collector is made up from many rectangular curved facets approximately 1.5 m in size, with layers of glass, silver and either paint or a composite backing. The glass used is a low-iron variety manufactured by a float process, having the advantage of reducing the surface roughness to less than 1 nm root mean square (RMS). The float process, described by Yates and Duffy

(2008), is one where the glass raw materials are mixed and heated to 1500°C. Then a quantity of the mixture, depending on the required glass thickness, is fed onto a bath of molten metal; usually tin. The glass floats on top of the tin as the two are immiscible and forms an even thickness layer. As the glass cools it is pulled out of the bath where it is cooled further gradually and is annealed, it is then cut to size. This type of glass is the most common type of flat glass and is usually found in domestic windows and so the process is well understood and the resultant panel thickness can be tightly controlled.

The thickness of the glass layer varies between manufacturers but it is typically in the region of 3 to 4 mm. However, thin-glass mirrors are being developed with a thickness nearer to 1 mm, which reduces the amount of glass needed but requires more substantial and rigid supporting structure. A thin layer of silver is deposited on the back surface of the glass layer to form a mirror with reflectances in excess of 90% dependent on the thickness of the glass. If the glass is thick its mechanical strength is good enough to keep the parabolic trough shape once it has been formed and multiple paint layers at the back are sufficient to protect the thin silver layer of the mirror panel so it is resistant to outdoor conditions. However if the mirror is thin, additional supporting structure is needed so an adhesive layer is applied followed by a backing panel. This panel will add strength to the more flexible thin glass and hold the mirror to its required shape. The support panel for a Ronda 1 mm glass is made from a 3 mm thick polyester resin with glass fibres so as to have thermal expansion properties close to that of glass to reduce any stresses due to thermal effects. For additional support there is a pattern of ribs on the reverse of the panel surrounding the attachment points. The completed trough facets may then be attached to the structures seen in Figure 2.3 to form the whole parabolic trough collector.

At the focal point of the collectors is placed the absorber tube, typically made from 4 m long units connected together to form a pipe the length of the collectors. The absorbers are formed from two concentric cylinders, the outside one glass and the inside one steel coated in a material which strongly absorbs solar radiation. An absorber tube produced by Schott Solar (2012) has the

following specifications. The outer glass cylinder diameter is 125 mm with an anti-reflective coating to increase the solar transmittance to >96%. The inner cylinder has a diameter of 70 mm and is coated so that the absorptance is >95%. This diameter is matched to the focal size of light, dependent on the form quality of the trough. A higher quality trough will enable a smaller diameter tube, thus providing a higher concentration ratio. To further increase the efficiency of the absorber, the space between the two tubes is evacuated to avoid convective heat loss. As the two tubes are different materials there is a difference in the thermal expansion properties of each, therefore at the ends of each tube there are expansion bellows to allow thermal expansions. These occur as the absorber tube temperature fluctuates between day and night from 70°C to over 450°C when thermal oil is used as working fluid in the solar field, which is the technology currently available for commercial parabolic trough plants.

Flowing through these absorber tubes is the heat transfer fluid (HTF), this can be a mineral oil, synthetic oil, water/steam or molten salts (Herrmann, Kelly and Price, 2004; Lupfert et al., 2001). Mineral or synthetic oil is the technology fully proven for commercial plants. Molten salts and water/steam are being investigated because these working fluids would allow higher solar field temperatures and therefore higher power block efficiencies. The HTF is chosen dependent on the temperatures which may be reached within the absorber tube and the plant requirements. With the use of molten salts it would be possible to increase the temperature at which the steam turbine runs from a limit of 390ºC with oil to over 450ºC. This in turn increases the efficiency of the Rankine cycle and thus the output of the power plant (Kearney et al., 2003). The HTF may either be immediately pumped to the turbines for use in generating electricity (this would be the case when using water/steam as a working fluid in the solar field), or it may be stored in large tanks for use during low-solar and high demand times such as the evenings (this would be the case when using molten salts in the solar field). However, in current large commercial solar thermal power plants that use parabolic trough collectors, the heat transfer fluid is synthetic oil. This oil transfers the thermal energy gained at the solar field to

either large, thermally insulated steel tanks containing molten salts as the storage medium, or to a steam generator. In the steam generator the oil transfers its thermal energy to liquid water and this water converts into superheated steam to feed the turbine, which drives an electricity generator. When discharging the thermal storage system, the molten salts transfer their thermal energy to the oil, which is then sent to the steam generator.

2.4 CSP Performance

2.4.1 Effect of mirror form on performance

An ideal CSP mirror should conform to the shape which provides the optimal focus. For a trough CSP mirror, this shape should be a perfect parabola in one direction and perfectly straight in the perpendicular one. However, this shape is never exactly reproduced and some errors will be present. The errors are local slope errors which will cause the light to be reflected away from its ideal path such that it strikes the absorber tube off-centre or not at all. The sun itself is not a point source and has approximately a 3 mrad size (Gee et al., 2010) so will itself produce dispersion. Therefore, the combination of this dispersion with slope errors introduces spreading of the focus and reduces the heating effect on the absorber tube.

It is important to reduce such errors to maximise the efficiency of the trough and this may be done as a quality assessment process during manufacture as well as when the troughs have been installed on-site. The form is principally controlled by the support structure holding the mirror facets. If this structure is inaccurately made or misaligned then this will place stress onto the mirror facets, bending and distorting their shape. These structures are measured before the facet is attached (Pottler and Shortis, 2004; Shortis et al., 2008a), adjustments are made and the mirror can then be mounted. These support structures must be manufactured to reduce the effects from thermal expansion, distortions due gravity and wind loading.

Lüpfert & Ulmer (2009) proposed that a high performance reflector should not have an RMS transversal focus deviation of greater than 15% of the absorber

diameter, which for a 70 mm tube diameter would be 10.5 mm. For an RP3-type mirror facet of focal length 1710 mm a focus deviation of 12 mm was seen. A second measure of the quality of the focus is the intercept factor, which measures the percentage of reflected rays which strike the absorber tube (García-Cortés, Bello-García and Ordóñez, 2012). Lüpfert & Ulmer (2009) found intercept factors for the RP3 inner facet to be in excess of 95%.

One of the principle causes of form deviation is the inaccurate positioning of a facet in the collector. Each 1.5 m mirror facet of the 12 m by 6 m trough is not directly attached to the adjacent facets; it is wholly supported by the support pads and fixture positions. Therefore if one of these positions is incorrect then distortions will occur. There are commonly around 4 support positions for each facet so there will also be distortions due to the weight of the mirror at these points. Also the support structure is not perfectly rigid and will bend under the weight of the mirror facets, though this can be predicted the distribution of weight will change through the day as the troughs rotate to track the sun (Pottler et al., 2005).

Errors in the form of the mirror may be reduced by either changes to the collector itself or by changes to the supporting structure. Different reflective materials and constructions may be used, for example thin films on metal sheeting or different thicknesses of glass with different backing structures, such as full panel moulds. The number of connection points between mirror and steel structure may be changed, or alternatives to steel may be found to provide a more stable structure for the mirrors. However, any method used needs to be subjected to analysis to investigate the potential gain versus any added expense, added maintenance or environmental impact from using specialised materials.

2.4.2 Effect of surface damage on performance

The amount of light that is reflected from the mirrors also depends on the surface texture. If the surface is rough from abrasion then the light that is incident on the surface will not undergo perfect reflection. Instead, the light

passes through the roughened surface of the glass and is refracted at many different angles, causing a spread of the beam. This beam scattering causes the average path length through the glass to increase meaning a higher percentage of the radiation is absorbed by the material. In addition, the remaining light will again be refracted at the glass-air interface and the beam will be subject to further dispersion after leaving the glass. This spread causes a loss in the amount of light that is incident on the receiver tube, and so a loss in efficiency. The surface texture may also include impacted particles which may stick to the surface of the glass, causing any incident radiation to be absorbed into the contaminant material.

The manufacturing process for solar mirrors produces a smooth glass-air interface due to the float process described previously; the roughness is less than 1 nm and is homogeneous across the surface. Post-installation surface damage occurs due to the harsh environment in which the troughs operate. Such environments contain high quantities of dust and sand, which is picked up by the wind and impacted upon the mirror surfaces. This is compounded by high wind speed events such as sand storms (Adjouadi et al., 2007; Bouaouadja et al., 2000; Bousbaa, 2003).

There are two main ways of reducing surface damage caused by particle impact. The first way is to deposit a hard coating onto the glass surface, which will act to reduce the damage caused by the impacts. Though this is more commonly used for front surface reflectors or polymer films (Bouquet, 1980; Brogren, 2004; Fend et al., 2003; Kennedy and Terwilliger, 2005).

The second method, in the case of parabolic troughs, involves tilting the trough so that it points vertically downwards during sandstorms. This then exposes the back surface to the sand and it acts as a barrier against the majority of the particle impacts. This is not viable for heliostats as the mirrors are supported from below and the foundations prevent the required position. In this case the mirrors are tilted so that they point vertically upwards, reducing the wind loading on them and also reducing the angle of incidence of any impacting particles. This makes them less prone to damage of the surface.

2.5 Form assessment

2.5.1 Metrology requirements

The important information to be obtained regarding the shape of the collecting mirror surface is that of the slope at each point on the surface (Huang and Han, 2012; Ulmer et al., 2009). As the surface is designed to accurately reflect light along specific paths, the slope is crucial in maintaining a tight focus and making the mirror more efficient in concentrating the solar energy. There are two ways of measuring this slope information, by either measuring the local slope at many points on the mirror surface, or by measuring the position of a large number of points and then interpolating the slope between these points. The level of slope error is typically in the region of 1 to 5 mrad (Jones, Neal and Gruetzner, 1996; März et al., 2011; Ulmer et al., 2009). In order to measure at this level with a 10 mm point spacing it is necessary measure position with an accuracy of 100 µm. It has also been found that there can be positional inaccuracies of the order of millimetres (Pottler et al., 2005), which would be measurable with an accuracy of 100 µm. Any method identified must be able to record positional data relating to where the errors occur on the mirror and to sufficient lateral resolution so as to pinpoint any likely causes for such errors, for example around support positions.

Direct slope measurement requires light to be incident on the mirror at a known angle. The slope of the mirror for any point may be calculated by measuring the trajectory of the reflected light from that point. One such method illustrated in Figure 2.6 (Knauer, Kaminski and Häusler, 2004) is deflectometry, where a reflection of a known pattern by the mirror is viewed and any distortions can then clearly be seen. The original known pattern and its distorted image can be compared and thus the mirror shape can be determined including any imperfections. This method is a whole surface one, where the slope can be measured directly for any part of the mirror surface without interpolation (Ulmer et al., 2009; Xiao et al., 2012; Zhao, 2009). The technique may also be

extended by using the absorber tube as a reference object and recording the distortions in its reflection in the mirror (Diver and Moss, 2007).

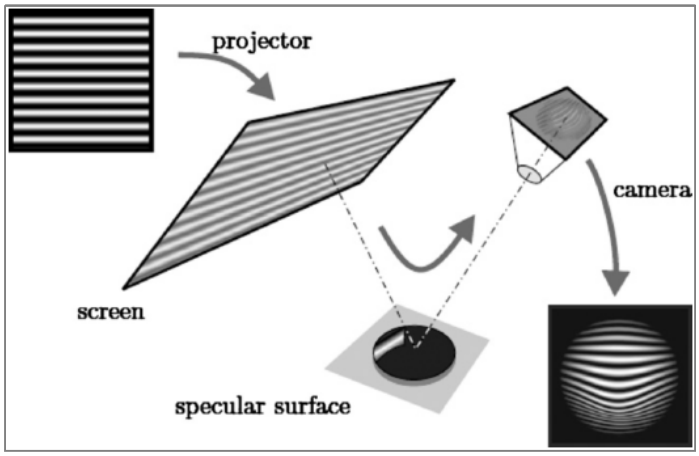

Figure 2.6 - Pattern analysis deflectometry

Applying deflectometry in this way enables its use on-site; however there is still the requirement for careful measurement of camera, object and reflector positions in order to calculate the exact slope. An indication of the approximate error can be found quickly using this technique by imaging the absorber at a large distance. For a perfectly focusing reflector the absorber tube should fill the reflector aperture. If any parts of the mirror show either objects above or below the absorber, for example the ground and sky, then these parts can be seen as in error (Diver and Moss, 2007; Prahl et al., 2013; Stynes and Ihas, 2012; Ulmer et al., 2009). This is the so called distant observer method as shown in Figure 2.7.

Figure 2.7 - Distant observer method, before (l) and after (r) correction

A second slope measurement method called Video Scanning Hartmann Optical Testing (VSHOT) (Molnar et al., 2011; Wendelin, May and Gee, 2006) uses a laser, which is fired at the mirror and reflected to form a spot on a screen as shown in Figure 2.8 (Molnar et al., 2011). With a known incident angle, by analysing the spot position, the slope for that incident point can be calculated. The laser is then moved across the mirror and the spot position is tracked allowing the calculation of local slope for the points on which the laser is incident. This method is suitable for use on reflectors where the F-number (focal length/aperture) is greater than 0.5 and less than 3, with the laser and screen typically sited at a distance of twice the focal length (Arqueros, Jiménez and Valverde, 2003; Jones, Neal and Gruetzner, 1996).

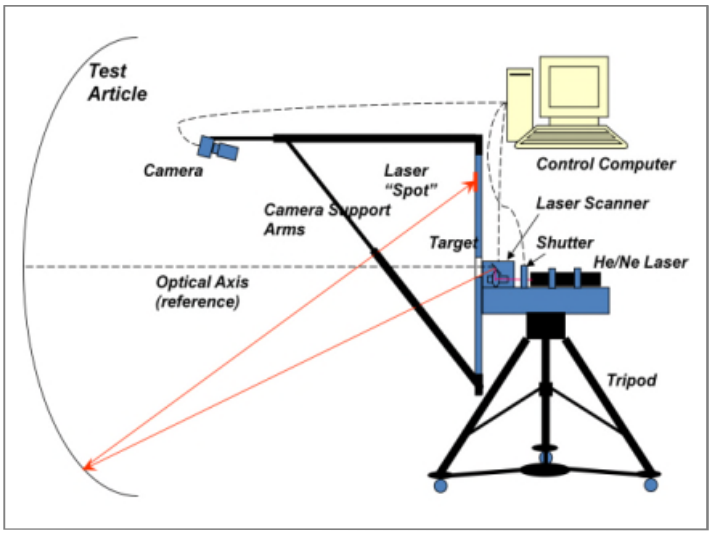

Figure 2.8 - VSHOT configuration

The results of Wendelin & May (2006) on measuring parabolic trough collectors showed large variations in the slope error from 1.5 mrad to as high as 9 mrad with an average of 4.4 mrad, which was less than the 5 mrad specification of the particular parabolic mirror under test. The accuracy of this technique is quoted as 0.1 mrad slope but is highly dependent on the accuracy of data such as the distance and the camera calibrations (Jones, 1998). A separate uncertainty analysis by Gray et al. (2010) found a higher 2-sigma uncertainty of 0.33 mrad, which is still small when compared to the expected errors found in parabolic troughs of at least 2 to 3 mrad RMS.

These slope measurement techniques do not however give information about the position where the slope error occurs. This would require a separate measurement to determine the location under investigation. However, by measuring the positions of many points directly, it is possible to determine the slope between these measured points and its deviation from the ideal shape.

For indirect measurement of the slope using interpolation between points, there are many established techniques for surface point metrology. However, as the surface to be measured is very large, highly reflective and aspheric, these techniques are complicated by the need to account for these facts.

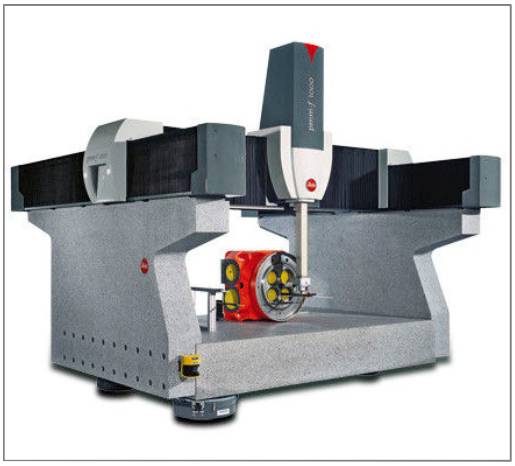

Figure 2.9 - Large CMM

Figure 2.10 - Laser Tracker

Coordinate metrology using a coordinate measuring machine is one of the most straightforward contact techniques. There are a wide variety of sizes and configurations. The bridge configuration CMM shown in Figure 2.9 (Leitz, 2012) offers higher levels of precision. The technique involves touching a machine driven probe onto the surface, where the probe location is known by the CMM by measurement transducers along the three orthogonal axes. The CMM can build up a point map of locations on the surface of the mirror where the probe was touched. Due to the large measurement volume and contact probing this method is ideal for measuring large, aspheric surfaces and is independent of the reflectance of the surface. The surfaces are glass and as such are resistant to deformation under the small forces applied by the probe head. A disadvantage with this measuring technique is the requirement for a highly stable test environment for the highest accuracy measurements at such large

sizes. This can include large granite beds and temperature controlled laboratories. Such machines would not be suitable for measurements on-site as they are not portable. As one of the most accurate tactile large scale measuring machines, they can be used to validate other techniques in a laboratory environment. When used in an assembly process the CMM can be programmed for repeated measurements on different parts, allowing quality control. A portable version may consist of an articulated arm (Hexagon Metrology, 2013), which is fixed to a stable mount and must be manually used by an operator. Such articulated arms lack the accuracy of the traditional CMMs.

Another method, shown in Figure 2.10 (Hexagon Metrology, 2012a), is the use of a laser tracker (Estler et al., 2002), which has a hand held probe with a retro-reflective target which can also be placed anywhere on the mirror surface. To measure the location of the probe the laser tracker base moves a laser beam such that it continuously strikes the target and is reflected back to the base. The tracker records both the distance to the probe and the angular positions of its head. Using this data it then reconstructs the 3D position of the probe as it is moved. By knowing the dimensions of the probe and the position of reflection, an offset is applied to give the point at which contact is made on the surface. This method is widely used as a portable technique and as such may be suitable for measuring parabolic troughs. However the equipment is expensive and can take time to set up for accurate measurements. There is also the need for the probe to be physically moved over the surface of the mirror, which may prove difficult and time consuming over such large surfaces and heights.

A further method is laser interferometry. This uses a laser beam which is split into two paths, one of which is reflected off a high quality reference artefact such as an optically flat mirror, with the second beam reflected off the object to be measured. These two beams are then recombined and will interfere due to a difference in their path lengths. The pattern which is formed from this interference shows the difference between the two surfaces. This method requires the reference mirror to be of high optical quality and would be further

complicated due to the aspheric trough shape and the size of the mirrors themselves.

2.5.2 Photogrammetry

Photogrammetry has been shown to be suitable for use with the large parabolic trough collectors and has been used for other large surfaces as well, such as gossamer spacecraft (Burgess et al., 2009; Pappa, Jones and Black, 2002; Pottler et al., 2005). It is highly scalable from very fine detail over a small surface area of interest, up to whole mirror troughs and support joints. The technique is highly portable, needing only to attach targets to the mirrors and to take photographs with a conventional camera, which may be later processed.

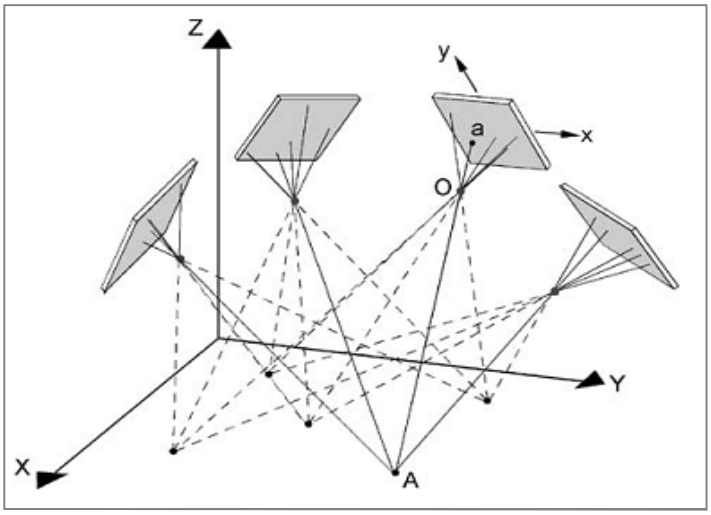

Figure 2.11 - Photogrammetry geometry

The general principle of photogrammetry is to place a number of high contrast or retroreflective targets on a surface and to then take a large number of photographs of these surfaces from many different angles, as shown in Figure 2.11 (Estler et al., 2002). These photographs are then fed into a computer and software is used to analyse the different perspectives in the images and to determine the relative positions of the target points. High resolution images should be taken so that the targets may be clearly distinguished and that the central point of the target may be found by the centring algorithm within the software. The angle from the surface being photographed should be sufficient to

allow triangulation, but not too great as to produce highly elliptical target images as this will reduce their effective size and they may not be identified correctly.

The targets themselves should have a high contrast against their background to enable the centring algorithm to be accurate to the sub-pixel level (Shortis, Clarke and Short, 1994). This may be achieved through printed black and white targets, or with retroreflective targets, both of which utilise the camera flash (Shortis and Johnston, 1997). Printed targets give the flexibility of varying sizes, patterns and point density as well as being disposable and cheap. However, nearly all photogrammetry work that has been done at high accuracy has used the retroreflective targets, giving the highest possible contrast against their background. While printed targets may be suitable for use and achieve an acceptable accuracy, retroreflective targets to date appear to be higher accuracy and more widely used.

In calculating the positions of the target points the software must determine the precise location of the camera for each photograph based on the variations between each image. It is therefore necessary for the software to be calibrated for the inner optics of the camera and any lens distortions that may be present. This means that the camera must have a fixed zoom level and focus for each image and the camera should be of good quality with stable and configurable optics and should not rely on autofocus features.

The calibration procedure involves taking photographs of a known calibration grid of around 100 points from positions surrounding the grid, including at least one photograph with the camera rolled 90 degrees around its axis. This enables the photogrammetry software to calculate any distortions that would not appear if the camera is kept in the same orientation, and determine correction parameters which may then be applied later to the measurement photographs to improve the accuracy of the final results.

A second calibration method is available called field calibration. If there are enough points in the project the software can adjust the distortion parameters to improve the point positions and reduce the error between photographs, without

the need for a separate grid. This has the advantage of calibrating with the camera set up that is used and the conditions under which the photographs were taken. With the grid calibration there is a chance that the camera settings, for instance focus could move between test photographs and the calibration photographs.

The parameters calculated during the camera calibration are the exact focal length f, the radial distortion and the decentring distortion. The radial distortion is radially symmetric around the principal point, that which describes the centre of the lens. A point that is found to be a radial distance r from the principal point must be corrected by an amount dr such that the corrected x and y components are

$$x_c = x \times (1 + dr) \quad \textbf{(2.4)}$$

$$y_c = y \times (1 + dr) \quad \textbf{(2.5)}$$

where

$$dr = K1 \times r^2 + K2 \times r^4 + K3 \times r^6 \quad \textbf{(2.6)}$$

Where $K1$, $K2$ and $K3$ are the radial distortion parameters calculated by the software.

The decentring distortion is much smaller than the radial lens distortion but is necessary for the highest accuracy. This describes the offset from ideal of the principal point, such that the correction applied in x and y are

$$dp_x = P1 \times (r^2 + 2x^2) + 2 \times P2 \times xy \quad \textbf{(2.7)}$$

$$dp_y = P2 \times (r^2 + 2y^2) + 2 \times P1 \times xy \quad \textbf{(2.8)}$$

respectively, where $P1$ and $P2$ are the decentring correction parameters also calculated within the software.

Photogrammetry is a well-used technique for measuring systems from aerial photography down to industrial metrology. It has been used for other large

mirror structures such as in the construction of the 25 m wide 500 m^2 SG4 parabolic dish at the Australian National University (Burgess et al., 2009). In this case a convex jig to be used in forming the parabolic shape was placed on the ground with many retroreflective photogrammetry targets attached. The photographs were taken from around 30 m in the air from a crane and a precision of around 0.2 mm was achieved over the 25 m dish. This is a precision ratio of 1:175,000 and would correspond to less than 10 µm over a 1.5 m trough facet. A 1.2 m square mirror facet from the dish was also assessed using photogrammetry; in this case the targets were projected rather than being physical retroreflective or contrast targets. Due to the reflective nature of the mirror the back surface of the facet was used. Though this leads to a reduction in the cost of targets and the ability to use a large number of targets, the resolution of the projector will limit the quality of each target and affect the accuracy of the centring algorithms. Additionally this rear surface assessment would only be satisfactory if the surface directly corresponds to the front surface of the mirror and there is no underlying support structure or reinforcement.

Another application of photogrammetry to large mirror structures is that of the 5 m diameter ultra-light inflatable 'Gossamer' spacecraft (Pappa et al., 2002). Retroreflective targets were attached to the mirrors and four cameras were used in parallel rather than a single moving camera. Due to limitations in digital camera technology at the time of measurement, the precision obtained was 1:28,000 at best.

Photogrammetry has also been extensively used by for applications ranging from model verification of parachutes (Shortis et al., 2007) to the measurement of the lengths of fish (Cappo, Harvey and Shortis, 2006) for stock and life monitoring and underwater habitats (Shortis et al., 2008b), showing its portability, flexibility and independence of laboratory conditions for measurement results.

2.6 Surface damage assessment

2.6.1 Ageing by sand impact

Regions of high DNI have high levels of intense solar radiation, which may cause the ground to be drier, dustier and have little vegetation. As these regions are the ideal areas for locating solar power plants it is important to consider what impact this environment will have on the performance over extended periods. These regions are often subject to sand and dust storms on a regular basis and these storms can move large amounts of particles through the air at speeds high enough to damage surfaces. As the sandstorms are regular and can be intense the cumulative effect over years of sand particles striking the collector surfaces will lead to a build-up of damage. This in turn leads to a decrease in performance of the power plant. Therefore there is the need carefully consider the durability of the materials used, a study by Bousbaa et al. (2009) on a vehicle windshield after two years in Algeria showed damage causing a decrease of 34% in optical transmission.

An analysis done by Wada & Watanabe (1987) showed that the hardness ratio between the sand H_s and the glass H_g is important in determining the glass erosion characteristics. When $H_s/H_g \gg 1$ then inelastic deformation occurs resulting in radial and lateral cracking. The lateral cracks are parallel to the glass surface originating from the impact site. When these lateral cracks intersect with one another and extend to the surface of the glass this will result the surface flaking away. If, however, the ratio $H_s/H_g < 1$ then the particles will not penetrate the surface and no lateral cracking will occur. Madjoubi & Bousbaa (1998) found mean value ratio of 1.585 for Saharan sand and soda-lime glass, concluding that lateral cracking is the primary damage mechanism. The size of impact cracks on the glass surface increases with the kinetic energy and shape of the impacting particles. Kinetic energy is dependent on the square of the impact velocity and the mass of each particle (Adjouadi et al., 2007).

When light meets a boundary between two media it can be reflected or refracted. Refraction at a boundary between two isotropic media is governed by Snell's Law. This states that refraction depends on the angles of incidence, θ_i, and refraction, θ_r; and the refractive indices of the first medium, n_1, and the second medium, n_2 given by $sin\theta_i / sin\,\theta_r = n_2/n_1$ (Hecht, 1974). Through the undamaged approximately planar surface, the light will refract predictably and consistently over the whole surface. However, when impact sites and cracks are introduced, this will change the angle of incidence, thus changing the angle of refraction. This in turn causes the light to travel through the glass on different paths causing scattering. At the glass-air interface approximately 4% of the light is immediately reflected so this light will also be scattered by varying incidence angles. The scattering reduces the light reaching the absorber, leading to losses in the energy gathered.

The typical particle composition of sandstorms is important in determining the type of damage which will occur when the mirrors are exposed for long periods of time. The physics of sandstorms has been investigated by Bagnold (1941) and calculations were done based on effects such as gravity, wind and air resistance in order to determine the likely composition.

According to Bagnold (1941) there are three mechanisms for the transport of particles in a fluid, namely suspension, saltation and creep. The air resistance that decelerates a moving particle will depend primarily on its size and shape. Generally, smaller particles have lower air resistance; therefore if the particle is falling it will fall at a reduced rate and achieve a lower terminal velocity than larger particles. If the upward air currents are greater than this terminal velocity the particle will be carried upwards in the air thus becoming suspended. Such particles can be classed as dust and define a lower limit on sand particle size.

For larger particles there are two means by which movement can occur. This may be either by direct pressure from the wind or by impact of other moving particles. If larger particles are not moved by either mechanism then these are not classed as sand particles, setting an upper limit on sand size. If the particles are moved along the ground but do not rise into the air they are said to be

creeping. Saltation occurs when the particles are lifted into the air and their trajectory is such that they will return under gravity to the ground. These particles may travel large distances at relatively low height and it is these particles which will cause the damage to mirror surface and so are of interest in ageing processes.

A study by Hubert & Kalman (2004) on pickup and saltation velocities found that for sand particles of sizes 0.71 to 1 mm, the boundary saltation velocity, at which particles will travel long distances when initially suspended, was 4.28 m/s and the pickup velocity, that which moved the particles initially at rest in a layer, was 8.6 m/s.

Samples collected in the Egyptian desert by Sowelim (1983), were comprised of 88 to 90% quartz by weight with 2 to 3% each of carbonate and clay. Samples collected near Alexandria and the Matrouh region of Egypt by El-Gamal et al. (2010) show 65% by weight of sand between 62.5 μm and 125 μm and 25% by weight between 125 μm and 250 μm.

The concentration of sand particles in sandstorms depends on the local wind conditions and the relief of the land. Higher wind speeds lead to more particles being moved with a higher concentration of larger particles. There is a distribution of particle sizes with height with the larger particles staying closer to the ground. There is a vertical wind speed gradient extending from the ground due to the drag caused by interactions at the surface which follows a logarithmic model described by Bagnold (1941) such that $v(z) = 5.75\sqrt{\tau/\rho}\,\log(z/k)$, where v is the wind speed as a function of height z, τ is the drag force per unit area of surface, ρ is the density of air and k is a constant relating to the surface roughness. This shows that the actual wind speed at the mirror may vary in height from the free air wind speed. Therefore the actual damage done to the mirrors may follow a complex relationship with height due to lower wind speeds but larger particles present nearer the surface.

There are many parameters which may be used to quantify sandstorms; these are the wind speed, wind direction, particle concentration, particle size, duration

and frequency of occurrence. If these parameters were well documented then it would be possible to accurately reproduce the conditions in controlled tests. However, there is little published data on sandstorms involving particles greater than 100 μm, with the majority of measurements concerned with small dust particles of 10 μm or less particularly in China (Fu et al., 2008; Li and Zhang, 2012). The smaller dust particles have been considered particularly important as they can affect health if inhaled and may affect large areas due to the great distance they can travel (Chan, Chuang and Chen, 2008; Kuo and Shen, 2010; Thalib and Al-Taiar, 2012; Wu et al., 2013).

Some data has been collected on wind directions, speeds, duration and frequency, but little is known about the concentration levels of particles in sand storms. Concentration levels can however be estimated using the visibility, which is often measured at places such as airports. Visibility is related to the particle concentration through an inverse power law such as that found by Alhaider (1986) and Chu (1979) using microwaves, relating number of particles N to optical visibility V_0

$$N\ (particles/m^3) = \frac{0.55 \times 10^{-3}}{V_0\ a^2}, \qquad \textbf{(2.9)}$$

where a is the radius of spherical particles. This has also been seen by Hagen and Skidmore (1976) using visible light and a study in America by Chepil and Woodruff (1957) gave a result of $C_a\ (mg/ft^3) = 0.9/(0.8 \times V(miles))$. These results indicate that with the appropriate monitoring of weather conditions, the required parameters may be attainable. However, there seems to be little such data on the conditions in the Saharan regions of interest.

There are a number of military standards to assess materials which are used in the field in a variety of environments. Such standards are appropriate as a starting point for investigating the effect that sandstorms have on glass. One such standard is the US MIL-STD-810G section 510.5 dealing with sand and dust (US-DOD, 2008). This standard defines sand as particles between 150 μm and 850 μm in size. A number of parameters are also defined in the absence of

known data, for example the suggested wind speed is from 18 m/s up to 29 m/s with a concentration of up to 0.18 g/m^3.

The majority of the work on the effect that the environment has on the optical efficiency of solar collectors has focused on the short term effects of soiling of the mirrors related to on-going maintenance (Deffenbaugh, Green and Svedeman, 1986; Jorgensen et al., 2000; Tahboub, Dahleh and Goebel, 2012; Taketani, 1980). Efficiency losses due to soiling can be controlled and removed by washing, whereas the physical damage caused by particle impact has a permanent effect.

Ageing experiments have been performed on thick glass by López-Martín et al. (2011) where particle concentrations of 100, 600 and 900 mg/m^3 and wind speeds of 6, 12 and 18 m/s were used. Specular and hemispherical reflectances were measured every 4 minutes with a total exposure time of 60 minutes. The trend in measured reflectances observed was an exponential loss of reflectance with increased exposure time, with the solar weighted specular reflectance dropping from 93% to 67% for the high sand concentration, high wind speed test. Overall the wind speed was found to have a greater impact on the reflectance loss than the concentration of the particles in the air.

2.6.2 Surface damage assessment requirements

Specular reflectance is the most important measure of the effect that any surface damage has on the mirrors. The expected undamaged specular reflectance is in the region of 95% at its peak wavelength and varies according to this wavelength. A range of wavelengths should be measured to investigate whether surface damage has a varying impact with wavelength. The reflectance has been seen to reduce as low as 60% in extreme damage cases, and as such any measurements should be capable at this level.

2.6.3 Reflectance

There are two types of reflectance that must be measured, hemispherical and specular. Hemispherical reflectance is the percentage of light that is reflected

from a mirror, collected over the whole hemisphere surrounding the mirror plane. It describes the total reflected light regardless of any scattering which may be present. This is therefore a good measure of the amount of light that is being absorbed within the material itself. The reflectance spectrum measured is weighted using the 250 to 2500 nm solar spectrum specified by the ASTM G173-03 standard (ASTM, 2012), resulting in the solar weighted hemispherical reflectance. Hemispherical reflectance for solar mirrors is greater than 96% (Brogren, 2004) for silvered glass.

Specular, or direct, reflectance is a measure of the amount of light that is reflected in the plane of the incident beam normal to the surface. Using this technique it is possible to determine the amount of scattering that occurs at the mirror surface and therefore the amount of useful light which will strike the absorber. When measuring the specular reflectance, the acceptance angle of the measurement device may vary to investigate the distribution of the scattered light and the proportion which will be useful or lost (Meyen et al., 2009). The ratio of specular reflectance over hemispherical reflectance is called the gloss, and for a perfectly smooth surface would have a value of 1. That is, all the reflected light follows the ideal path and none is scattered (Meyen et al., 2009).

To measure hemispherical reflectance within a laboratory a spectrophotometer is used together with an integrating sphere (Heimsath, Kutscheidt and Nitz, 2011; Meyen et al., 2009, 2010). This is a hollow cavity, whose inside surface is coated with a diffuse reflective material. The light enters the cavity through a small hole; it reflects from the test sample and strikes the diffuse material. Any light not absorbed by the sample is reflected around the cavity by scattering from the walls, being equally distributed to the whole inner surface. This removes any directional dependence of the input light beam and the total reflection may then be measured through a second hole.

As hemispherical reflection is angle independent, it is a measure of the total amount of light that a surface will reflect. Any drop in light intensity compared to the input light beam must therefore be caused by this light being absorbed by

the sample. Measuring hemispherical reflectance therefore gives a measurement of the amount of light that is lost due to absorption.

Results of un-weathered silver-backed glass mirrors have shown solar weighted hemispherical reflectances of around 96% (Brogren, 2004; Fend et al., 2003). Fend et al. also show results of reflectance measurements following mirror exposure for 5 to 7 years. These results showed the hemispherical reflectance dropped from 95% to around 90%, indicating an increase in mirror absorption due to ageing. However, within the same investigation some samples showed negligible loss of reflectance.

Specular reflectance may also be measured using a spectrophotometer, however an integrating sphere is not used. Instead the reflected light beam must be directly captured and its intensity measured. This may be done over a range of angles and the detector aperture may be varied to give a measure of the dispersion of the reflected beam. As with the hemispherical reflectance measurements, the whole solar spectrum should be used and the results weighted accordingly.

Specular reflectance is an important measurement in regards to the soiling rate of the mirrors and is regularly used on-site at the power plants to determine cleaning routines. These measurements may need to be done on a very large number of mirrors so should be quick and easy to undertake by maintenance staff. As spectrophotometers are typically not suitable for use outside a laboratory, a hand held portable reflectometer is used. There are different commercial units available such as the D&S 15R, the Surface Optics 410-Solar and the Abengoa Solar Condor which are reviewed by Crawford et al. (2012).

The importance of measuring specular reflectance is shown in the work by Sandia Laboratories (Pettit and Freese, 1980), where samples of solar mirrors were exposed for 10 months outside. It was found that the specular reflectance was reduced five times more than the hemispherical reflectance. This indicates that the exposure directly affected the scattering of the light more than the absorption of the light. Similar experiments performed by Crawford et al. (2012)

using the reflectometers mentioned above have shown specular reflectance values decrease from 94% to 91% over 8 weeks of exposure. It is also stated that a single percentage reduction in reflectance would cost $185,000 per year on a 1,000,000 m^2 field (Pettit and Freese, 1980).

In the round robin tests performed by Meyen et al. (2010), it can be seen that the thickness of the glass has an effect on the hemispherical reflectance of the mirrors. It can be seen that the average reflectance of 4 mm, 3 mm and 0.95 mm glass mirrors are 94%, 94.5% and 96% respectively, with standard deviations of less than 0.6 to 0.7% across the measurements. The results for specular reflectance are less distinct with all results in the 95 to 96% range with lower standard deviations of around 0.4%, though the thicker glass mirrors do have a lower specular reflectance overall.

2.7 Aim and objectives

The aim of this thesis is to develop and characterise techniques to measure the form and assess the durability of mirror surfaces for concentrating solar power applications. This was done by completing the following objectives:

- Select the most suitable technique to measure the form of large mirror surfaces at CSP sites.
- Develop the capability to use the measurement technique.
- Validate the measurement technique to traceable standards.
- Assess the form of mirror surfaces of an existing CSP system.
- Gather and analyse climate data for typical CSP locations.
- Use climate data to define accelerated sand erosion testing.
- Carry out sand erosion testing using real CSP mirror samples and analyse the results.

3 METHODOLOGY

The methodology first covers the selection of photogrammetry as the measurement technique against the others discussed in the previous chapter, detailing the advantages and disadvantages of each and a decision table to determine the most appropriate. Following the selection, the development of the photogrammetry technique and its traceable validation using the CMM are presented. Details of the photogrammetry measurements performed on existing CSP systems at representative locations are then discussed. Details of the accelerated erosion testing include the collection and analysis of the climate data to inform the erosion testing, followed by details of the testing. Finally details of the surface analysis undertaken are presented, including specular and hemispherical reflectances and microscopy.

3.1 Measurement technique selection

The measurement techniques described previously were all considered for use for the characterisation of the parabolic mirror facets on-site. To aid in making the decision as to which technique should be pursued a decision table was drawn up with key factors listed and weighted according to their importance.

- **Site effects** - how the environment, e.g. heat, dust, ground stability, and also mirror sizes and positions might affect measurements.
- **Basic accuracy** - how accurate and precise the measurements are in the lab.
- **Single measurement time** - how quickly each measurement can be done once set up is complete.
- **Flexibility** - how easily the equipment can be moved or changed for different types of measurement, e.g. different orientations of mirrors.
- **Equipment size** - how portable the equipment is for taking on-site.
- **Set up time** - how long it takes from arrival to first measurement.
- **Cost**

Table 3.1 shows the decision matrix for the selected technologies, namely photogrammetry, deflectometry, VSHOT and a laser tracker. These are all methods which could be readily used on-site. Full form interferometry and the CMM were not included as these are lab based techniques which would not be suitable for transport to sites across the world.

The named methods were compared and ranked for each factor, with the best method given 4 points and the lowest given 1 point. These scores were then multiplied by the weighting of the factor, where a higher weighting is given to more important factors.

Photogrammetry suffers least from being outside the lab, as only a standard camera is needed, which is robust enough for general use. Its stated accuracy is less than the other methods at around 100 microns (Pottler et al., 2005), but this is still suitable for predicted form errors in excess of 2 to 3 mm. This accuracy can also be improved by measuring smaller areas, which can be done with minimal change to the set up. Photogrammetry is the most flexible as there are no requirements for highly calibrated or stable measurement positions. The measurements are free to be taken from any position as long as it is stable enough to prevent any blurring of the photos, typically less than 1/100s. Though the individual measurements do not take long, the targets must be attached to the mirror so this leads to an increased set up time and complexity due to the requirement to reach all parts of the mirrors.

Deflectometry would give a high resolution of the slope errors present in the mirror surface, down to 0.5 mrad (Marz et al., 2011), however this method has a complex set up requiring the measurements to be made with projectors and cameras, the calibration of which would take a long time. This set up also restricts the flexibility of the method, where moving the projector and screen would necessitate a new calibration and set up.

Another slope measurement technique is the VSHOT method, the most accurate of those considered at 0.2 mrad (Molnar et al., 2011), due to a highly calibrated laser and mountings. However, this method only provides data for a

single slice of the mirror at a time, after which the laser mounting must be moved and recalibrated, a lengthy process leading to long set up and single measurement times. The nature of the calibration and mountings mean that this is also not a flexible method and the cost would be higher due to the need for the laser and mountings.

The final method is the laser tracker method, this would be more flexible that deflectometry and VSHOT as only a line of sight is required to the retroreflective target with no requirement for reflection from the mirror itself. It is also more accurate than Photogrammetry at under 50 microns (Hexagon Metrology, 2012). The base needs to be stable and so moving the tracker would require additional time to recalibrate for the new position. This would also be the most expensive of the methods, due to the high precision tracker base and laser.

Factor	**Weight** (1 to 7)	**Photogram-metry**		**Deflecto-metry**		**VSHOT**		**Laser Tracker**	
		Point score	Factor rating	Point score	Factor rating	Point score	Factor rating	Point score	Factor rating
Site effects	7	4	**28**	3	**21**	1	**7**	2	**14**
Basic accuracy	6	1	**6**	3	**18**	4	**24**	2	**12**
Single measurement time	5	4	**20**	3	**15**	1	**5**	2	**10**
Flexibility	4	4	**16**	2	**8**	1	**4**	3	**12**
Equipment size	3	4	**12**	3	**9**	2	**6**	1	**3**
Set up time	2	4	**8**	2	**4**	1	**2**	3	**6**
Cost	1	4	**4**	3	**3**	2	**2**	1	**1**
Total			**94**		**78**		**50**		**58**

Table 3.1 - Technique decision table

For this application photogrammetry has the highest score, followed by deflectometry then laser tracker and finally VSHOT.

Photogrammetry is the method which has the best flexibility, portability and is most cost effective while still providing a good level of accuracy. The precision is usually expressed as a ratio to the image size, for example a 1:1000 precision implies 1 mm over a 1 m object or 10 mm over a 10 m object. It therefore provides good precision at both large areas and also close-up measurements. It is highly flexible and portable in that it only needs the targets to be affixed to any object at the required resolution that needs to be measured and there are no special lab conditions that need to be observed. Once the images have been captured there is also the advantage of a fully automated software stage to produce 3D points with errors and an overall RMS residual for the whole object.

Photogrammetry has the lowest accuracy of the four techniques, with the accuracy seen by Pottler et al. (2005) in measurements of large parabolic troughs in the region of 100 microns. The sizes of the errors present in parabolic trough mirrors are in the millimetre range and so 100 micron accuracy would be sufficient. However, with some optimisation it may be possible to achieve higher accuracies such as those found in similar photogrammetry applications by Burgess et al. (2009) and Pappa et al. (2002) where accuracies in the 10s of microns have been indicated for surfaces up to approximately 1 m.

3.2 Photogrammetry technique

3.2.1 Requirements

Photogrammetry must be accurate enough to measure any distortions that are present in the surface of the mirror. These distortions have typically been found to be in the low millimetre region. To reliably measure to such a level, the accuracy of photogrammetry must therefore be much smaller than the millimetre level. A maximum of 100 µm accuracy should be allowed, which has been indicated from the results of preliminary tests without optimization.

Photogrammetry was initially validated and its uncertainty found by comparing the results of measurements done using both the CMM and photogrammetry on

the same mirror surfaces. Once the uncertainty was known photogrammetry was then used away from the CMM for measuring the mirror facets using external influences to simulate distortions such as gravity, temperature, wind loading. It is therefore important that the photogrammetry technique established is suitable for use away from the CMM area.

The photogrammetry must provide a relatively simple and swift measurement per mirror facet, as the troughs are made of many hundreds of facets. Reducing the measurement time also enables a larger number of repeat measurements under different conditions including different orientations and with different applied forces. The simpler the set up and method, the greater the ability of the technique to be adapted for different situations outside the laboratory.

3.2.2 Equipment

There are three main pieces of equipment needed for photogrammetry measurements: the camera, the software and the targets.

The camera must have a stable optical configuration, with all settings able to be manually controlled. Resolution and sensor size are important, making a digital SLR camera the most suitable. These have interchangeable lenses, can be fully manual and are high resolution. Following these guidelines a Canon EOS 600D was purchased, which has an 18.0 MPixel CMOS APS-C sensor measuring 22.3 x 14.9 mm. The photographs taken are stored on an SD card and are then transferred to a PC for loading into the photogrammetry software.

There are a number of photogrammetry software packages available, which specialise in a range of photogrammetry applications such as aerial, industrial and crime scene. In choosing a software package it was important to consider the ease of use, availability of technical support and documentation, and the accuracy achievable. The photogrammetry software chosen was PhotoModeler from EOS Systems Inc. This software allows an automatic project to be set up where the photographs are loaded and the points are automatically marked, referenced and the solution found with minimal user input. This is an important

feature in speeding up the photogrammetry technique as a whole. Coded targets are included in this automatic process, as they may be uniquely identified by rings surrounding the central point.

The target points are located by the software and a least squares fit is performed to find the centre of the shape, usually a circle. To allow the fitting algorithm to find the centre effectively there is a requirement that the target circle has a high contrast difference against its background. The use of black and white targets is common and these may be printed out onto paper or other materials. These printed high contrast targets therefore have the flexibility to be varied in size and configuration to determine the optimal parameters for high accuracy. The coded rings can also easily be printed at no extra cost. In addition to printed targets, retroreflective targets may be used. These reflect the flash from the camera giving a very high contrast against their background providing possibly the highest accuracy possible for photogrammetry targets. However these are not as customisable as the printed targets, and are much more expensive to manufacture in large numbers.

3.2.3 Camera settings

There are a number of different camera settings that affect the quality of the images taken for photogrammetry. It is important to optimise such settings to provide the best images possible for input into the photogrammetry software. The relevant camera settings are the aperture size, the shutter speed and the use of the flash.

The aperture size controls the depth of focus of the image, which is a measure of the closest and furthest distances that the image will have an acceptable level of focus. This is important as all targets on the mirror, which is 2 m along its diagonal, should be within this depth of focus so as to have their maximum sharpness and so their optimal identification and centring. If the depth of focus is too small then the furthest and nearest points will be blurry, however if the depth of focus is too large all the points as a whole will gain an amount of blur affecting the accuracy.

The shutter speed affects the amount of light that the camera sensor receives from the object, and also affects the amount of motion blur which may result from the camera being hand-held. A faster shutter, with less time open, will result in less light striking the sensor and also a reduction in the movement that occurs while the shutter is open. This acts to both increase the contrast of the targets and also reduce the blurring due to motion. However if the shutter is too fast, the white parts of the targets will also start to reduce, diminishing the contrast again. The flash is important to increase the amount of light received from the target and so the contrast of the target.

The photogrammetry software obtains the point positions by calculating the focal length of the camera, so it is crucial that is remains fixed during each set of measurement photographs. It is therefore important to turn off any automatic focussing for the duration of the measurement. It can however be used to find the initial focus position for the first photograph.

The software also uses the position of the pixels on the camera sensor itself in calculating the point positions. Image stabilisation is done by moving this sensor to match any camera shake, thus reducing the apparent movement in the photograph. However this sensor movement is undesirable for photogrammetry, so this setting should also be turned off.

3.2.4 Procedure

The method of photogrammetry measurements is not universally well defined and depends upon the particular object and environment under test. Key elements of the method are the number of photographs, the number and size of targets, the distance to the targets and positions that the photographs are taken from.

These elements should all be tested to optimise the photogrammetry procedure, however some can be approximately calculated prior to testing.

The mirror facets being measured are positioned using their support points in the position suitable for the measurement conditions. For example, the resting

shape test may be done on the CMM bed, whereas orientation dependent gravity tests are done with the mirror tilted. In all cases the mirror is allowed to rest and achieve a stable position so that it does not move over the time it takes to take the set of photographs for the measurement, typically only a few minutes.

In analysing the photographs the coordinate system and scale of the object must be found. This is due to the inability to distinguish the real life size of an object from a photograph, without a length of known size also present in the photograph. This may consist of a number of targets pre-placed at known distances from each other or known features of the mirrors or structure itself such as the corners. The use of already present features is dependent on the stability of such structures and the ease of including a scale artefact. In some cases it may not be possible to include such an artefact in the images without artificially disturbing the positions of the mirrors, in which case it is preferable to use features of the mirror itself.

To establish the accuracy of photogrammetry and to optimise the camera settings, with minimal manipulation by software and surface mapping algorithms, it is necessary to perform sets of measurements to find identical points with both photogrammetry and the CMM. The point positions may then be compared, with the photogrammetry uncertainty resulting from the difference between the sets of data, within the error of the CMM. To measure identical points using both techniques requires the use of sphere targets. Photogrammetry identifies the spheres as circular targets and so the centre of these will be found. Taking the centres for the same target from many angles will result in the centre of the sphere, which is the point measured using the CMM. The targets used are 10 mm white ceramic spheres, so as to be reflective and so have a high contrast against the background which is blackened. 25 spheres are fixed in a grid on the CMM bed where both techniques may be used. Various camera settings and procedural parameters are varied individually and the resulting accuracy changes are recorded. From

these results an optimal camera set up is determined and the accuracy of this is verified by repeat measurements.

Once the accuracy and camera settings have been established, the same camera settings are then used in measuring the mirror facet, due to its similar size to the sphere grid. In this case flat circular targets are fixed to the mirror facet rather than using ceramic spheres. The resulting point cloud is then exported for use in generating surface maps.

3.3 CMM methods

3.3.1 Requirements

To ensure that the CMM result may be used as a reliable 'true' surface for comparison the accuracy and precision of the CMM results should be much better than those obtained through photogrammetry.

When comparing the two sets of data it is important that the measurement surfaces are identical to remove errors resulting from location, the coordinate systems should therefore be the same. There is a need for many repeat measurements of the mirror facets with different numbers and densities of points and also the ability to focus on single areas only. This makes it important to create a method by which the programming for the CMM may be easily modified dependent on such parameters.

3.3.2 Equipment

The CMM (Figure 3.1) is a Leitz PMM-F moving bridge configuration designed with a minimized moving mass comprising the Z-ram and upper bridge section. The main body of the CMM is constructed from granite, which has high stiffness, high thermal mass and low thermal expansion. The moving bridge x-axis is controlled by dual ball spindle drives with two measurement scales to increase the precision of the system. The Z-ram itself is ceramic with a Leitz LSP-S2 probe system which may accommodate stylus extensions up to 800 mm in length (Leitz, 2012). It has a measurement volume of 3 x 2 x 1 m and is

located in a temperature and humidity controlled laboratory in the Cranfield University Precision Engineering Institute where it is primarily used for measurements of large optical components.

The CMM has a traceable accuracy, defined by the equation:

$$Accuracy = 1.9\mu m + L/400\,, \tag{3.1}$$

where L, the longest length measured, is in millimetres. Over the mirror facet's diagonal of L = 2000 mm this equals 6.9 µm calibrated accuracy error.

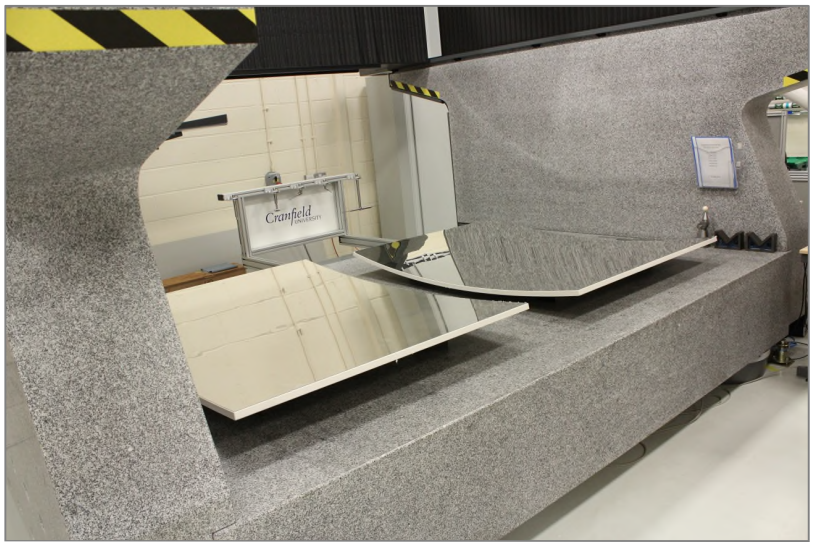

Figure 3.1 - CMM with mirror facets

The large measurement volume capability makes it ideal for measuring the 1.6 x 1.2 x 0.3 m mirror facets. It is fully programmable and can measure points automatically enabling high numbers and densities of points on complex free form surfaces whilst maintaining speed and accuracy.

3.3.3 Procedure

It is important that the mirror is being supported in a stable way and one that does not produce unnatural stress and distortion into the facet. Typically surfaces are kinematically supported to minimise distortions, however to ensure that the CMM results correspond to on-site measurements of the mirrors they were supported at points that are representative of its trough support structure.

The six fixing points on its back structure were used as the support points to be placed on the granite CMM bed. These points were supported by vertically adjustable feet which are set to the correct heights according to the design data provided with the mirror facets. These may also be adjusted to remove or alternatively place stress into the mirror to investigate misalignment of the supports.

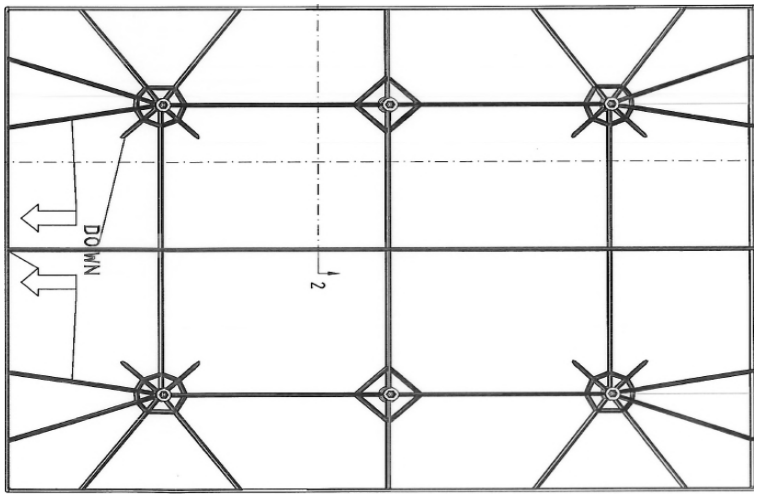

Figure 3.2 - Mirror support structure

As the CMM is being used to validate the photogrammetry it is important that the accuracy of the measurements made is much higher than that of photogrammetry. The time allowed for laboratory measurements is greater than available when visiting CSP sites. The CMM has the ability to make high density point clouds of the surface enabling full analysis of the novel structure to be investigated, for example any influence of the ribbed structure. A point spacing of 20 mm was selected from studying the supporting structure and minimum feature sizes on the mirror backing in Figure 3.2 (Ronda High Tech, 2012). This spacing produces around 5,000 points per facet, which measured at 5 seconds per point results in a measurement time of 6 to 7 hours including the coordinate system definition. This was deemed acceptable for a research tool and validation technique. Once the high density measurement has been completed and distortions assessed the point spacing may be adjusted to reflect the actual size of error seen. Reducing the number of points would then significantly

decrease the measurement time, allowing higher numbers of repeat measurements to be made.

There are a number of considerations when using the CMM, including establishing a reliable coordinate system under which the measurements are made. This coordinate system should be defined using the mirror itself so as to simplify the analysis of the points that follows. Other considerations are the number and density of points that are taken on the mirror surface, where a higher density of points potentially enables a more accurate surface profile to be measured, but the measurement takes longer to run.

The coordinate system should be defined using a plane, an axis and a point; or three planes (Hexagon Metrology, 2012b). The mirror has six support points built into its back surface mounting, which all provide surfaces onto which the mirror can sit. The CMM granite bed is used as the plane for the mirror coordinate system, the axis is defined as the long edge of the mirror and the point defined at one of the mirror corners.

The CMM measurement subroutines do not have a built-in parabolic trough procedure, therefore it is necessary to define a measurement procedure. As the parabolic trough is close to a cylinder, deviating by a maximum of 2 mm for the Ronda mirror, it is possible to measure the trough as an approximate cylinder using a search distance of 4 mm from the cylinder shape. The CMM will move to a position 4 mm from the surface of the virtual cylinder and begin slowly probing until it touches the real surface. This ensures that the probe head does not impact the mirror. However, as this increased search distance slows the measurement down; on subsequent measurements the actual points measured are used as nominal probing points thus reducing the time.

A second method is to measure an approximate circle along the curved direction of the trough, again with the increased search distance. The actual arc measured is a parabola, which is then translated along the length of the mirror in steps to produce the parabolic trough shape. This method reduces the time taken compared to the cylinder method, especially when changing the point

spacing, which may be done by the first circle points and then the translation step size.

Once the measurements have been completed the resultant coordinates of the measured points are extracted from the CMM and output as a point cloud in a text format. This data is analysed using bespoke MATLAB algorithms in order to assess CMM and photogrammetry data directly.

3.4 Surface mapping and evaluating performance

The point clouds generated using photogrammetry and the CMM are imported into MATLAB and analysed using custom algorithms (see Appendix). As both measurements were done using identical coordinate systems the point clouds need no further adjustment in orientation against one another. For photogrammetry, the points recorded are those on the surface of the targets, which are the thickness of the target away from the mirror surface. This distance is seen as a systematic error between the two data sets and is removed in the fitting and comparison of the data.

The equation of the mirror facet is known and is fit against each point cloud showing the residual error maps in the mirror surfaces for each technique. By subtracting these maps from one another, the measurement differences between the CMM and photogrammetry are seen. As the CMM has a much higher accuracy than photogrammetry, this map is taken as the actual surface. Any departure from this shown in the photogrammetry maps is therefore due to errors in photogrammetry, down to the level of accuracy of the CMM at approximately 6 µm.

The uncertainty map is investigated and attempts are made to determine the likely causes for the errors. For example, it is likely that the points towards the edge of the mirror facet have a higher uncertainty than those towards the centre. This is due to the focal point of the camera being at the centre, and the edges being toward to outer edge of the lens, where distortion is highest. While this distortion should be removed by calibration, any remaining distortion is

seen on the surface maps as a radial error coming away from the centre of focus.

The slope in the curved direction is most important in determining the optical efficiency of the mirror as this determines the distance from the focal point at which the reflected light strikes. This slope is calculated from the positions of adjacent points in the surface map. To eliminate the effects of target misalignment the surface map is interpolated to a regular grid aligned to the mirror edges. This ensures that the calculated slope is precisely along the curved direction. This slope is assigned to the point midway between the two adjacent points used in the calculation.

Once these slopes are known it is then possible to construct a ray trace by projecting incoming vertical light rays onto each point and following its reflection towards the focal point. The actual position that the light ray strikes the absorber tube can then be seen, along with any missing rays.

Performance of parabolic trough collectors can be measured by the intercept factor. This is a measure of the percentage of the light incident on the mirror that strikes the absorber tube. An ideal collector would have an intercept factor of 100%, where distortions causing light to be lost reduce this down to typical values of 96 to 97% (Ulmer et al., 2007).

3.5 Photogrammetry measurements

3.5.1 Photogrammetry validation against CMM

The mirror is placed onto the CMM bed on its 6 support feet at its designed state. Three spheres are fixed on the edge of the mirror at three corners to provide direct point to point alignment between CMM measurements and photogrammetry. The CMM is then used to measure with a point spacing of approximately 50 mm in both directions. Recorded is each individual points in x, y and z and also the direction of the normal to the contact point. As the point recorded is the centre of the probe, the probe radius must then be used with the normal direction to offset each point towards the mirror. Each measurement

cycle is repeated 10 times to give an average value for each point, along with the CMM repeatability, which is at the sub-micron level. Each of the sphere positions is also recorded. Without moving the mirror, sets of photogrammetry photographs are taken using the procedure previously defined with the inclusion of the three sphere points. Both data sets are then loaded into MATLAB for analysis.

There are two methods for aligning the point clouds. The first is by using the three sphere points which are common between the measurement techniques. The second is by using a photogrammetry scale only, and then automatically rotating the point clouds to align them.

Using the sphere targets gives a true alignment procedure, but the result depends heavily on the accuracy of these three points only. The points are difficult to distinguish from the background due to the lack of dark background, as was used for the sphere grid. This is due to the presence of the mirror preventing insertion of the background material. Any departures from the CMM measurements seen are caused by both photogrammetry errors and also the coordinate system alignment errors; this will therefore not give a true photogrammetry error map. To avoid the errors caused by the coordinate system alignment, the automatic rotation alignment should be used. This will only show the departures inherent in the photogrammetry itself, rather than including errors in measuring the three spheres.

In order to define the scale of the mirror within the PhotoModeler software it is necessary to know the distance between adjacent points. This can be done by either using the sphere targets, the distance between which can be calculated from the CMM measurements, or by using the distance between the printed disc targets. Due to the difficulty in accurately measuring the sphere targets discussed before, it is necessary to measure the distance between the printed disc targets. A sample of target sheet is taken and the distance between adjacent points measured using the vision system on a TESA CMM. The target sheets are in a grid of 4 by 3 so for increased accuracy the longest distance along a strip is measured and used to set the scale. It was shown previously

with the sphere targets that the length of the scale used can have an impact on the accuracy of the photogrammetry.

If the scale points are placed along the curved direction of the mirror then measuring the targets off mirror will provide a measurement with a small difference from that when the targets are placed on the mirror due to the curve. The curve will bring the two target points closer together on the mirror than when measured flat on the TESA. This difference will be a maximum at the base of the parabola where the curve is greatest as seen in Figure 3.3.

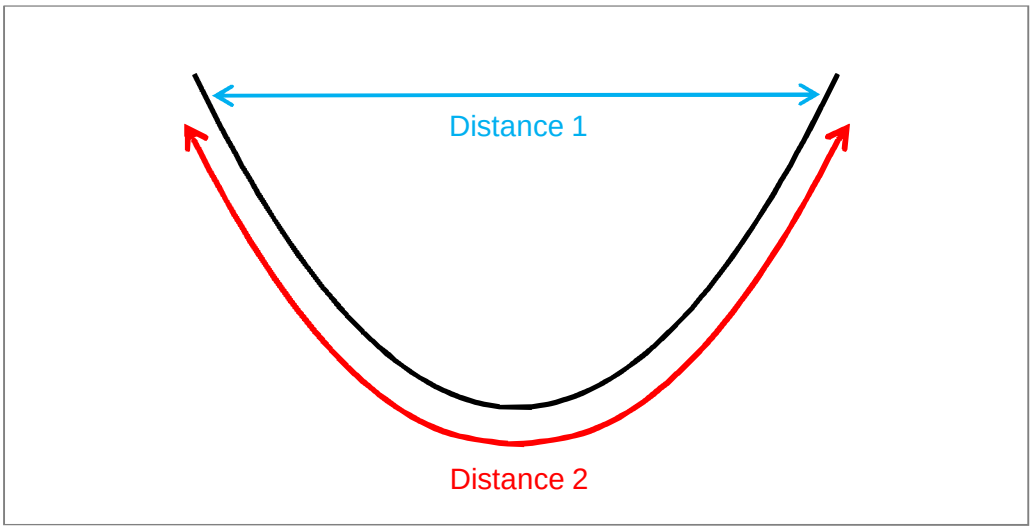

Figure 3.3 - Effect of parabola on scale measurement

The arc length (distance 2) of a parabolic segment is (Wolfram MathWorld, 2013):

$$s = \int_{-a}^{a} \sqrt{1 + y'^2}\, dx \tag{3.2}$$

$$= 2 \int_{0}^{a} \sqrt{1 + y'^2}\, dx \tag{3.3}$$

$$= \sqrt{a^2 + 4h^2} + \frac{a^2}{2h} \sinh^{-1}\left(\frac{2h}{a}\right) \tag{3.4}$$

where a and h are defined in Figure 3.4 and $y = h\left(1 - \frac{x^2}{a^2}\right)$ for $-a \leq x \leq a$.

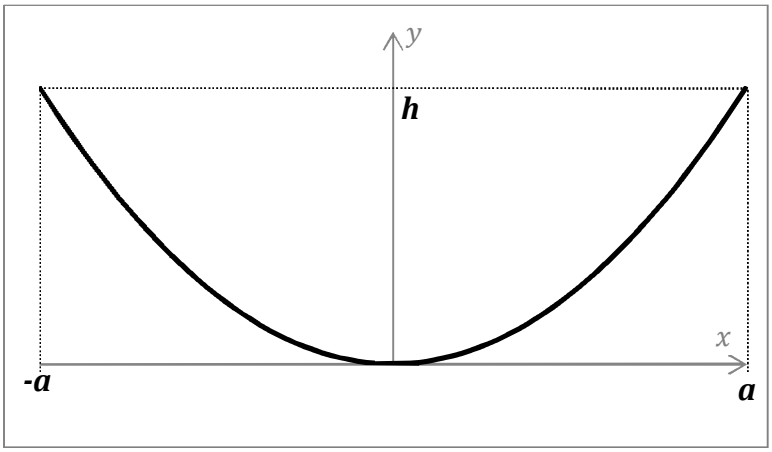

Figure 3.4 - Length of a parabolic segment

The equation of a parabola is $y = \frac{x^2}{4F}$, where F is the focal length. For the Ronda mirror under investigation F = 1810 mm, therefore $y = \frac{x^2}{4\times1810}$. It follows from Figure 3.4 that $h = \frac{a^2}{7240}$ and thus (3.4) becomes

$$s = \sqrt{a^2 + 4\left(\frac{a^4}{7240^2}\right)} + 3620\sinh^{-1}\left(\frac{a}{3620}\right). \quad \textbf{(3.5)}$$

If $2a = 100\,mm,$ then $s = 100.00318\,mm$ making a difference of 3.18 μm per 100 mm scale bar size. Over the 1600 mm mirror length, this becomes an error of 50.9 μm, which is at the approximate expected accuracy level of the photogrammetry. This is calculated at the extreme curve, so that any actual error is less than this value. To minimise this error, the scale length is taken along the axis of the trough, with any curve only due to target misalignment, which is minimal.

Once the two sets of point clouds are obtained they are compared against one another for the level of correlation. The surface maps have their coordinate systems aligned and then a regular grid of points is applied to both maps. This creates new interpolated points with common x and y values allowing their direct subtraction in the z direction. This shows any vertical variations between the methods, which are caused by errors in the photogrammetry due to the high accuracy of the CMM providing the ‘actual’ surface.

3.5.2 Effect of external factors

To test the effect of installation errors, the supports are distorted by different amounts and the shape of the mirror measured in comparison with the undistorted shape. In this way, a series of surface maps are created along with their causes to build up a picture of how the shape of the mirror reacts to incorrect installation. The surface maps created by on-site measurements may then be analysed and compared to these to show which supports may be misaligned. To create these distortions, thin plastic sheets of known thickness are placed under the supports. The configuration and thickness of the sheets is varied to provide the different distortions. The undistorted supports are clamped down to avoid unwanted movement, adjacent supports lifting from the table for example, which would not be possible when clamped to the support structure.

To determine the effect from gravitational sag, it is necessary to place the mirror on its support structure at varying positions. This is only possible on site, where the trough may be moved as a whole, thus distorting the mirrors. At each position the facet is measured with photogrammetry to see how the shape changes with its orientation. By measuring the trough as a whole, as the mirror is moved it is also possible to measure whether there is any significant error in tracking due to non-rigid structure causing one end of the trough to lag behind the driven end.

3.5.3 On-site considerations

There are many considerations which must be made when moving from the laboratory to an on-site environment. These include changes to the targets, camera settings and procedure.

The target sheets used in the lab are created on a standard printer and cover a single mirror at any time. These targets are time consuming both to apply and remove as they are in small sheets and are slightly adhesive. When measuring multiple facets, or an entire trough these targets would not be suitable due to the length of time and subsequent mirror cleaning required. An additional factor

is the number of coded targets required for multiple facets exceeds the number available from the PhotoModeler software. This requires a change of the target sheets both in material and design. A more appropriate material is a static cling vinyl sheet, which can be made to fit a whole mirror facet without any adhesive residue. Fewer sheets to apply also decreases the time taken to apply and remove the targets significantly. The design printed onto these sheets is adapted to include a mixture of coded and non-coded dot targets of identical diameters.

To measure the whole trough for large scale distortions, separate larger diameter coded targets are used. When taking photographs of large areas of the trough, rather than individual facets, the larger diameter ensures that the pixel sizes of the targets in the photographs remain above the 10 pixel minimum previously defined.

In the laboratory the lighting conditions are constant throughout the experiments and also between experiments. On-site the light level can vary both during the photograph capture stage, perhaps due to clouds or camera shading, and also between successive experiments. Overall the light levels are expected to be much brighter than those in the laboratory and as this affects the contrast across the images, adjustments to the shutter speed are required. It is also unlikely that the flash will be as effective in enhancing the contrast on-site as it is in the laboratory.

It is important to be able to maintain a good level of contrast within the photographs independent of the lighting conditions. As the shutter speed does not change the configuration of the optics within the camera, it will not have a negative effect on the accuracy of the photogrammetry. Changing the shutter speed to retain the contrast is therefore possible by gauging the contrast both by studying the photographs and also examining the histogram data available on the camera itself. This histogram data shows the amount of pixels of any particular light level from black to white. By adjusting the shutter speed such that the whole range of levels are covered it is possible to control and optimise the contrast.

There are two significant issues which arise in moving from measuring a single facet located on a laboratory table to facets suspended vertically up to a height of 7 to 8 m. These are obtaining the required camera positions for optimal photogrammetry and reaching all parts of the mirror surface to apply the target sheets. There is therefore a requirement for the use of an elevated platform system capable of reaching up to 10 m and with enough control and range of movement to reach all parts of the trough. Such systems are usually available at parabolic trough plants and are regularly used for operations and maintenance tasks. It is also possible that some camera positions may not be achievable due to limitations of such systems and any obstructions which may be present on-site. Some camera positions may not be possible if they are close to the focus of the trough making it unsafe or there are strong solar reflections towards the camera, unsuitable for the photographs. To compensate for the loss of camera positions additional photographs can be taken from adjacent or previously unused locations.

Weather conditions can impact photogrammetry, for example due to rain, which may cause the targets to detach or the camera to get wet, or high temperatures may reduce the time that an operator is able to stay out of the shade. Such factors are unavoidable; however weather such as rain is not as common in locations where CSP systems are used.

3.5.4 Outdoor preliminary tests

Experiments were done on a linear Fresnel collector in Islamabad, Pakistan during February 2013 (Figure 3.5). The linear Fresnel has 1 inch width mirror strips which require special targets to be printed, possible within the flexibility of photogrammetry. There is insufficient space on the thin mirror strips to place both the central disc and the coded ring for all targets; therefore thin strips of targets were printed with two rows of dots on each so as to enable measurement of the tilt of the mirrors. Single coded targets were distributed between strips and around the measurement area to provide initial orientation of the photographs. The photographs were taken in sets of 16 as before with two

rotation angles, the aim of these experiments was to test the photogrammetry technique to find the tilt angles of each strip and its sag.

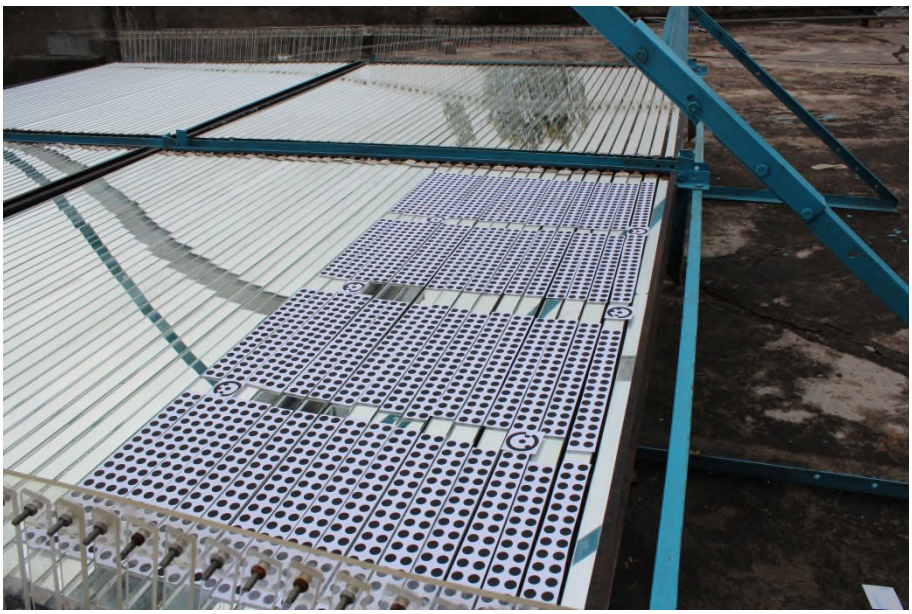

Figure 3.5 - Pakistan Linear Fresnel with targets

During these tests it was noted that the laboratory settings of flash on and shutter speed 1/125s produced low contrast 'grey' images as seen in Figure 3.6c. By varying the shutter from 1/4000 (Figure 3.6a) to 1/125 and running the PhotoModeler point marking procedure on each photograph it was seen that the most points were identified in the highest contrast photograph with the expected histogram. This shutter speed was 1/1000s with no flash (Figure 3.6b), compared to 1/125s with flash in the laboratory.

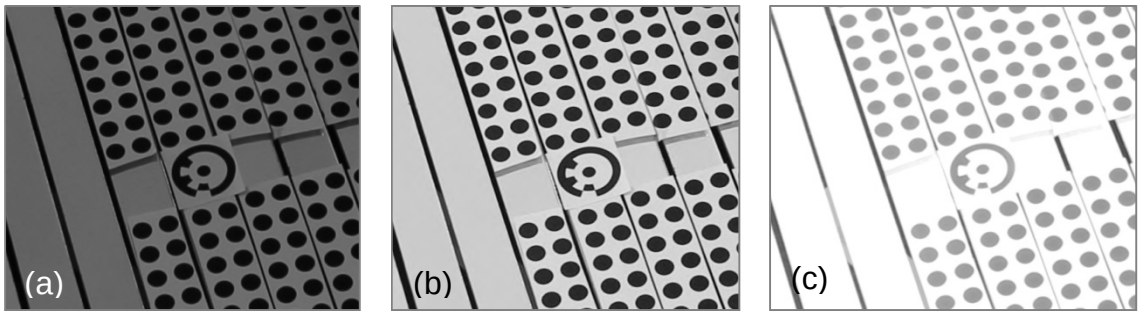

Figure 3.6 - Shutter variation vs. contrast

Measurements were made of a small parabolic trough installed in Saudi Arabia (Figure 3.7), showing again that a much higher shutter speed is required on-site, in this case up to 1/1250s. An additional issue encountered was the susceptibility of the ink of the printed targets to smudge due to the heat. This occurred when the targets were applied indicating that care should be taken not to directly contact the ink of the targets where possible and to record any targets which have been smudged so as to remove them from the final results.

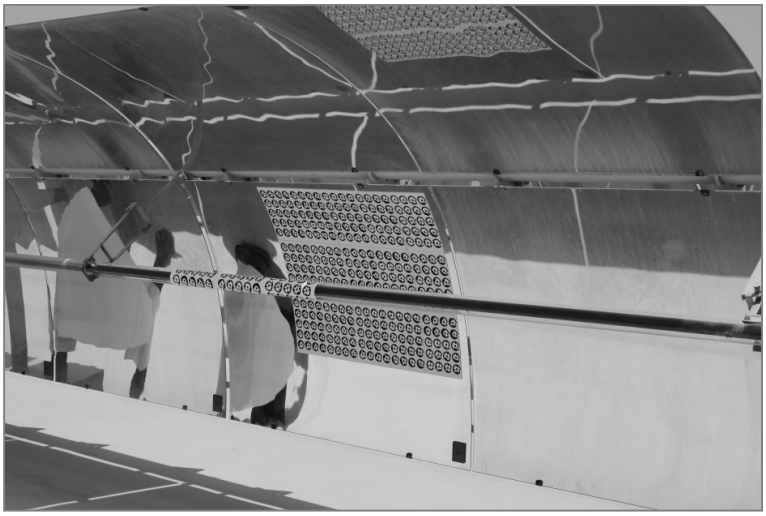

Figure 3.7 - Saudi Arabia parabolic trough

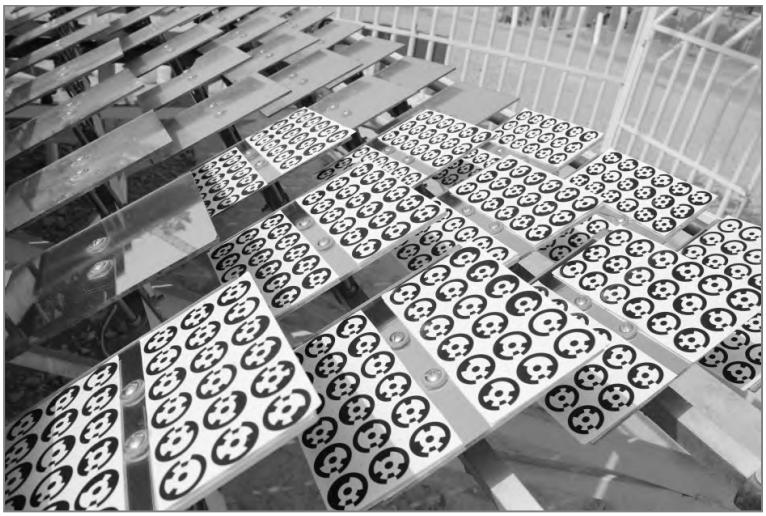

Figure 3.8 - Saudi Arabia point focus linear Fresnel

A set of 200 mm square mirrors for a point focus linear Fresnel collector was also measured in Saudi Arabia (Figure 3.8). The mirrors were measured as a single object of interest making up approximately 1 square meter, the appropriate size for the previously established parameters. Each mirror had a grid of targets applied allowing both the form and orientation of each mirror to be measured.

3.5.5 On-site parabolic trough measurements

Measurements were done at the *Italian National agency for new technologies, Energy and sustainable economic development* (ENEA) near Rome, where a parabolic trough test line is under construction with Ronda thin glass mirror collectors installed. These mirrors are the same construction as those measured in the laboratory and serve as a direct comparison. Construction of the trough had not been fully completed and as such the mirrors had not been adjusted to their final positions, thus any errors are expected to be significant and measurable.

Three ground level mirrors were covered in target sheets for measurement and comparison as shown in Figure 3.9, with targets placed at the corners of the mirrors to define the coordinate system. These mirrors were chosen as they were easily accessible without the requirement for a movable platform.

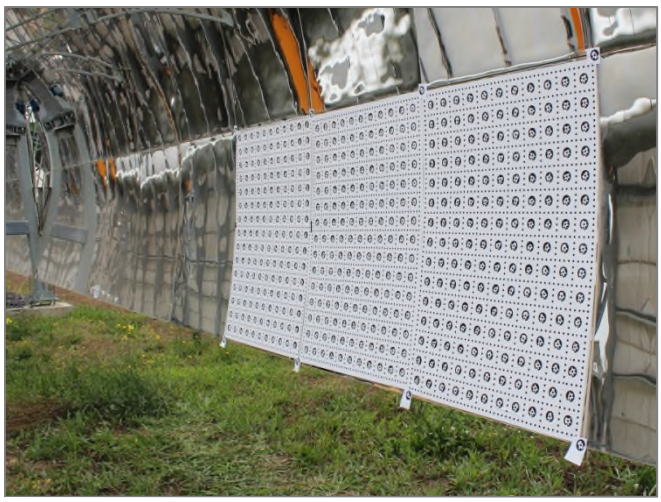

Figure 3.9 - ENEA photogrammetry set up

Targets were placed at the corners of the mirrors to define the coordinate system to be aligned with the facets and to provide known scale lengths along the straight edges. The first target sheet to be applied was on a mirror that was still damp from cleaning beforehand. This moisture caused the edges of the target sheet to detach from the mirror and some bubbles to form under the sheet. The individual target dots not fully attached to the mirror were noted for removal in the analysis stage. Subsequent mirrors were thoroughly dried and the sheets were cut into sections to aid attachment and bubble removal. These target sheets attached more readily with little detachment, with any detached edge dots noted.

As the mirrors are identical to those measured in the lab and the camera positions are therefore the same, the aperture value of f/7.1 found in the lab was optimal for the photographs. To determine the shutter speed appropriate for the lighting conditions the target sheets were captured using a range of shutter speeds. Each photograph was studied for best contrast and the histogram was considered. This set the shutter speed at 1/125s, in cloudy conditions.

Figure 3.10 - ENEA photograph capture

Each mirror was photographed separately with additional overlapping sections photographed to enable the facets to be compared to one another directly. As

the mirrors are close to the ground, the lowest ideal camera positions were not attainable so additional photographs were taken to compensate for these. To reach the upper camera positions the camera was placed onto a monopod and positioning and capture were controlled via a remote display as shown in Figure 3.10.

Measurements were done at Plataforma Solar de Almería (PSA) Spain, on EuroTrough collectors which are conventional 4 mm thick glass mirrors currently used at CSP plants. These troughs are formed in 12 m assemblies with an aperture of 5.76 m and a focal length of 1.71 m. Each assembly is formed from four horizontal rows of mirrors with the outermost mirror dimensions of 1.5 x 1.7 m and the innermost mirror dimensions of 1.64 x 1.7 m. These troughs have similar overall size to the Ronda troughs, but the individual facets are larger giving a grid of 7 x 4 mirrors compared to the Ronda 10 x 4 grid. The EuroTrough facets are held by four support points compared to the 6 of the Ronda mirror.

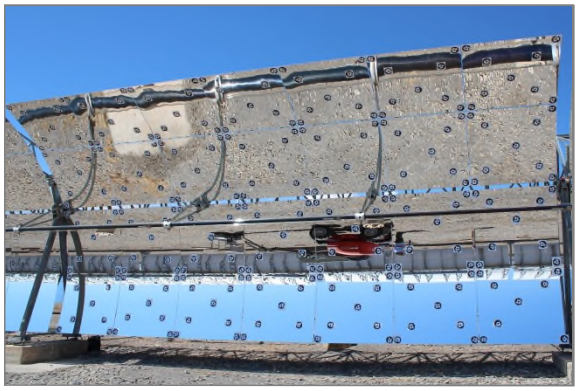

Figure 3.11 - Whole trough PSA set up

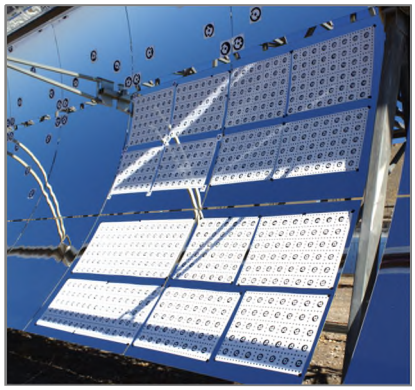

Figure 3.12 - Four facet PSA set up

Two set ups were used at PSA, the first was a whole trough measurement where large diameter individual targets were placed over the whole trough to measure the total shape and large errors, Figure 3.11. These targets were placed with one in each corner, one over each support point and one in the centre of the mirror totalling 9 per facet and 252 over the whole trough. The second set up placed target sheets over four mirrors only, to measure the lower

magnitude facet distortions. For these measurements, due to the larger facet size the target sheets were placed in sections covering the support positions, Figure 3.12.

The mirrors had been previously cleaned thoroughly so only a dry wipe was required to remove any dust. This ensured good contact and adhesion of the targets such that no sheets lifted at the edges and there were few bubbles.

Two separate sets of camera settings were used for the whole trough and the 4 facet measurements. For the whole trough, the aperture value was increased to f/16 to increase the depth of focus to ensure the whole trough was in focus. The shutter speed was set at 1/100s by studying a number of photographs with varying shutter speeds. This shutter speed is lower than the laboratory and ENEA tests despite the increased light due to the smaller aperture used, which significantly reduces the light entering the camera. For the whole trough the photographs taken capture the majority of the trough in each image from a number of positions surrounding the trough obtained using the platform lift available, Figure 3.13. The range of positions was limited by the ground and there were some reflections from the sun, causing additional positions to be required to compensate for the lost ideal ones.

Figure 3.13 - Whole trough photogrammetry at PSA

For the four facet measurement the aperture was returned to f/7.1, at which point the shutter speed was increased to 1/1000s by studying the contrasts as before. This shutter speed matches that used in Pakistan and is closer to that used in Saudi Arabia, which had similar lighting conditions. The photographs were taken in such a manner as to consider each facet as a separate object, with additional overlapping photographs taken as at ENEA. Some of the ideal positions were unobtainable due to the position of the absorber tube and structural elements blocking some images. Additional photographs were taken from nearby positions, Figure 3.14. Additionally due to the high direct sunlight there were positions where solar reflections were an issue as well as some positions close to the focal line of the trough being unsafe due to the intense concentrated sunlight.

Figure 3.14 - Four facet photogrammetry at PSA

3.6 Accelerated erosion testing

Environmental considerations and material testing for service life is described in the US Department of Defence standard MIL-STD-810G (US-DOD, 2008). Specifically, method 510.5 discusses tests for simulating blowing sand and dust exposure. This is not a generally used method for CSP, however it has been applied in the absence of any established standard. This provides a valuable starting point for assessment of surfaces for CSP. Within the section titled

"Procedure 2 - blowing sand", the temperature, wind speed, equipment configuration, sand composition, sand concentration and test duration are discussed.

The temperature should be set to the highest operating temperature that the material will be subject to during its lifetime, which for solar mirrors will be at 50°C. The wind speeds are typically 18 m/s with gusts up to 29 m/s so testing should occur in this range. There should also be a distance of 3 m between the sand injection point and the sample to ensure that the sand has been accelerated to the required velocity, unless it can otherwise be shown that this is achieved with a shorter distance using the equipment available.

The sand should be silica sand, 95% SiO_2 by weight, with a recommended size range of 150 to 850 µm, and fresh sand should be used for each test to avoid contamination by any sample material removed during abrasion. Unless the concentration at site is known, 0.18 g/m^3, -0.0/+0.2 g/m^3 should be used. This should be for a duration of at least 90 minutes for each test. The sand used for the erosion testing in this thesis is MIL-E-5007C (referred to as MIL sand), which is a synthetic silica sand conforming to the specification above.

3.6.1 Equipment and safety

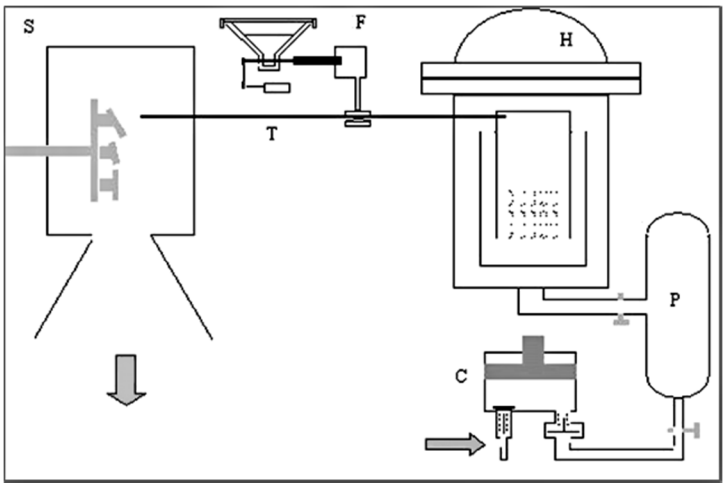

Figure 3.15 - Cranfield University erosion rig

The ageing is done using an erosion rig as shown in Figure 3.15 (Jaslier, 1995). A compressor (C) supplies air to the pressure vessel (P) where the required pressure is maintained. This air is then fed through a heating system (H) and flows through the acceleration tube (T) into which the sand is fed (F). The air then accelerates the sand which continues and strikes the mirror held in the sample holder (S).

The sample holder allows variable impact angles of 30°, 45°, 60°, 75° and 90° and is located 20 mm from the acceleration tube nozzle, exit diameter 13 mm. The sand is injected at a distance of 1.2 m from the nozzle and is fed through a Venturi nozzle, which causes the sand to be sucked into the air stream by the pressure reduction caused by the Venturi effect. A controlled mass of sand is injected over a 10 second time period. It impacts the sample over a circular area of 20 mm diameter and is extracted by a ventilation system.

Safety concerns when using the erosion rig are due to small silica particles, which may cause silicosis following long exposure times. While the silica sand is low risk when stationary, when accelerated to high velocities smaller dust particles can be created during impact, which may enter the lungs. Although the velocities used for these ageing tests are relatively low, there is a requirement for proper ventilation and air filtration, breathing masks and restrictions on usage time to lower the risk of exposure.

3.6.2 Air velocity vs. pressure calibration

The air velocity is set using the pressure at the pressure vessel and therefore the required velocities should be measured and calibrated against the pressures used. For this a small 20 mm diameter anemometer is used, placed at the sample site in place of the sample holder. The pressure is then varied, with no sand injection, to find the pressure values giving a velocity range from 0 to 29 m/s as stated in the MIL-STD-810G standard.

The pressure was set in 0.2 bar intervals, where initial tests have shown that 0.4 bar gives an air velocity of 25 m/s. It was noted that the required pressure is

extremely low compared to the usual operating range of the equipment. This complicates the calibration as there is no pressure reading under 0.1 bar which corresponds to the lowest air velocities. While the calibration curve may be used for higher velocities it is therefore necessary to set the air speed using the anemometer each time the equipment is used to ensure the correct speeds are used.

3.6.3 Climate data and flux calculations

To determine the air velocity to use in the erosion experiments it is necessary to consider the climate data for the target site. In this case the site is in Alexandria, Egypt and climate data was obtained from the Wunderground.com website which records data measured at weather stations located across the world. The specific weather station used is the Borg El-Arab airport weather station. Hourly observations were obtained for a two year period from 2012 to 2013 containing temperature, humidity, pressure, visibility, wind speed, gust speed and wind direction (Figure A.5). Additionally a note is made of the current conditions, for example clear, rain, fog, sandstorm etc. The data can be separated into those periods during which sandstorms were observed and those periods where no sandstorms are observed. The average conditions with sandstorms, without sandstorms and overall yearly averages can be seen in Table 3.2.

	Temperature (°C)	Humidity (%)	Sea Level Pressure (hPa)	Visibility (km)	Wind Speed (m/s)	Gust Speed (m/s)	WindDir (Degrees)
During sand	22.2	39.7	1008.7	2.1	9.6	15.4	253.4
No sand	24.2	70.8	947.9	9.5	5.0	18.4	224.6
Overall average	24.2	70.6	948.3	9.6	5.0	18.1	224.8

Table 3.2 - Summarised climate data for Borg El-Arab (2012-2013)

This data indicates that the average wind speed during a sandstorm event for this location is 9.6 m/s, with a yearly average of 5.0 m/s for all conditions. Gusts of up to 25 m/s were also observed which have the potential to damage the

collector surfaces significantly. This fits within the 18 to 29 m/s suggested by the MIL standard.

The second parameter to be established is the amount of sand to use, which may be estimated from observations in the literature. Zhao et al. (2010) measured the sand flux and wind velocity in three areas of the Minqin region in China. One of these is a desert type environment. Wind speeds were measured at various heights, recording approximately 9 m/s at 1 m. This matches with the velocity observed in Alexandria and therefore the characteristics of sand at this height should match that expected in Egypt. Through dust collection, they measured a sand/dust concentration at 1 m height of 104 mg/m^3 in the desert region. Assuming this value for the airborne concentration, moving at a velocity of 10 m/s implies the following

$$\begin{aligned} flux &= concentration \times velocity \\ &= 0.104\ g/m^3 \times 10\ m/s \\ &= 1\ g/m^2/s \end{aligned} \tag{3.6}$$

The area of impact is a 20 mm diameter circle.

$$\begin{aligned} impact\ area &= \pi \times 0.01^2\ m^2 \\ &= 0.3 \times 10^{-3}\ m^2 \end{aligned} \tag{3.7}$$

Therefore the rate of sand impact should be

$$\begin{aligned} rate &= flux \times area \\ &= 1\ g/m^2/s \times 0.3 \times 10^{-3}\ m^2 \\ &= 0.3\ mg/s \end{aligned} \tag{3.8}$$

Over one hour the mass of sand blown is therefore $0.3\ mg/s \times 3600 \approx 1\ g$.

From the Alexandria weather data there were 46 hours of sandstorm per year on average implying that for simulating a year of exposure, 46 g of sand is appropriate.

3.6.4 Erosion tests

Two sets of erosion tests were performed, with high mass and low air speed to simulate extended periods of time, and low mass high air speed to simulate gusting winds and extreme but short duration conditions.

To simulate a year of exposure the pressure was set to give an air speed measured at 10 m/s. A mass of 46 g of the MIL sand was used as calculated above. Following the results of this test the remaining tests were done using masses less than 4 g over a range of air speeds, as shown in the test summary Table 3.3.

Sample	Air velocity (m/s)	Sand mass (g)
1	10	46
2	5	4
3	10	4
4	15	4
5	20	4
6	25	0.1
7	25	0.5
8	25	1.0
9	25	0.5
10	30	0.5
11	20	0.5
12	25	0.2
13	25	0.3
14	25	0.4
15	25	0.6
16	25	0.7
17	25	0.8
18	25	0.9
19	25	1.5
20	25	2.0

Table 3.3 - Erosion tests performed

Varying speeds and masses were used to determine the point at which damage begins to occur and how it accumulates to reduce the reflectance of the mirror.

3.7 Surface analysis

3.7.1 Overview of reflectance measurements

The reflectance is measured using a spectrophotometer, Jasco FT/IR-6200 V-670 (Figure 3.16), covering a spectrum from 200 nm to 2500 nm. This allows the entire solar spectrum to be analysed with a resolution of 0.5 nm. Small samples of the mirror have been cut for these measurements. As the mirror has a silver backing, the total reflectance spectrum expected will be made from a combination of a silver reflectance spectrum and the transmission spectrum for float glass.

The undamaged samples are cleaned and then all have their hemispherical and specular reflectance measured. It is expected that, as the mirror samples are cut from a single larger mirror facet, the samples are uniform in undamaged reflectance between each other. These measurements are done using the same reference mirror to ensure consistency between measurements.

Figure 3.16 - Jasco spectrophotometer V-670

The undamaged samples are subjected to the accelerated aging tests to varying amounts, while keeping some samples as controls. These controls are

then used as the reference mirrors for measuring the damaged samples, allowing a direct comparison as the ageing is performed.

The hemispherical measurement window size matches the size of the damaged area caused by erosion so that only a single position is measureable for each mirror.

3.7.2 Specular reflectance

To measure the specular reflectance an accessory is used with the spectrophotometer. This has a number of mirrors contained within it reflecting the light from the source to strike the sample at a variable angle from 35 to 85 degrees. There is also a variable aperture which may be applied at the sample to limit the area over which the measurement is made. The reflected light then travels to the detector where the intensity is measured. The mirrors that the light reflects from between source and detector do not have perfect reflectances so will contribute to the loss in intensity measured. While these mirrors may be characterised during manufacture of the accessory, their properties will change over time making any adjustment inaccurate in calculating the absolute reflectance of the sample. It is therefore necessary to produce a baseline measurement of a reference surface, which is then used to produce a relative reflectance value for the sample.

The reference surface may be a traceable reflective artefact whose reflectance value is already known and as such will produce a relative reflectance value close to the absolute. It may also be a sample of undamaged sample mirror, which will then produce relative reflectance values to the manufactured state. This allows the reflectance drop to be easily tracked as the mirror is aged to different degrees.

3.7.3 Hemispherical reflectance

The hemispherical reflectance is also measured using the V-670 instrument, this time with an integrating sphere accessory model ISN-723. This has a 60 mm internal diameter integrating sphere with a barium sulphate coating,

suitable for a 250 to 2500 nm wavelength range. The integrating sphere geometry is shown in Figure 3.17.

The sample is placed such that the region of interest is against a window into the integrating sphere and that no light escapes from the edges of the sample. The light enters the integrating sphere through a small entrance port, is reflected from a mirror and strikes the sample. The reflected light is then distributed evenly by the diffuse reflecting walls. The wide field of view of the detector allows it to collect the light from most of the inner surface producing a reflectance value from the scattered light.

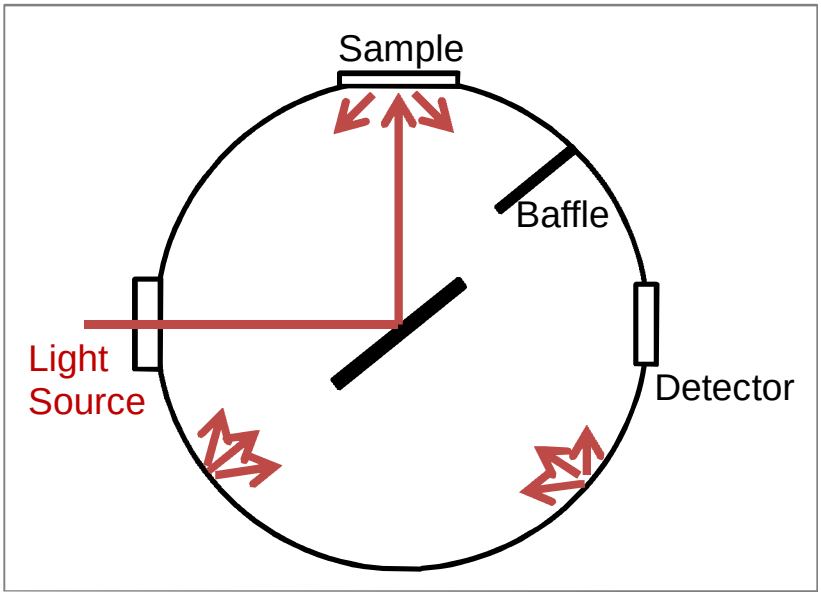

Figure 3.17 - Integrating sphere geometry

The reference surface used for calibration is a sample of Spectralon, a highly diffuse reflective material. It has a reflectance of over 95% across the solar spectrum from 250 to 2500 nm and 99% from 400 to 1500nm as shown in Figure 3.18 (Labsphere, 2013). It is this spectrum that defines the reflectance values measured for each sample. This calibration is done each time the instrument is switched on or the accessory changed.

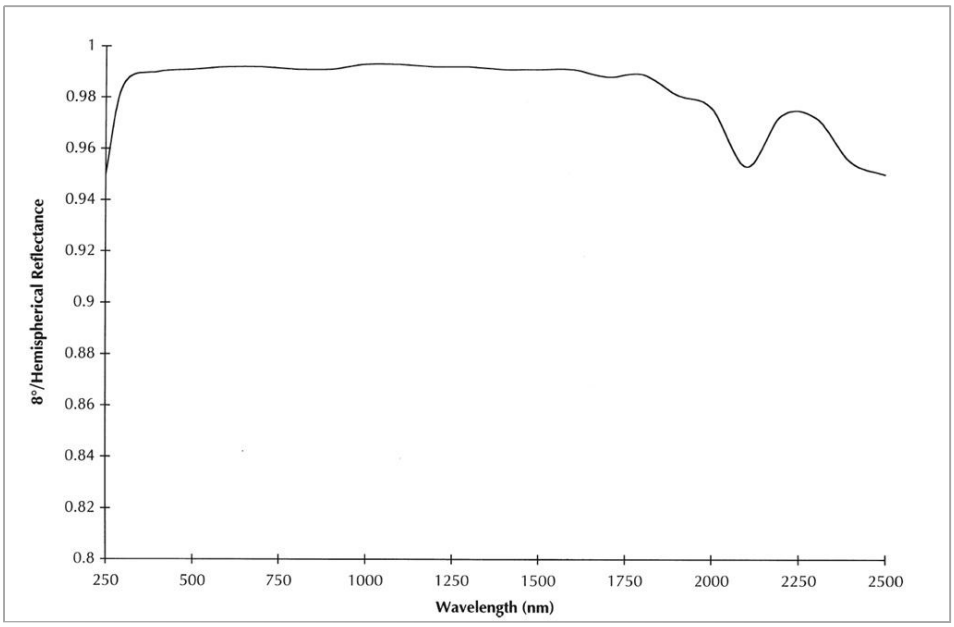

Figure 3.18 - Spectralon reflectance spectrum

3.7.4 Applying a solar weighting

Once the spectra have been recorded, they are weighted with the solar spectrum shown in Figure 3.19 and defined in detail by the ASTM (2003) G173/03 standard tables, giving a percentage reflectance value data point.

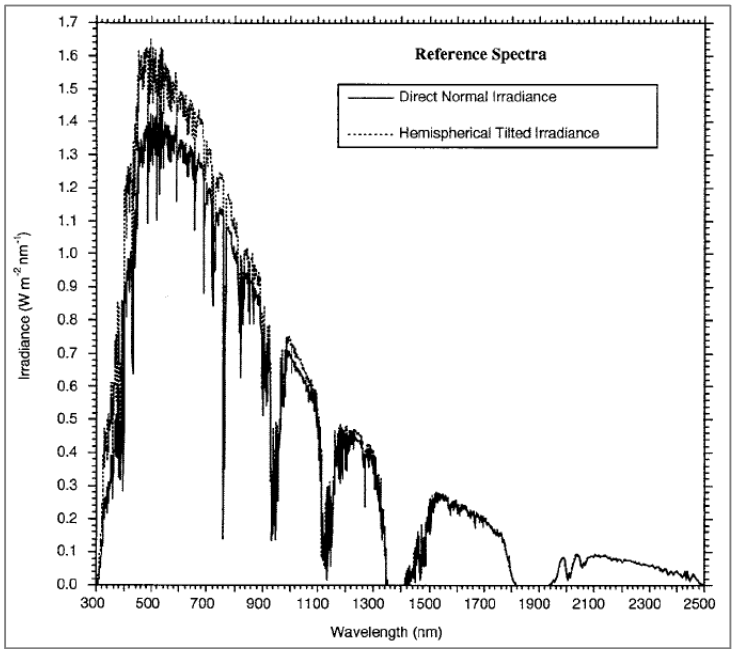

Figure 3.19 - Solar reference spectra

The standard defines the mean value of the reflectance R_s as

$$R_s = \frac{\int_0^\infty R(\lambda)E_\lambda(\lambda)d\lambda}{\int_0^\infty E_\lambda(\lambda)d\lambda} \quad \textbf{(3.9)}$$

where $E_\lambda(\lambda)$ is the solar spectral irradiance defined by the tables given in the standard and $R(\lambda)$ is the measured reflectance spectrum.

As these quantities are measured as discrete values, these integrals are reduced to summations over the range of values, such that

$$R_s = \frac{\sum_{i=1}^{N} R(\lambda_i)E_\lambda(\lambda_i)\Delta\lambda_i}{\sum_{i=1}^{N} E_\lambda(\lambda_i)\Delta\lambda_i} \quad \textbf{(3.10)}$$

where λ_i is the wavelength of the ith point from N measurements (ASTM, 2012).

This produces a single value for the reflectance, which may then be used for comparison between samples. Each spectrum is inspected for unusual features that do not represent a simple drop over the whole spectrum.

3.7.5 Microscopy

The samples were examined under a microscope using lenses of magnifications from 2.5X to 40X. The field of view varies from 6 x 4.5 mm to 300 x 225 µm and is captured with a 2048 x 1536, 3 MPixel sensor. At the highest magnification each pixel represents approximately 0.15 µm. Each lens is pre-calibrated and the appropriate scale bar is added to the image, measurements may also be done within the software with this calibrated scale.

Each sample was imaged using both the high and low magnifications under the same lighting conditions. This ensures consistency between the images both for qualitative study and quantitative analysis and comparison. The size and density of the cracks were compared visually and larger cracks were examined in detail at higher magnification to determine the crack formation mechanisms.

Following the qualitative assessment of the images, they were analysed using the ImageJ image processing software. Each image was converted to a binary image by a threshold value determined by examining the images. As there can be a large variation between the amount of light and dark pixels, best results were obtained by doing this step manually rather than as an automated routine. The particle analysis algorithm was then used to determine the number and sizes of dark patches on the image, corresponding to the cracks formed during erosion. These values were then compared with one another across the different samples.

4 RESULTS AND DISCUSSION

The following chapter contains results on the development and use of both the photogrammetry and ageing techniques. Section 4.1 details the optimisation of the camera settings and procedure, including comparison results to the CMM, details of the measurements taken at a number of sites and discussion of the results. Section 4.2 contains the results from the sand ageing experiments and contains details of the reflectance and microscopy measurements.

4.1 Photogrammetry

Initial photogrammetry tests were carried out using a set of 25 white ceramic spheres attached to the granite bed of the CMM, a highly stable structure which does not change significantly over the course of the measurements. Using these spheres many of the camera settings and elements of the procedure were determined.

4.1.1 Camera settings and procedure

Changing the aperture size affects the depth of focus of the image, which is important to be able to maintain a sharp image across the whole surface. It is possible to predict the approximate aperture size by calculating this depth of focus and also the amount of blur a point will have depending on its distance from the camera. For instance a point which is fully within the depth of focus will be sharp, however a point near the edge or outside the depth of focus will have a certain amount of blur associated with it.

The size of the sphere grid is 800 x 800 mm with a longest diagonal of 1100 mm. This distance must fit well within the field of view of the camera to reduce the image distortions around the outer edge of the lens. This sets the minimum distance at which the photographs must be taken from and depends on the focal length of the camera, which determines the field of view. The focal length of the camera has been set at its repeatable end stop of 18 mm giving a minimum distance to the target of approximately 1600 mm. Using this distance

and the positions of each sphere in the grid, the distance between the camera and each sphere was calculated. For each of the 25 distances it is possible to apply a blurring equation to calculate the size that a point source would appear on the camera sensor. This equation was applied for different aperture settings from f/5 to f/16 and was done for each of the 8 camera positions and a total effective blur was found by adding the contribution from each position. The results in Table 4.1 show that the minimum total blur of 1.05 mm occurs with an aperture of f/7.1 (highlighted in green).

Camera	Aperture										
	5	**5.6**	**6.3**	**7.1**	**8**	**9**	**10**	**11**	**13**	**14**	**16**
1	0.15	0.14	0.14	0.13	0.14	0.15	0.16	0.18	0.21	0.23	0.26
2	0.13	0.13	0.12	0.13	0.13	0.15	0.16	0.18	0.21	0.23	0.26
3	0.13	0.13	0.12	0.13	0.14	0.15	0.16	0.18	0.21	0.23	0.26
4	0.16	0.15	0.14	0.14	0.14	0.15	0.16	0.18	0.21	0.23	0.26
5	0.14	0.13	0.13	0.13	0.14	0.15	0.16	0.18	0.21	0.23	0.26
6	0.15	0.14	0.13	0.13	0.13	0.15	0.16	0.18	0.21	0.23	0.26
7	0.14	0.14	0.13	0.13	0.14	0.15	0.16	0.18	0.21	0.23	0.26
8	0.16	0.15	0.14	0.14	0.14	0.15	0.16	0.18	0.21	0.23	0.26
total blur (mm)	**1.17**	**1.10**	**1.06**	**1.05**	**1.09**	**1.18**	**1.30**	**1.42**	**1.68**	**1.81**	**2.07**

Table 4.1 - Aperture Size vs. Blur

By increasing the shutter speed from 1/60 second to 1/125 second a noticeable increase in the sphere position accuracy was seen from 73.3 microns to 40.7 microns RMS as shown in Table 4.2. The faster shutter speed reduces the amount of light that the sensor receives from the dark background behind the spheres, while having minimal effect on the light apparent from the spheres. This increases the contrast and leads a more accurate centring of the targets by the algorithm within the software. A faster shutter speed will also reduce any blurring caused by motion of the hand-held camera while the exposure is being taken. Though no motion blur is noticeable on the slower shutter speed, this may still have an effect at the pixel and sub-pixel level.

Shutter Speed (s)	Accuracy (µm)
1/60	84.6
1/60	73.3
1/125	40.7
1/125	40.6

Table 4.2 - Shutter speed

The photographs were taken so as to have the light rays connecting the camera and the points close to perpendicular. This is optimal for the intersection calculation within the software and so increases the accuracy of the points. To do this the photographs were taken at an angle of approximately 45 degrees from the horizontal plane of the spheres and at 8 positions equally spaced around the points as seen in Figure 4.1.

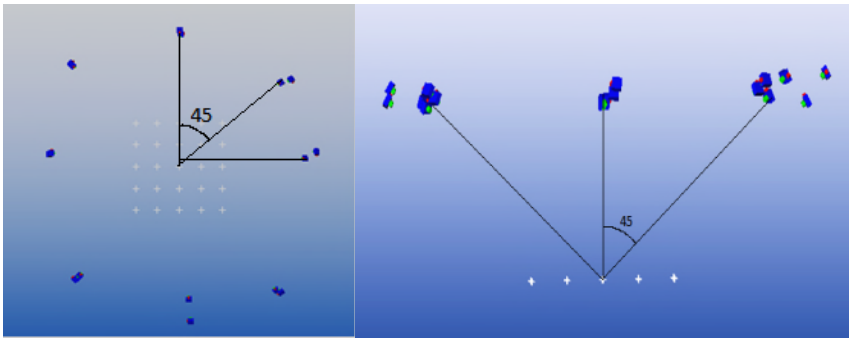

Figure 4.1 - Camera angles

At each of these positions two photographs were taken, one with the camera held in a landscape orientation and the other rolled 90 degrees to portrait. This is an important step in the software camera calibration where lens distortions are calculated and corrected. By implementing this camera roll the accuracy is increased from 60 microns to 40 microns RMS.

To determine the effect that camera calibration has on the error map results and to check its importance, analysis was done using the same images and photogrammetry solution both with the camera calibration applied and without. The difference between these measurements is then the calibration effect and is shown in Figure 4.2. The RMS difference is 12.1 microns for the x, y position,

which is at the level of accuracy of photogrammetry. It is therefore important to carefully consider the camera calibrations as they may causes systematic features in the error maps which are not a true representation of the surface.

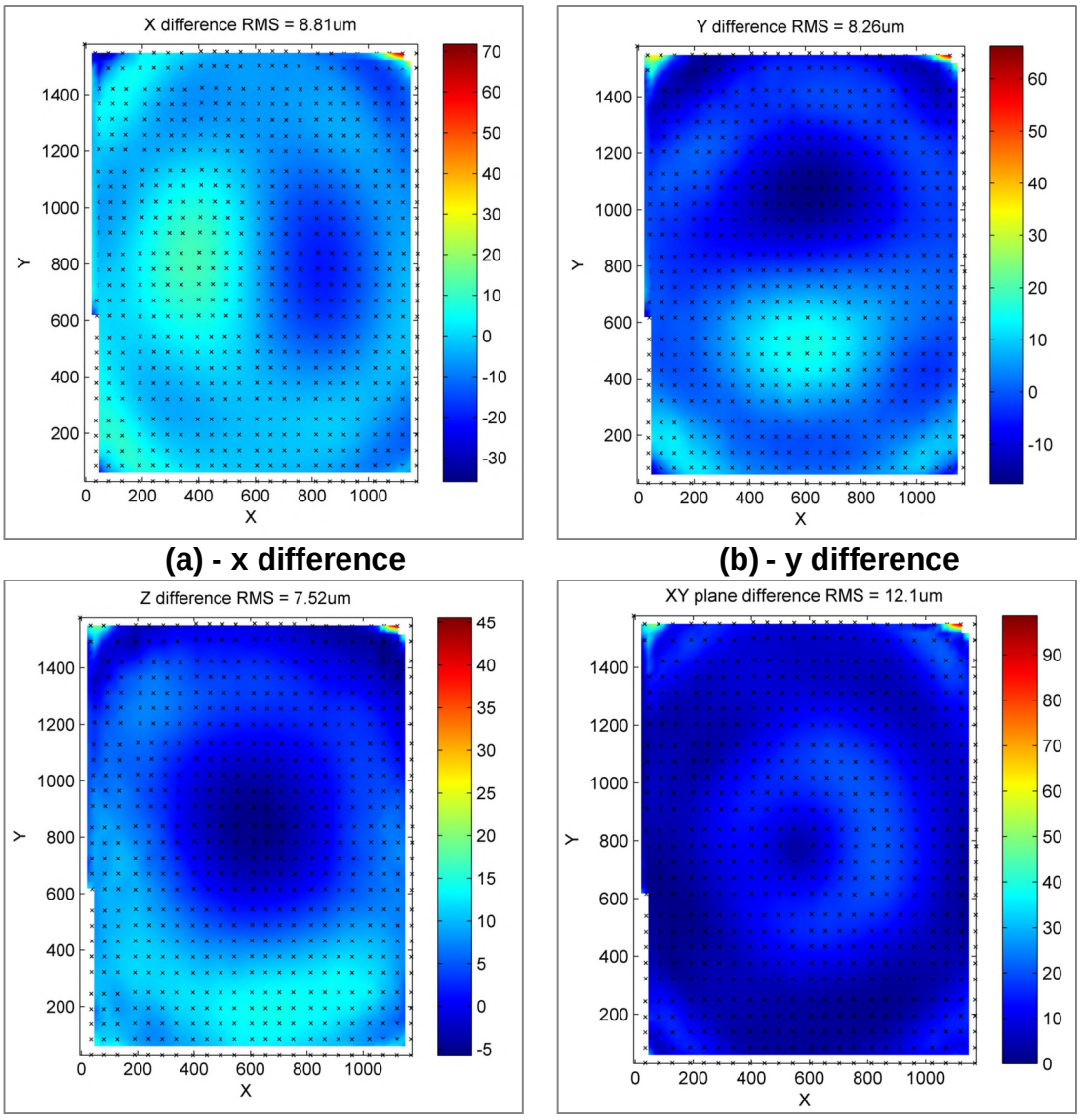

(a) - x difference **(b) - y difference**

(c) - z difference **(d) - xy plane difference**

Figure 4.2 - Camera calibration effects

The targets shown in Figure 4.3 are printed coded targets 20 mm, 15 mm, 10 mm and 5 mm in diameter. The whole grid occupies approximately 1.5 m by 1.2 m representative of the mirror size. Variable sizes are used at the same time within the same sets of images, rather than separately so as to remove any effects that differences in camera positions may have on the results.

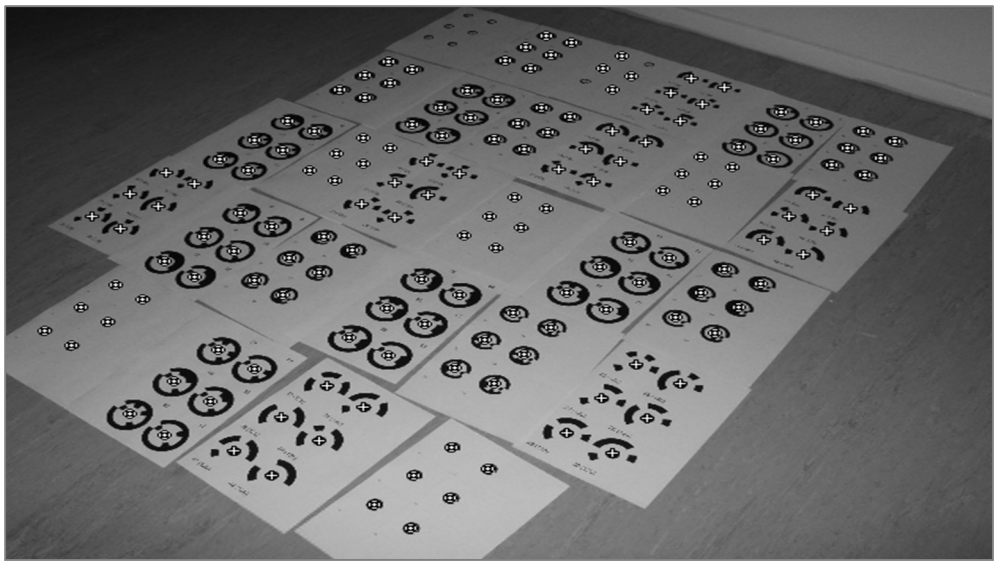

Figure 4.3 - Variation in target size on a 1.5 m grid

Analysis was done using each individual size of targets separately with the software residual results shown in Table 4.3

Target size (mm)	Residual (pixels)
20	0.087
15	0.075
10	0.074
5	0.102

Table 4.3 - Effect of target size on RMS residual

The best point size implied is around the 10 to 15 mm size. Some 5 mm targets were not identified at the far end of the photographs. Some were also incorrectly identified due to poor definition of the coded rings. There is a large decrease in the target diameter from the close edge of the photograph to the far edge from 20 pixels to 6 to 7 pixels. The minimum size required for good target centring is 10 pixels across, implying a minimum target size of around 10 mm taking into account the perspective distance and the elliptical shape of the furthest targets. This matches the results shown above. Doubling the target diameter to 20 mm does not make a large difference in the residuals and will

result in the reduction of the possible density and number of points on the object under test.

4.1.2 Sphere measurements

The coordinate system set up is important in determining the accuracy of the final photogrammetry result. The coordinate system for the sphere measurements was set up using the CMM measured positions of three of the spheres. This was done to quickly and easily align the two sets of point clouds for comparison. The choice of the three spheres impacts the accuracy of the measurement so was investigated. The variables in choosing the spheres are the position of the spheres and the distance between them.

In all cases the spheres were placed one at the origin and one along each of the x and y axes. The distance along the x and y axes was varied from 200 mm to 800 mm and the accuracy recorded in relation to the CMM. Table 4.4 shows the results for each coordinate system (CSY) length for 4 repeat measurements, their averages and standard deviations.

Repeat number	CSY length (mm)			
	200	400	600	800
1	94.6	96	44.3	41.1
2	78.9	80.7	38.9	40.6
3	107.8	84	38.3	40.5
4	78.3	82	39.5	40.9
Average	89.9	85.7	40.3	40.8
Standard Deviation	14.1	7.0	2.7	0.3

Table 4.4 - CSY distance variation (dimensions in microns)

The accuracy increases with the CSY distance up to 600 mm and slightly decreases for the largest size. The length of the CSY determines the scale that is applied to the point cloud so when using the 200 mm CSY this length is multiplied by 4 to calculate the scale at the 800 mm points. Therefore any error in locating the 200 mm points will also multiply and have a large effect on the scaling of the grid. When using the 800 mm CSY there is no scaling up of any

errors, making these CSY points more accurate. The decrease in accuracy seen past 600 mm is due to the 800 mm spheres being at the corners of the sphere grid. These corner points are not as accurate as those closer to the centre as the camera is focused at the centre of the grid. Additionally there is a larger camera lens distortion towards the outside of the field of view, where the corner points are located. This point quality is shown by the photogrammetry software RMS residual and is shown in Figure 4.4. Each circle represents one of the spheres in its corresponding position in the 5 x 5 grid, contained within is the RMS residual in pixels. Highlighted in red are those spheres with residuals greater than 0.1 pixels and in green are those less than 0.05 pixels, showing the greater quality toward the centre.

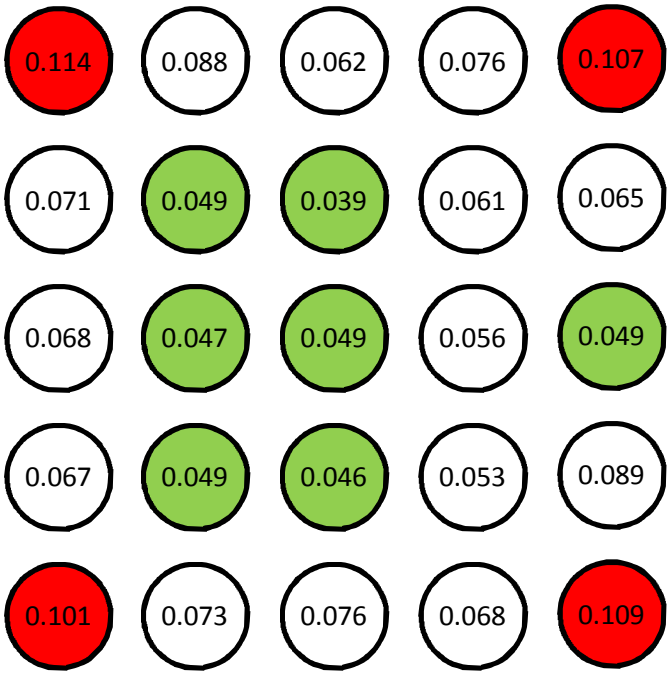

Figure 4.4 - RMS residuals over sphere grid (in pixels)

Placing a 200 mm CSY at the centre produced an RMS accuracy of 36 microns and a 400 mm CSY placed at the centre produced a 30 micron RMS accuracy. Based on these findings the ideal position for the scale bar would be in the centre of the image where the points have highest accuracy. However, this is not practical for use on the large mirrors as there is no suitable mounting point in the centre of the glass for any externally used scaling artefact.

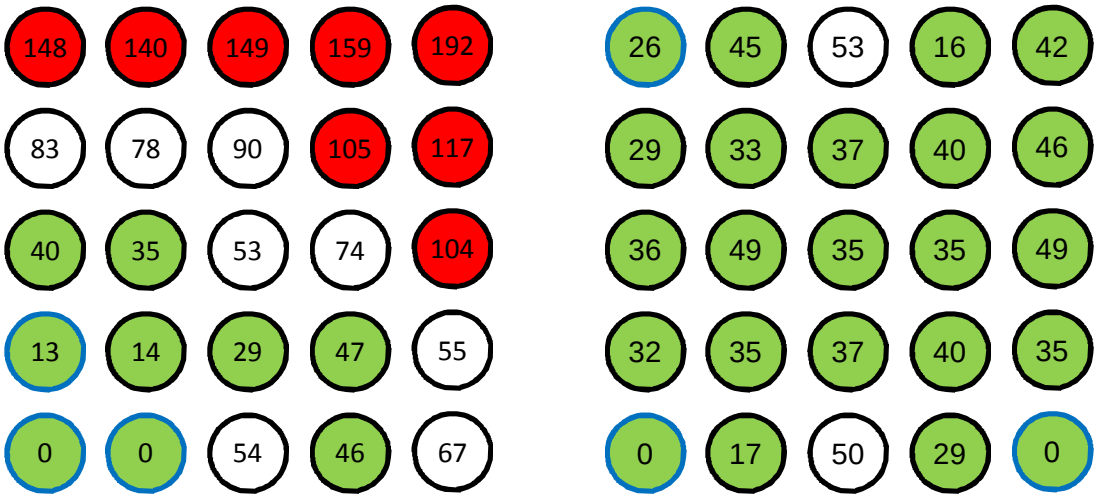

Figure 4.5 - Sphere errors in microns between photogrammetry/CMM for a 200 mm CSY (l) and 800 mm CSY (r)

Figure 4.5 shows the individual sphere errors across the 5 x 5 grid for the 200 mm CSY and the 800 mm CSY. Highlighted in red are those points with an error greater than 100 µm and in green are those less than 50µm. It is clear that when the smaller CSY is used there is a large error at the opposite corner, whereas with the large CSY the error is reduced and evenly distributed. The spheres used as CSY points are outlined in blue.

The measurements were done using the camera settings found previously of aperture f/7.1, shutter speed 1/125s, target size 10 mm, 8 photograph positions with 2 roll angles at each.

Based on the results found, the accuracy of the photogrammetry measurement points is 40.8 microns RMS with a standard deviation of 0.3 microns over the 800 mm square grid. Such accuracy is well within the defined requirement for measuring the parabolic mirrors.

It is clear from these results that a coordinate system should be set up using points separated as much as possible. Such points should be placed at the corners of the mirrors, or the corners themselves identified and used.

4.1.3 Photogrammetry validation with the CMM

Repeat measurements were taken with the CMM and the results are shown in Figure 4.6. The RMS z values over 8 repeat measurements with the CMM with an RMS over all points of 1.2 µm.

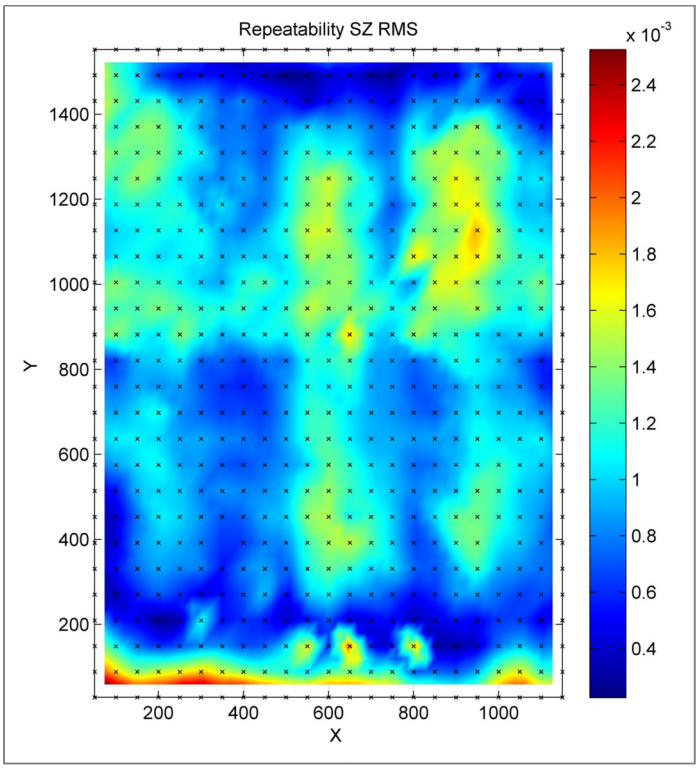

Figure 4.6 - CMM repeatability in z (mm)

These measurements were done with the target sheets already attached to the mirror surface. The thickness of the target sheets was 100µm and its compressive flexibility contributes to the increased variation in successive measurements, over the expected sub-micron level for the CMM. The x and y repeatability can be seen in Figure 4.7, with RMS values of 0.3 µm and 0.8 µm respectively, at the expected level for the CMM. Initially 10 repeat measurements were done, however it was noted that the first two measurement results were different by 10 µm to the remaining 8, much greater than the expected repeatability of the CMM. These two first results were therefore excluded from the averaging, as this is likely due to the mirror settling on the granite bed.

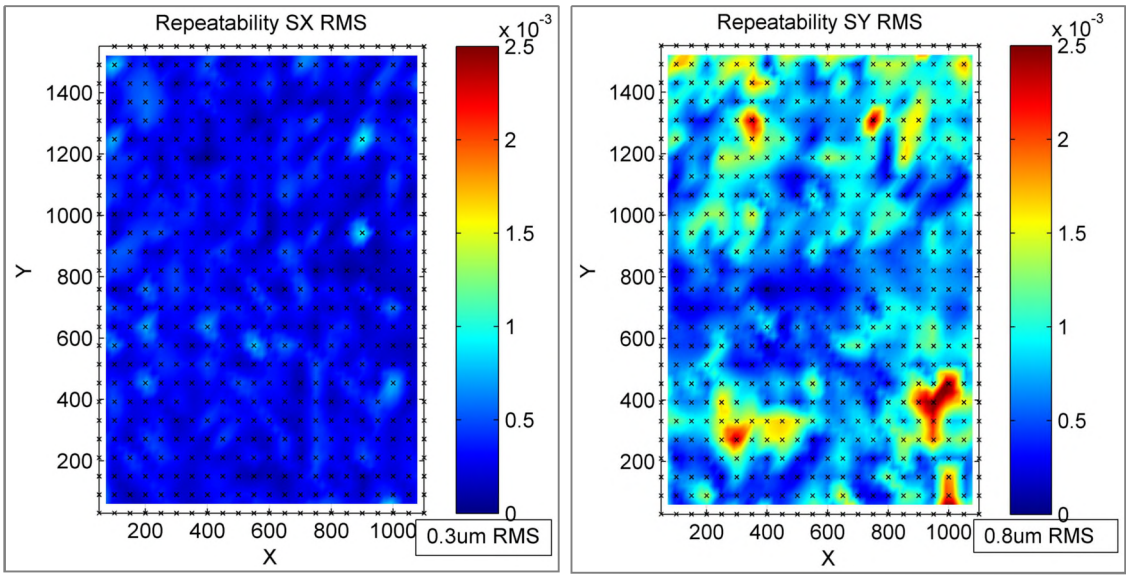

Figure 4.7 - Repeatability in x and y directions (mm)

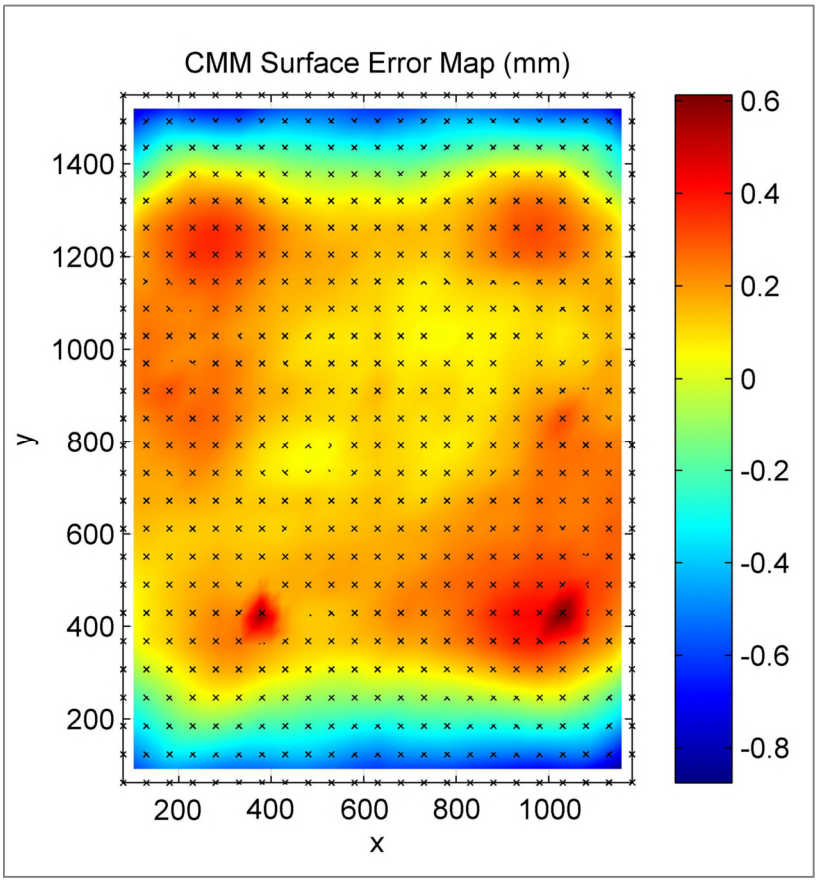

Figure 4.8 - CMM error map

Figure 4.8 shows the error map produced from the averaging over the 8 CMM measurements calculated as the departure from the ideal parabolic equation.

The map is formed from a 23 x 26 grid with 50 mm spacing in x and 60 mm in y. The two anomalous points seen in Figure 4.8 appear here as raised points, again indicating that these are caused by bubbling, which can be seen on further inspection as shown in Figure 4.9 as distortions in the elliptical appearance of the targets.

Figure 4.9 - Target sheet bubble

Photogrammetry repeatability measurements were done away from the CMM on the granite surface table shown in Figure 4.10. This provides a flat, stable test surface, much like the CMM bed.

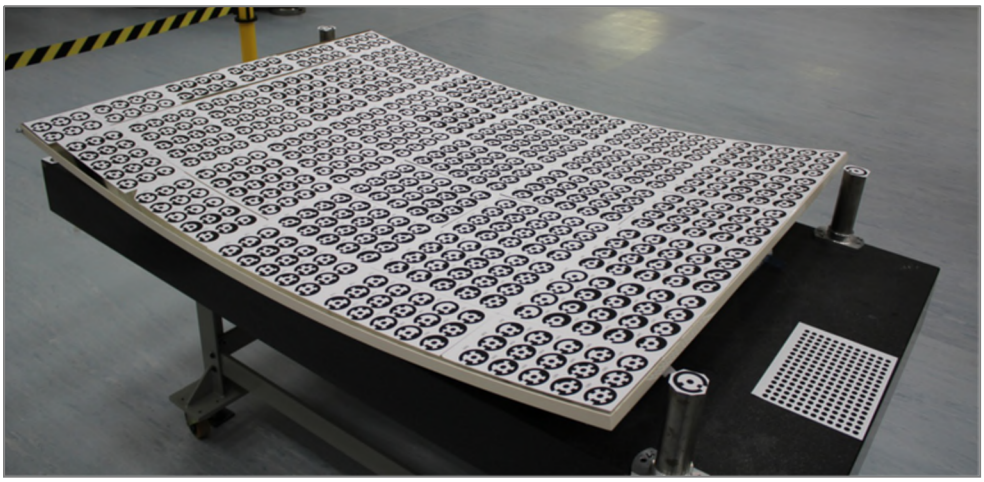

Figure 4.10 - Mirror on granite surface table

Three additional posts were used of the same height with a single target placed on each. This was to provide a common set of points which could define the coordinate system regardless of any distortions which may be applied to the mirror.

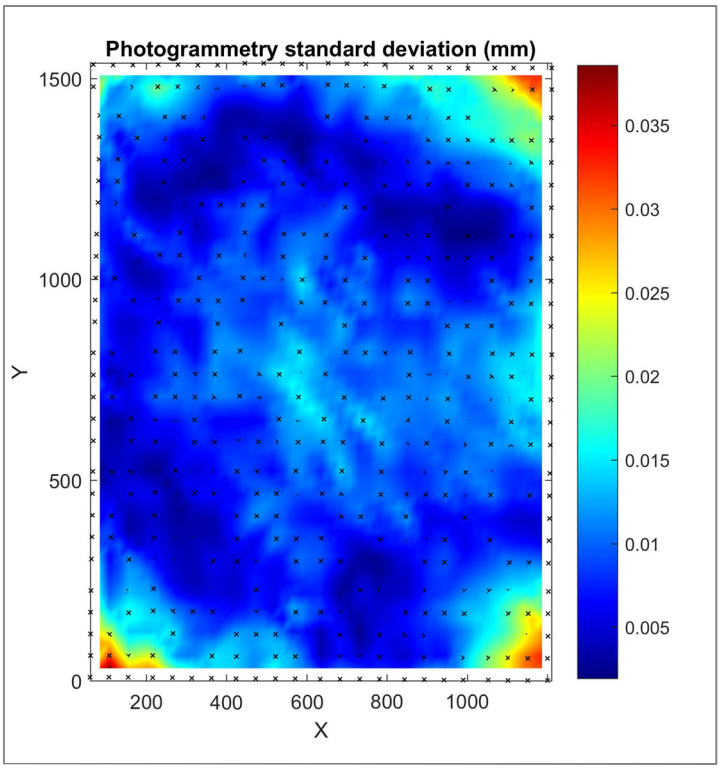

Figure 4.11 - Standard deviation in the Z direction (mm)

Photogrammetry measurements were repeated 5 times on the undistorted mirror. By aligning the point clouds using the three corner posts, the repeatability was investigated. The point cloud was not aligned to the parabolic shape. Figure 4.11 shows the standard deviation in the z direction. The maximum variation occurs at the corners at 40 µm with the overall RMS deviation at 10 µm. Figure 4.12 shows that the maximum variation in the x direction occurs at the left and right edges and is of 100 µm, with an overall RMS of 47 µm. The maximum variation in the y direction occurs at the top and bottom edges at 200 µm with an overall RMS deviation of 87 µm. Each direction show larger variations away from the central area of the mirror, as does the vector distance map. The Z deviations are much lower than those seen in the X and Y directions. The variations seen moving away from the central area are most likely due to the lower residual present nearer the focal position of the camera and towards the central area of the lens, where the points are generally better. There will also be a contribution to this variability in the scaling of each point cloud, due to the reliance upon only a few key points. If the scaling were to vary this would explain both the directionality of the variations, as well as the difference between the different directions. The maximum distance in the z direction is 10 times smaller than that in the other two directions.

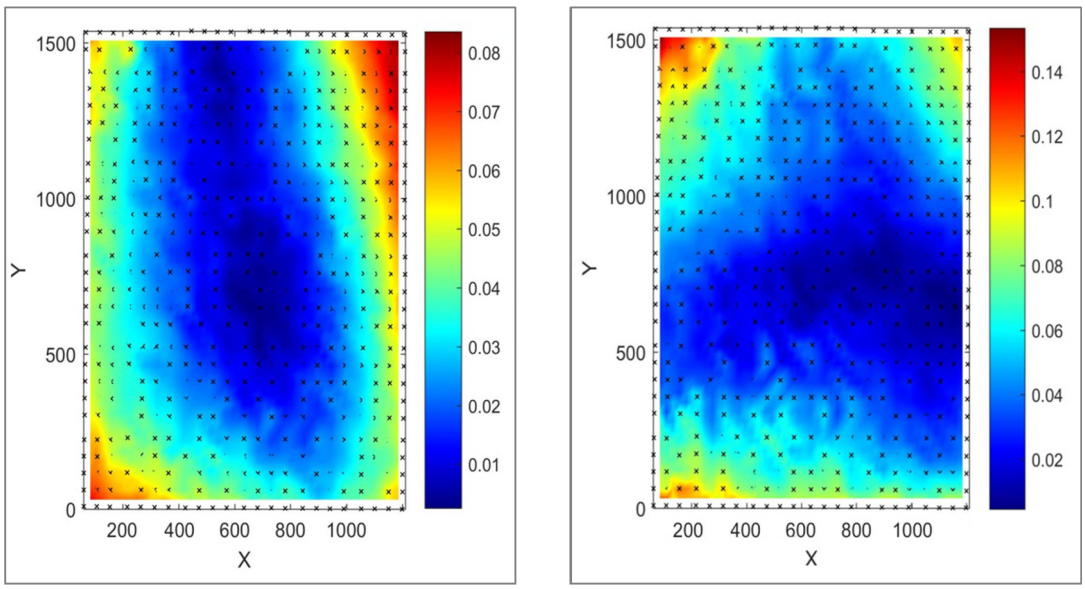

Figure 4.12 - Standard deviation in the x (l) and y (r) directions (mm)

These photogrammetry repeatability tests were repeated on the CMM with much smaller variations as can be seen in Figure 4.13. SD is defined as the vector deviation such that $SD^2 = SX^2 + SY^2 + SZ^2$.

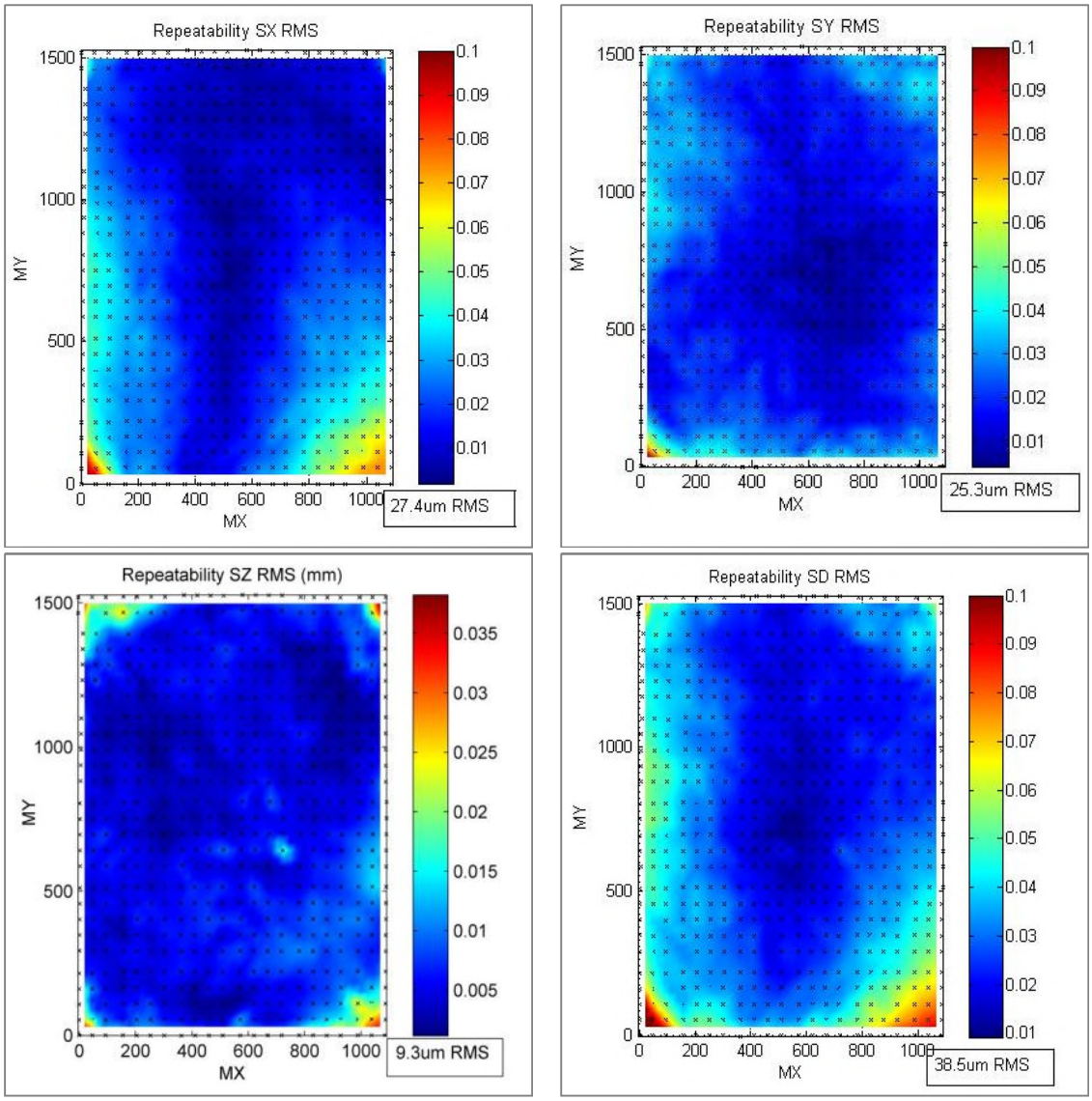

Figure 4.13 - On CMM repeatability

In this case the alignment was done automatically and free rotation and translation were allowed, this minimised the variation between repeats by not relying on three points alone. MX and MY refer to the mean x and y values taken across all the repeat measurements.

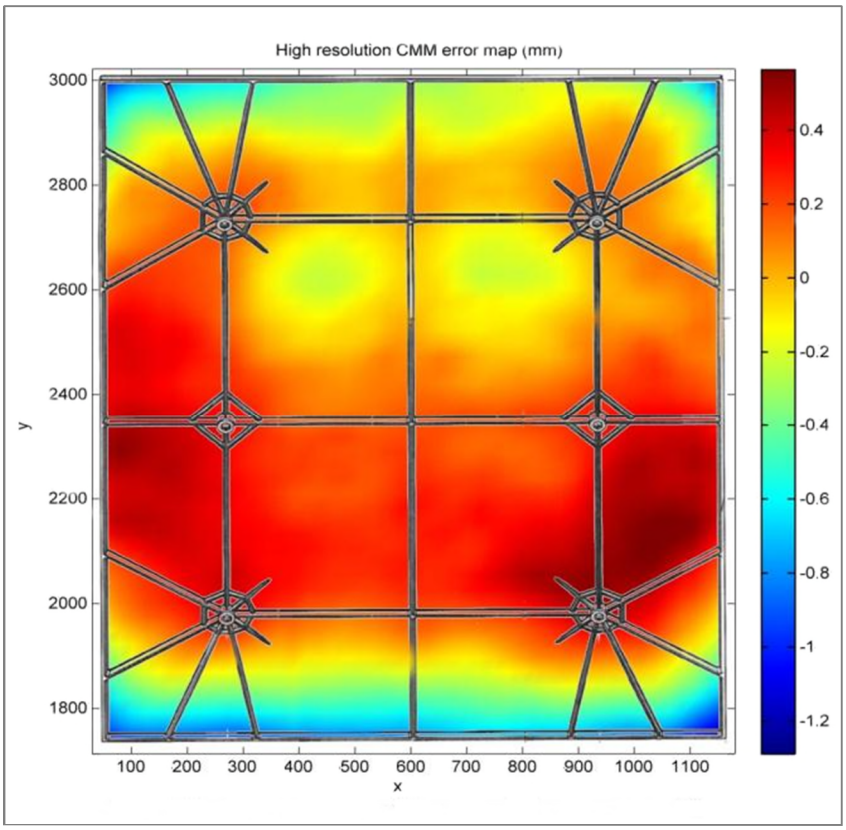

Figure 4.14 - High resolution CMM error map

Figure 4.14 shows a CMM error map measured on the second upper mirror, which continues the parabola to the edge of the trough. This has been measured with a point spacing of 10 mm in x and y. This shows more clearly the effect of the ribbed structure in the central vertical line and the variations around the support points.

Figure 4.15 shows close ups of the top left corner of Figure 4.14, clearly showing the effect of the supporting rib structure on the shape of the mirror. Figure 4.15b shows the results of an edge detection algorithm which displays more clearly the contours of the effect of the structure. The magnitudes of these variations is of the order of 50 to 100 μm in height with a length of approximately 50 to 100 mm, which are small when compared to the millimetre scale distortions expected and so are likely to not be seen. They are also of the order of the accuracy of photogrammetry and would require significantly dense targets to be seen.

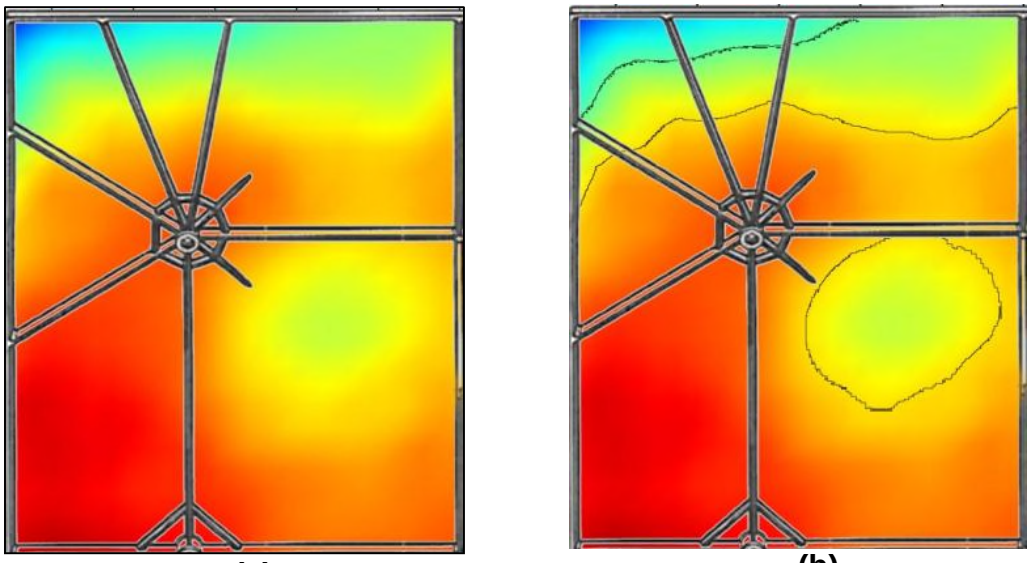

(a) (b)

Figure 4.15 - Close up of high resolution CMM map

The photogrammetry error map is shown in Figure 4.16.

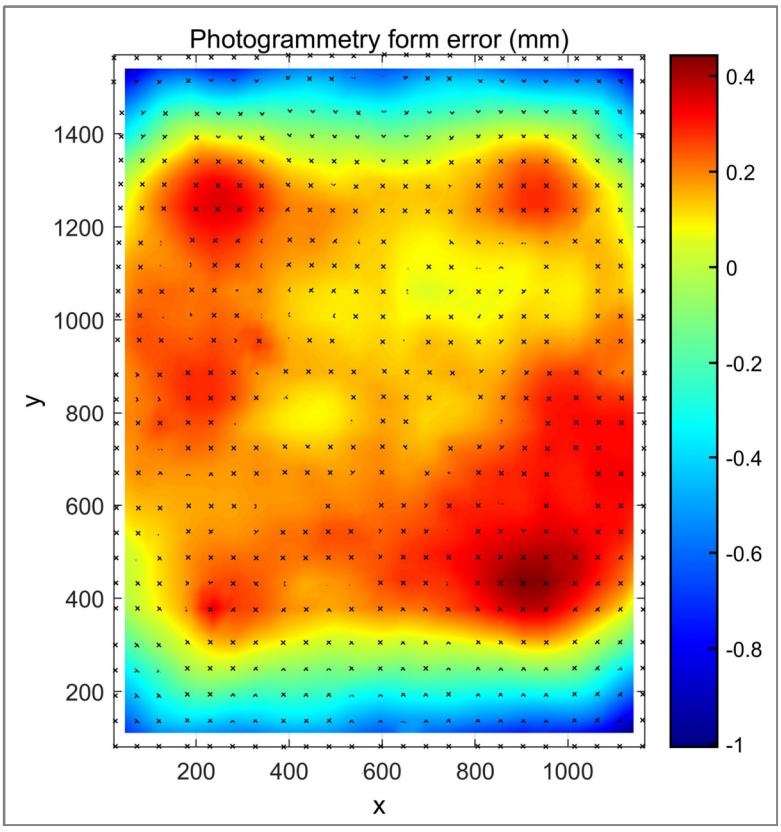

Figure 4.16 - Photogrammetry form error map

This is formed by rotating the point cloud such that it fits onto the parabolic equation $y = x^2/4F$ with minimal deviation and a focal length of 1810 mm. This error map is clearly curved in the y direction indicating an overall focal error on the mirror (Figure 4.17). The peak-valley error is 1.4 mm, with an RMS value of 0.44 mm overall. This indicates that the photogrammetry requirements are for a measurement accuracy in the region of 44 µm RMS.

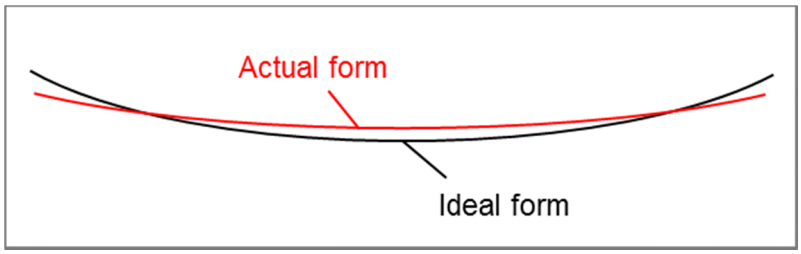

Figure 4.17 - Form error

If the focal length is allowed to vary in the fitting algorithm this curve error is removed and the underlying waviness is revealed in more detail as shown in Figure 4.18. The high points which remain are in the positions of the four corner support points and are due to the weight of the mirror. The peak-valley error is now 0.9 mm, with an RMS of 0.16 mm.

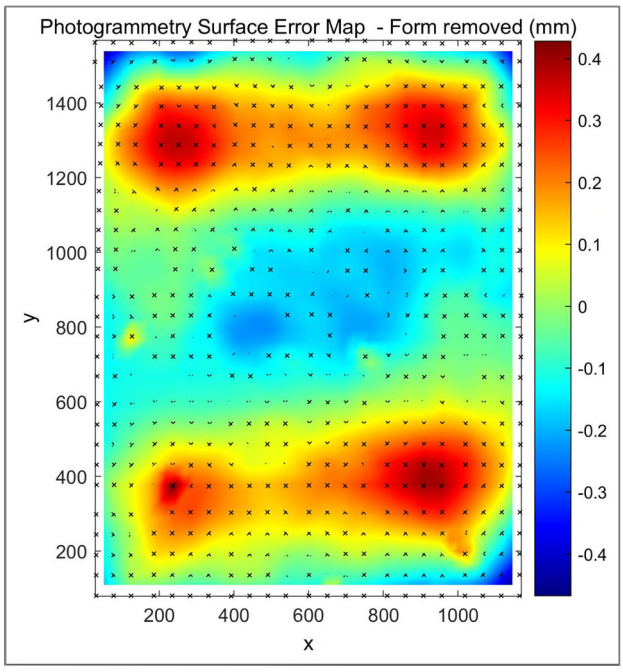

Figure 4.18 - Photogrammetry error map - form removed

The photogrammetry and CMM results are compared against each other by using the generated error maps, which are averages over 5 repeats themselves. Due to the different positions and densities of measured points each point cloud was interpolated to the same set of x and y coordinates. So as to only perform this interpolation once, the photogrammetry surface map is interpolated to the CMM x and y values. The corresponding z values are then subtracted with the result shown in Figure 4.19.

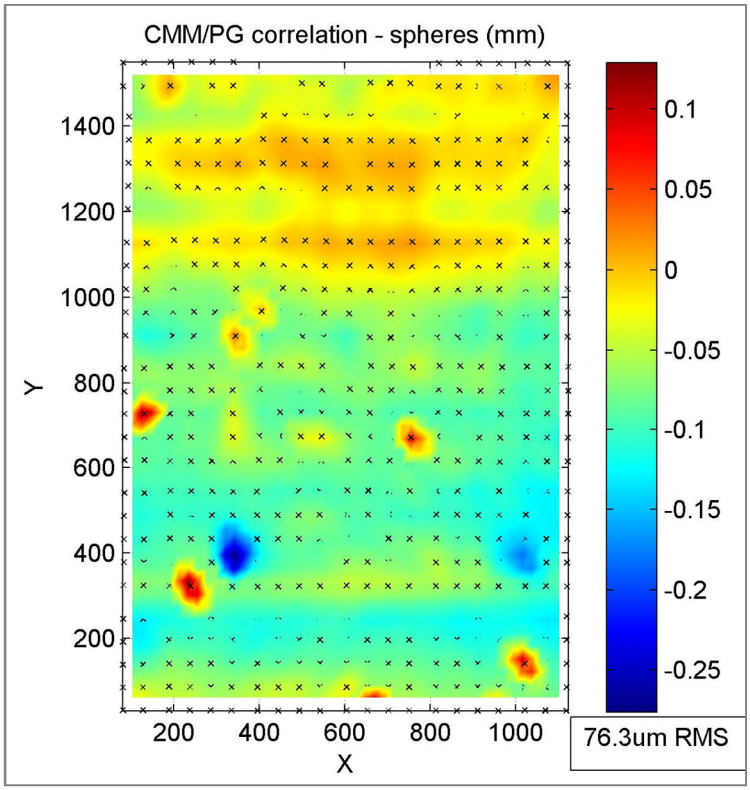

Figure 4.19 - Correlation between CMM and photogrammetry

The peak to valley correlation is 0.4 mm with an RMS of 76 µm. There are a number of anomalous points which appear as either red or dark blue. These are likely caused by bubbles, where the photogrammetry and CMM results may differ by compression of the bubble by the probe. A bubble may also cause a distortion in the viewed target, which may cause the software to calculate its position incorrectly. Each point was identified using its unique coded number, checked on the mirror itself and then excluded from further calculations. The correlation is 20 times less than the peak to valley value observed in the form

error maps, and 5.7 times less than the RMS value. There is some pattern in the correlation map, particularly some horizontal striping and a slight vertical variation. There is no radial dependence visible, which shows that the camera calibration was successful.

The local slope in the curved direction at each measured point was calculated from the photogrammetry point cloud data by interpolation between neighbouring points. The deviation of this measured slope from the ideal slope calculated from the parabolic equation was then found to produce a slope error map for the photogrammetry measurement, which is shown in Figure 4.20

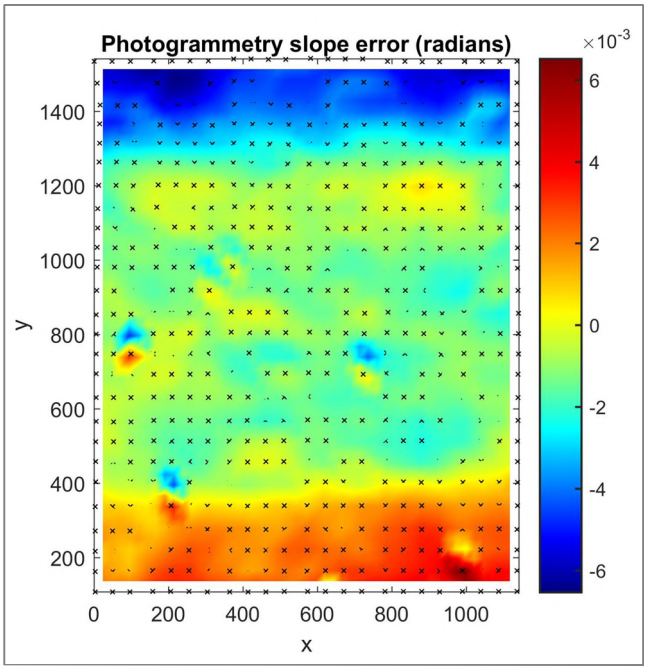

Figure 4.20 - Photogrammetry slope error

The peak to valley slope error is 12 mrad, with an RMS of 2.7 mrad. The largest slope errors occur at the top and bottom of the mirror and are due to the incorrect focal length seen in Figure 4.16. This slope error causes defocus and it is in these regions that most of the mirror efficiency is lost.

Performing a ray trace by using the calculated slopes of the point cloud produces the images shown in Figure 4.21. The inset figure details the absorber tube ideal location and shows both the inner steel and outer glass tubes. All the

light rays appear to hit the steel tube, but there is a clear difference in the focal position from the centre of the tube.

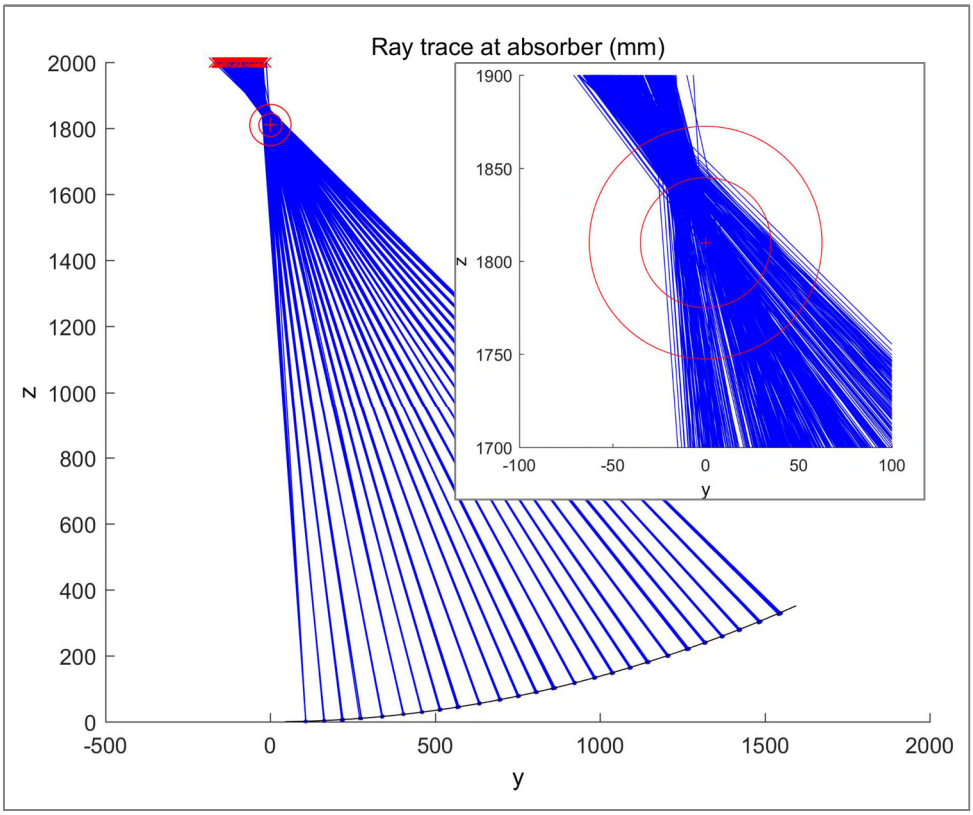

Figure 4.21 - Ray trace for photogrammetry

4.1.4 Effect of external factors

To investigate the flexibility of the mirror facet some distortions were introduced at the support points by using thin pieces plastic sheet of known thickness called shim. The mirror was first measured on the surface table with no shim, then different thicknesses were placed under different support feet. The posts were used to define the coordinate system as these were the only points which were certain to be unmoved by the mirror distortions. The surface maps between undisturbed and disturbed mirror states could be directly subtracted to see how each point has moved under the distortion. Figure 4.22 shows the z distortion caused by a 250 μm shim placed under the bottom right support at (900, 350). This results in a distortion of 0.58 mm which radiates from the nearest corner, spreading across most of the mirror. Based on these results it is

expected that adjustments may be performed by considering the errors at the corners and applying a displacement approximately half of the measured error to the corner supports. This would bring the corner positions into place and any top to bottom error may then be corrected by adjusting the middle supports accordingly.

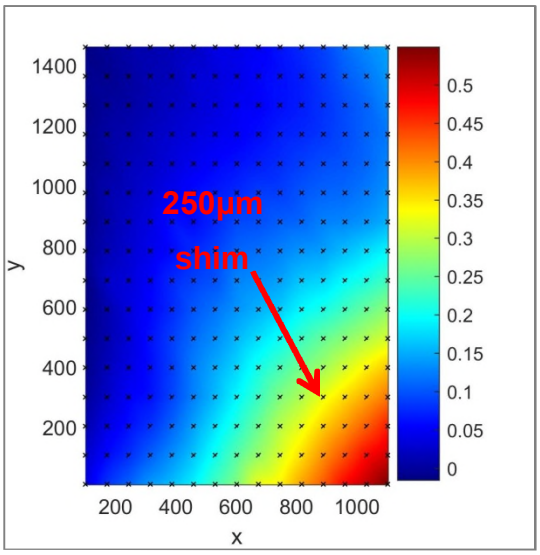

Figure 4.22 - 250 µm corner shim test (mm)

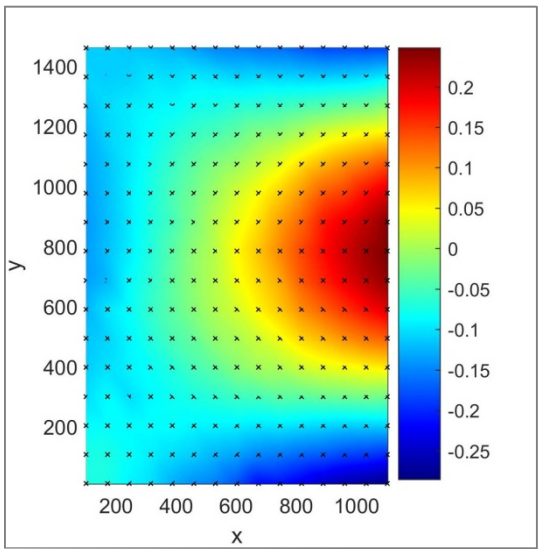

Figure 4.23 - 250 µm middle shim test (mm)

Figure 4.23 shows the same 250 µm shim placed under the middle right support, resulting in an inverse distortion above and below, which is the same magnitude as the shim thickness. There is little distortion on the opposite edge of the mirror.

4.1.5 Preliminary site tests

This section details preliminary site testing which was performed on a linear Fresnel collector in Pakistan, a parabolic trough collector and a point focus linear Fresnel both in Saudi Arabia.

Upon coarse visual inspection of the linear Fresnel glass mirror strips it is clear that each strip has large sag, which will produce defocus as shown in Figure 4.24. The strips are also irregularly spaced, with some gaps much larger than others.

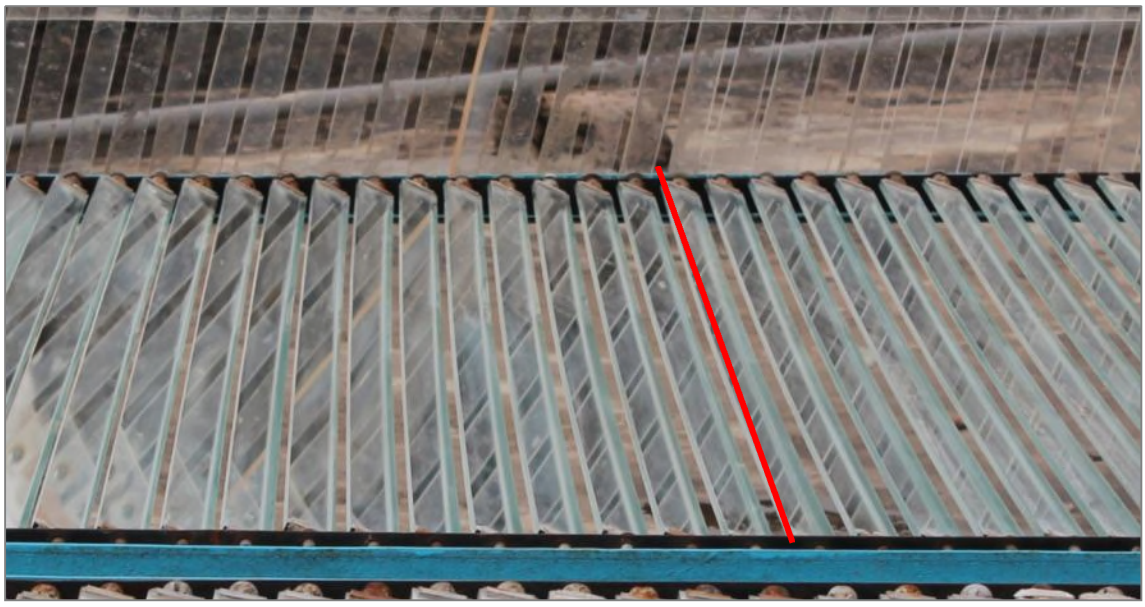

Figure 4.24 - Linear Fresnel sag

An issue seen, which is worst during early morning and late afternoon, is that of target blocking by neighbouring mirror strips. For a normal linear Fresnel collector the gap between the mirrors increases further away from the absorber ensuring that there is no shadowing of the mirrors and all the light reaches the absorber. However, as all the strips are equally spaced in this case, there is significant shadowing. This causes some blocking of parts of the target discs even for high camera angles away from the absorber. This has the effect of either causing the target to be ignored if a large part of the disc is obscured, or if only a small part of the disc is cut off the centring algorithm will place the point away from the actual centre. This effect may be mitigated by changing the camera positions; however the camera positions are limited due to the size of the linear Fresnel array and inaccessibility of those positions in the middle of the mirrors.

When focusing the mirrors onto the absorber, a band of light approximately 70 to 80 mm wide was seen with a central bright section approximately 30 to 40 mm wide. The main absorber is 50 mm wide indicating that the bright region is focused correctly but some light is lost. It is unknown how well the mirrors were focused or how much time was spent adjusting them.

Three sets of measurements were done, at 11:25, 13:50 and 17:00 Islamabad local time. This was done so as to have different mirror positions for comparison. The targets were not removed between measurements for direct comparison. Only 7 camera positions could be reached making a total of 14 photographs for each measurement. The points were paired across each strip allowing a calculation of the mirror angle to be made for each pair. Using a global positioning system location and the time of day the elevation angle of the Sun was calculated making it possible to then perform a 2D ray trace from the mirrors towards the absorber. Figure 4.25 shows the target layout and the sections referred to below.

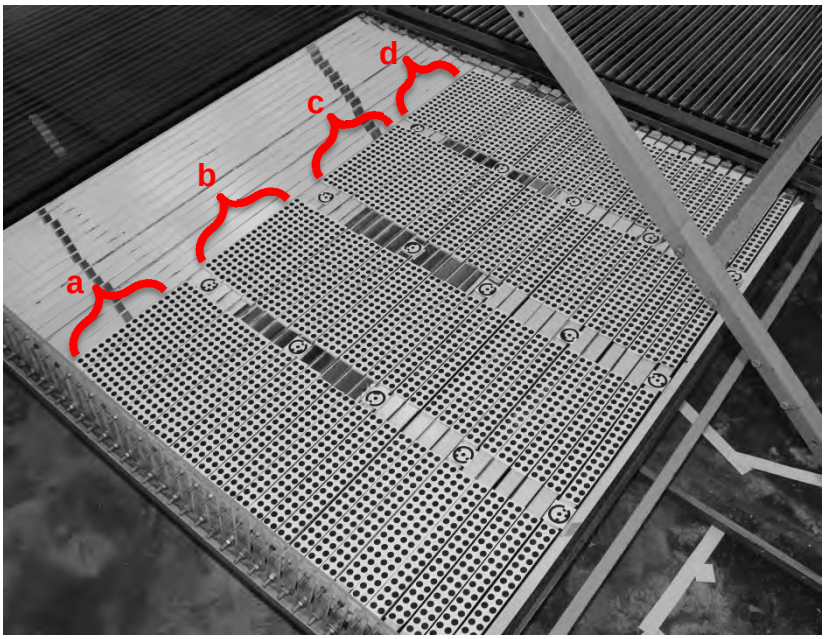

Figure 4.25 - Linear Fresnel target setup

Figure 4.26 shows the result from the 11:25 measurement. The majority of the light rays pass through a section that is approximately 150 mm wide between y = 1150 mm and y = 1300 mm with some passing at around y = 1000 mm. This is much larger than the 50 to 80 mm light band seen on the absorber. There also appear to be many rays which trace well outside the 150 mm width, which are likely to be anomalous points requiring further investigation into their validity.

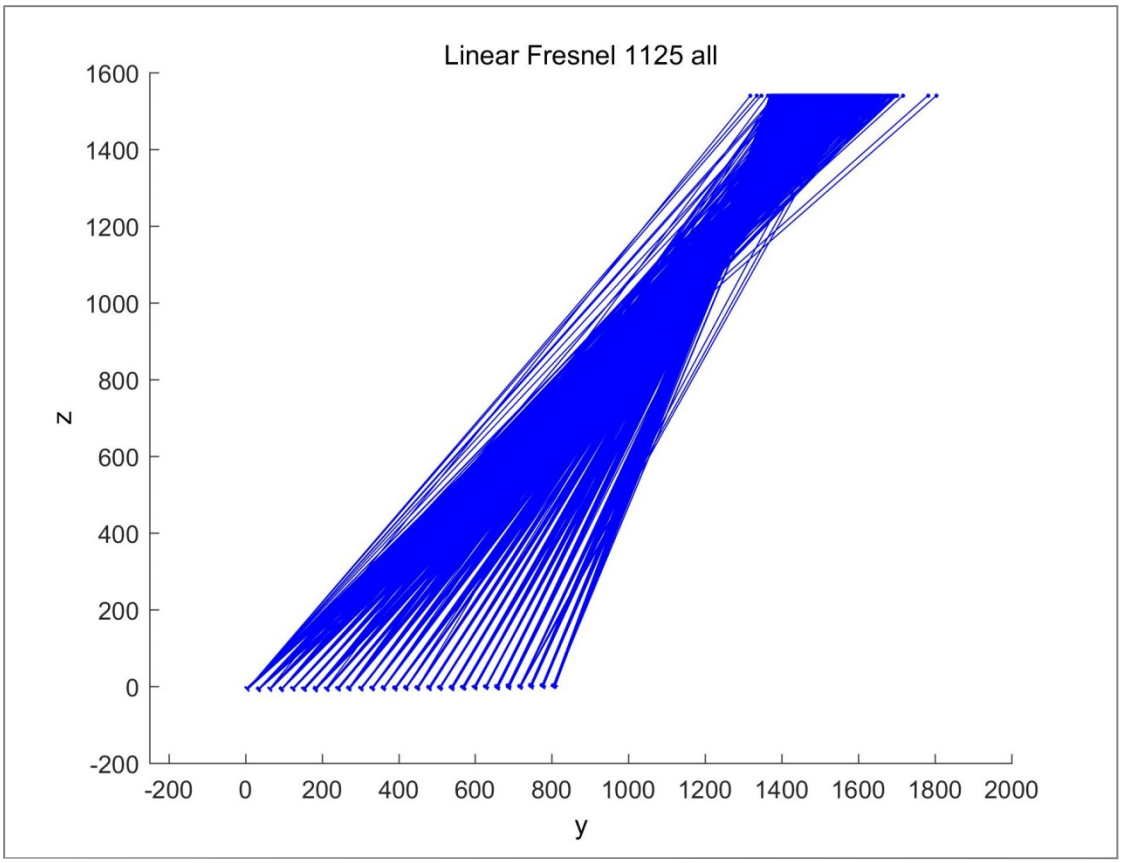

Figure 4.26 - Linear Fresnel ray trace at 11:25

Figure 4.27 shows a plot for each of the four sections (a,b,c,d) seen in Figure 4.25 showing varying widths of focus. The best focus is in section b with a width of 50 mm and few outside. The worst focus is section c with a total width of over 300 mm. In Figure 4.27a there are two ray that are noticeably outside the focal section, these are likely errors and looking back at the original photographs it is clear that these targets have lifted from the surface and so are invalid, which may be seen in Figure 4.28. This also indicated a possible cause for the large difference in focus between the sections, where the latter two sections have many more lifted target discs.

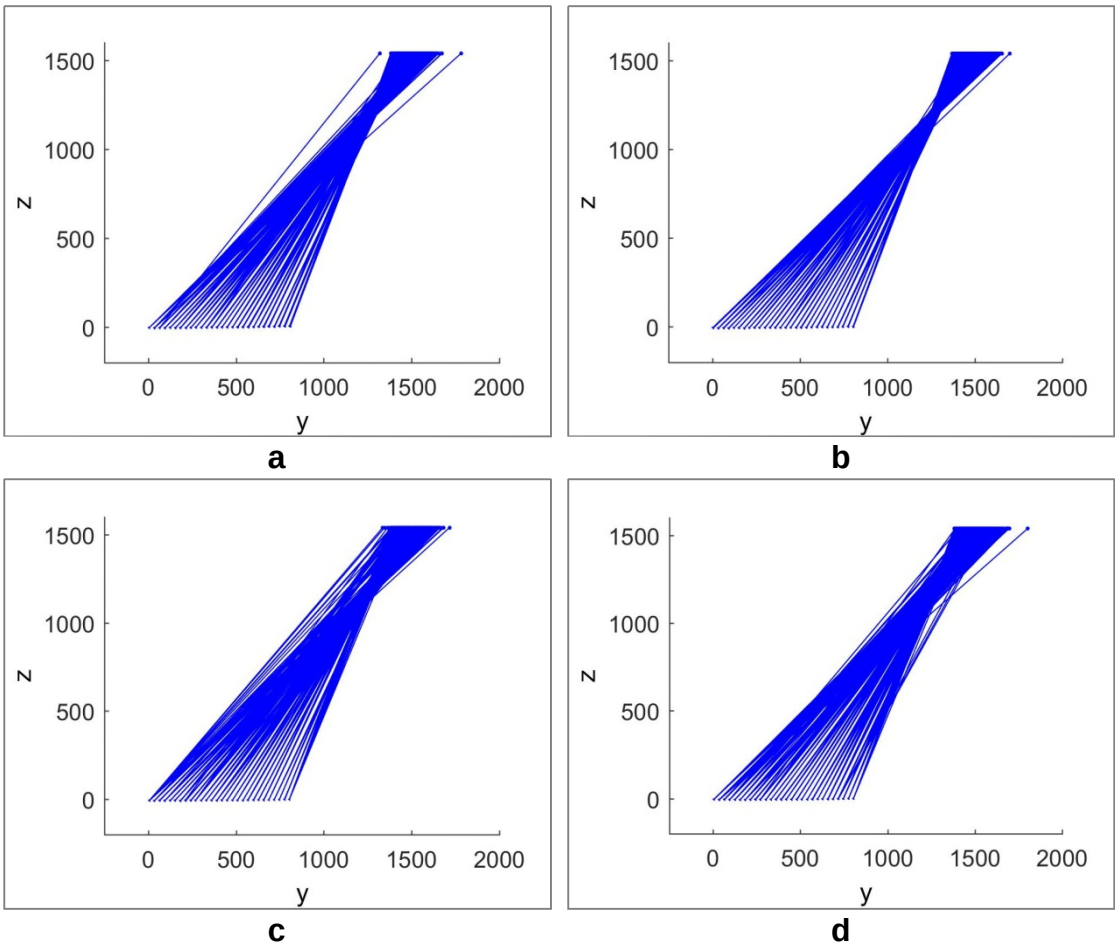

Figure 4.27 - Separate sections of targets

The points for each strip were separated and the shape investigated, an indication of the sag is shown in Figure 4.29.

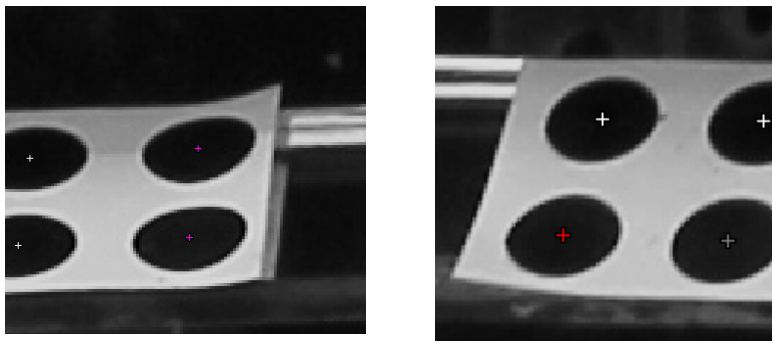

Figure 4.28 - Linear Fresnel target lift

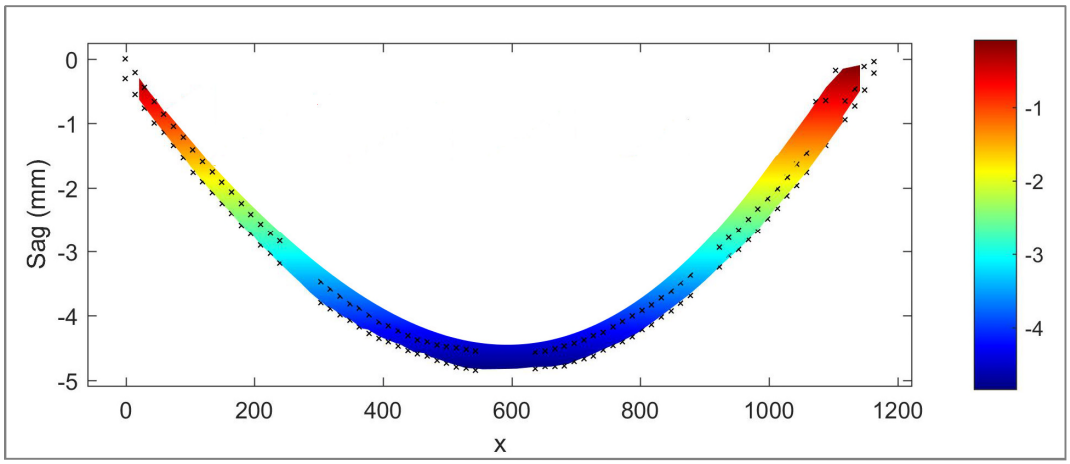

Figure 4.29 - Linear Fresnel sag measurement

This sag is approximately 5 mm for most mirror strips.

To investigate the difference between the section results, each strip had a curved polynomial fit performed on it. These are not plane surfaces due to the sag. The residual error from this curved surface for each point was then calculated to show those points that do not lie on the surface of the mirror. i.e. those that have lifted or are otherwise invalid. These were then plotted against the x,y coordinates to produce the the horizontal cross section shown in Figure 4.30.

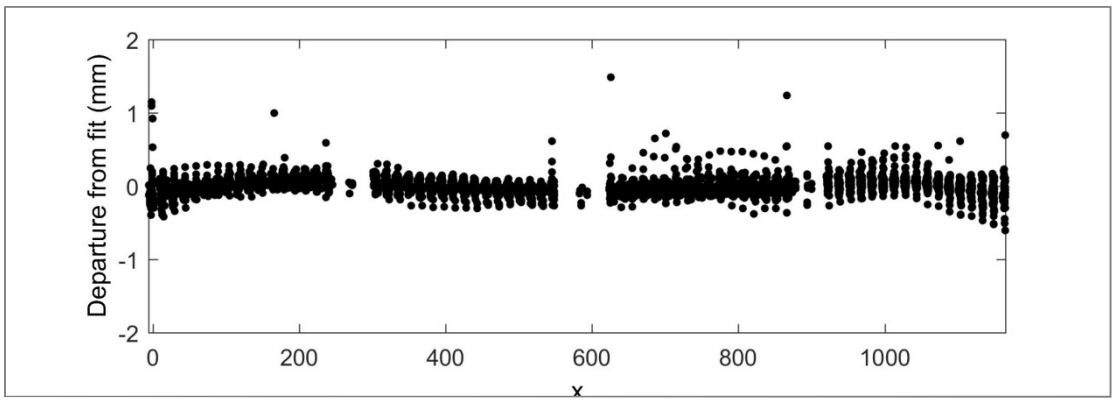

Figure 4.30 - Linear Fresnel target lifting

Each section may be seen from left to right. The second section has the best fit to the zero error line, with the third and fourth sections the worst. Some error points lie in curves on the third section indicating that perhaps a whole target strip may be invalid. This could be due to lifting or target shadowing as shown in Figure 4.31

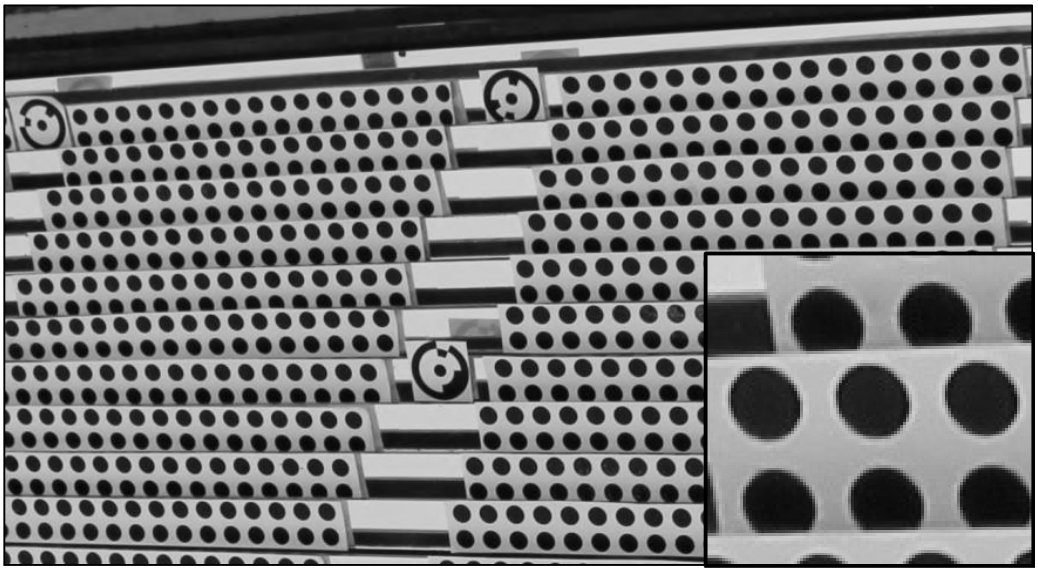

Figure 4.31 - Linear Fresnel target shadowing

The parabolic trough measurement done at King Abdulaziz University, Saudi Arabia can be seen in Figure 4.32 where a 900 x 700 mm grid of targets was placed on the mirror and further targets placed on the absorber tube in an attempt to locate both objects.

The photogrammetry scale was set using the distance between the points as found prior to the measurement. The grid was photographed from 8 positions with additional photographs taken of the tube and mirror together. The focal length of the mirror was unknown so this was calculated by a best fit algorithm for the general parabolic trough equation, along with the translation and rotation of the point cloud. The departure from the parabolic equation is shown in the resulting error map in Figure 4.33. This has a peak to valley error of 0.8 mm, with a single anomalous point of 1.2 mm removed. The trough was calculated to have a focal length of 640 mm. Overlaying this surface map onto the rear structure reveals little indication of the cause of the errors seen (Figure 4.34).

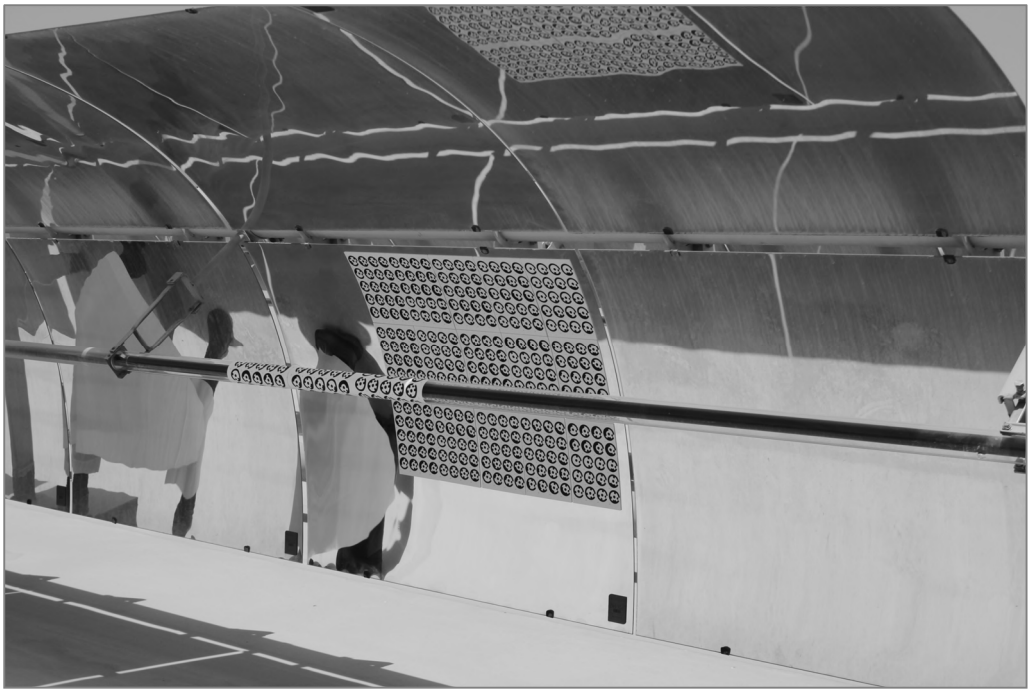

Figure 4.32 - Saudi Arabia parabolic trough set up

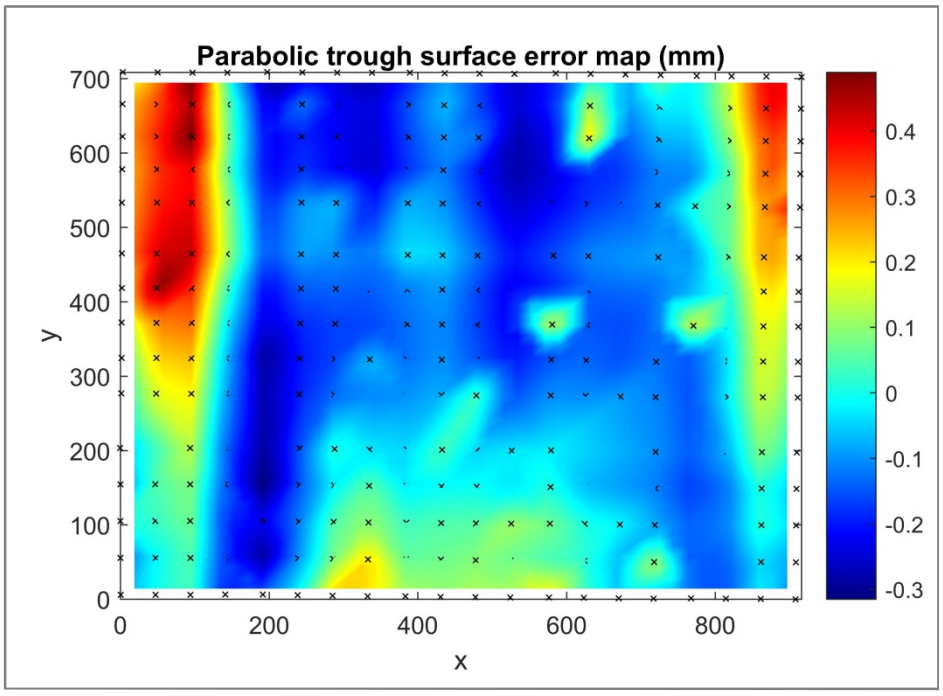

Figure 4.33 - Saudi Arabia parabolic trough surface error map

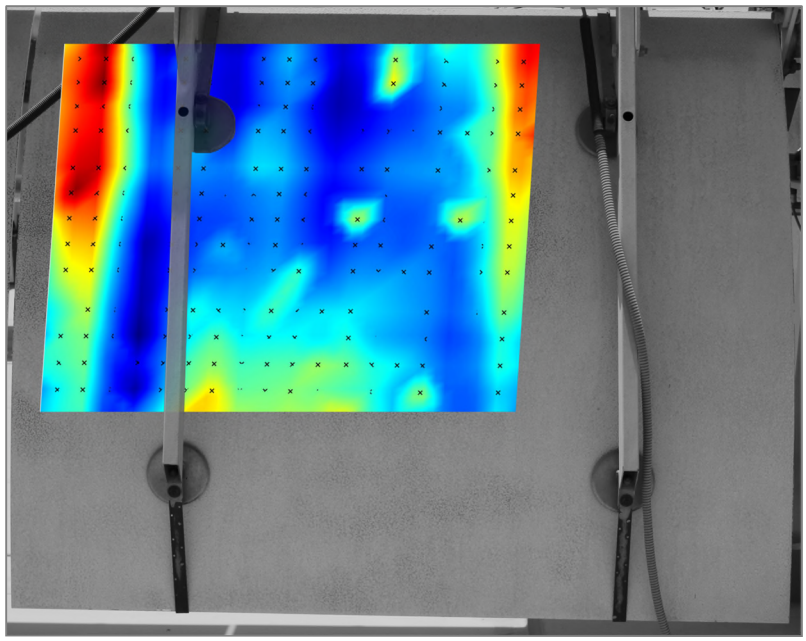

Figure 4.34 - Saudi Arabia parabolic trough rear structure

A ray trace done on the trough reveals that the majority of the rays would strike the absorber tube in its assumed position, with the few that miss highlighted in red on Figure 4.35.

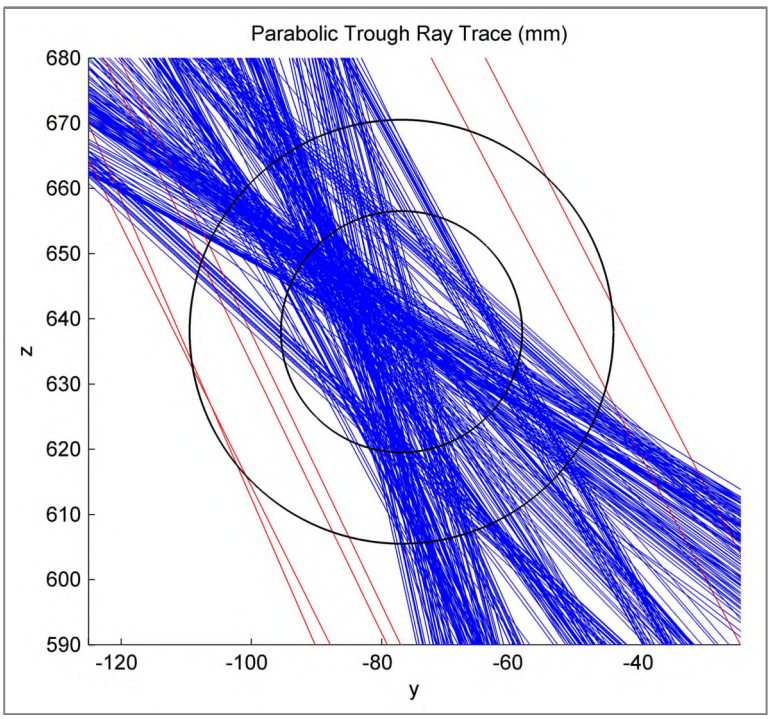

Figure 4.35 - Saudi Arabia parabolic trough ray trace

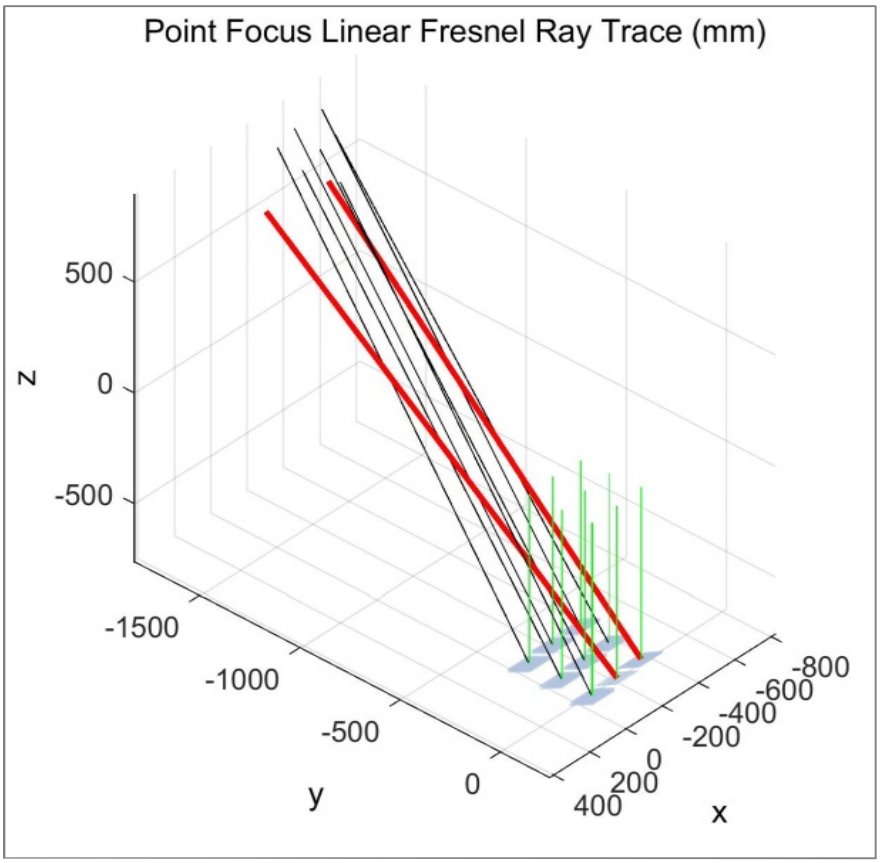

Figure 4.36 - Saudi Arabia point focus linear Fresnel ray trace

It was not possible to locate the absorber tube using photogrammetry as the targets were too distorted due to curvature of the tube. Additionally the photographs were primarily focused on the mirror so those on the tube were out of focus. Locating the tube in the manner is not straightforward especially when considering larger troughs, which would have larger focal lengths.

The point focus linear Fresnel collector system was measured for the orientation of each of the square mirrors, the resulting ray trace is shown in Figure 4.36, with the two misaligned mirrors shown in red and as a result of these measurements it was reported that the Saudi Arabia point focus linear Fresnel was redesigned.

4.1.6 Measurements on the MATS test line

This section details the measurements done on the thin glass Ronda mirrors at the MATS test line at ENEA, Italy.

The photographs for each mirror facet were loaded into PhotoModeler and the automatic target marking was carried out, mirror 1 is shown in Figure 4.37. Once all the targets were identified and the 3D point cloud generated the coordinate system was applied. This coordinate system made use of the targets placed at the corners of the mirrors to define the axes and the scale of the project. The scale was set at 1200 mm between corners along the non-curved edge of the mirror to minimise the error, the points used for mirror 1 are highlighted in green on Figure 4.38.

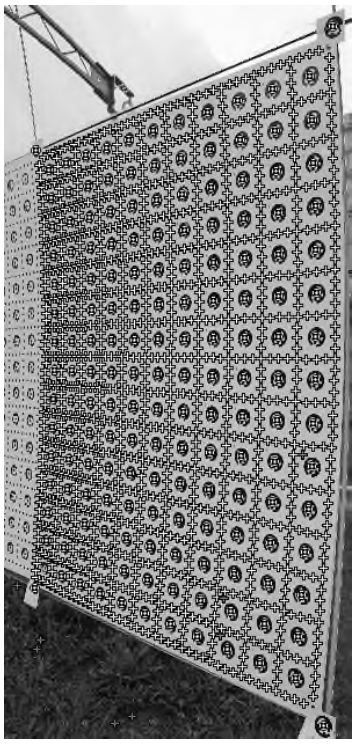

Figure 4.37 - Points marked

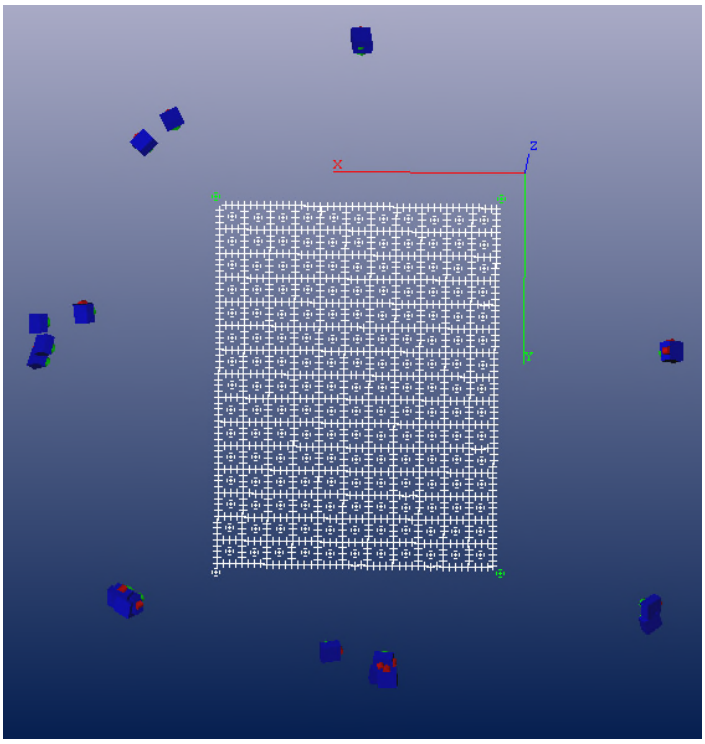

Figure 4.38 - Generated 3D point cloud with camera positions

The point cloud was then imported into MATLAB for further analysis. Using the computer-aided design drawings provided with the mirrors the angle through which to rotate the mirror and the translational values to be applied were calculated. Each point cloud was rotated by 32.19 degrees, and translated by

1602 mm in y and 354 mm in z. This placed the mirror in a position where it could be compared directly with the parabolic equation. The departure from the ideal parabolic equation can be seen in Figure 4.39 and shows a large distortion in the curved direction as well as several areas of isolated displacement of high magnitude caused by lifting of the target sheets near the corners. It was necessary to remove the influence of these lifted points before calculating the error present in the mirror. This was done by considering that such errors are localised to small areas of the mirror any real errors in the millimetre range would be due to long length distortions over the whole facet. A second order polynomial in x and y was fitted to the points shown in Figure 4.39, with the RMS residual from this fit calculated. Any points that were more than twice this RMS residual were marked as outliers and not used for the remaining calculations ensuring that 95% of the points are still kept. The points excluded can be seen highlighted in black on Figure 4.40. Though there is still some influence from the outliers, this has been greatly reduced.

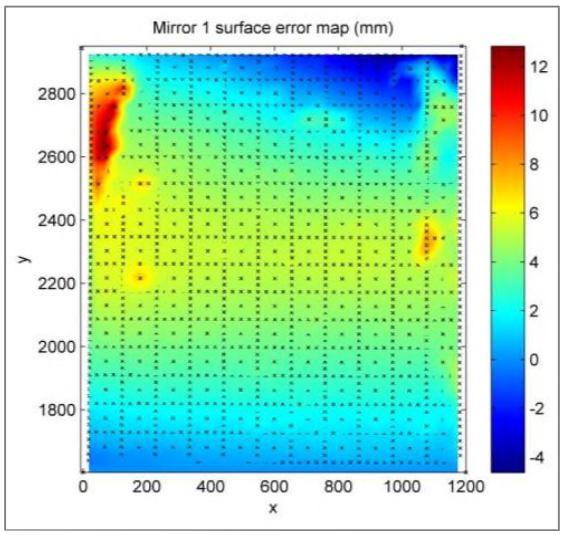

Figure 4.39 - Mirror 1 surface error map (mm)

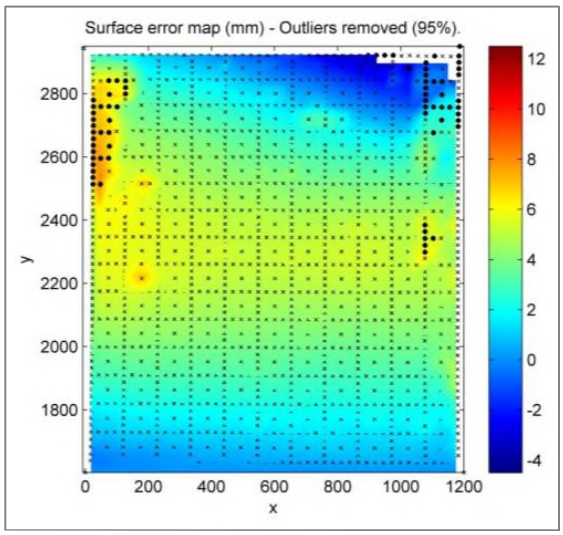

Figure 4.40 - Mirror 1 surface error map (mm) with outliers removed

With the largest outliers removed, a second polynomial was fitted to the remaining points to separate the form error, Figure 4.41, from the smaller variations as shown in Figure 4.42.

It is the form error from Figure 4.41 which may be used when adjusting the support points behind the mirror and correcting the shape. This form error shows that the middle left support point requires the most adjustment, approximately 6 to 7 mm followed by the middle right point at 4 to 5 mm. There would also be some balancing to be done with the corner support points due to the twist in the mirror. The form error has a peak to valley value of 9.5 mm and an RMS error of 3.9 mm. This is approximately a factor of 10 more than the values of 1.4 mm peak to valley and 0.4 mm RMS found for the mirrors within the lab. It is clear from these values that the mirror requires significant adjustment to restore it to its optimal shape. The flexibility of the mirrors is therefore an important factor to consider when comparing the performance of the thinner glass mirrors with that of the thick glass.

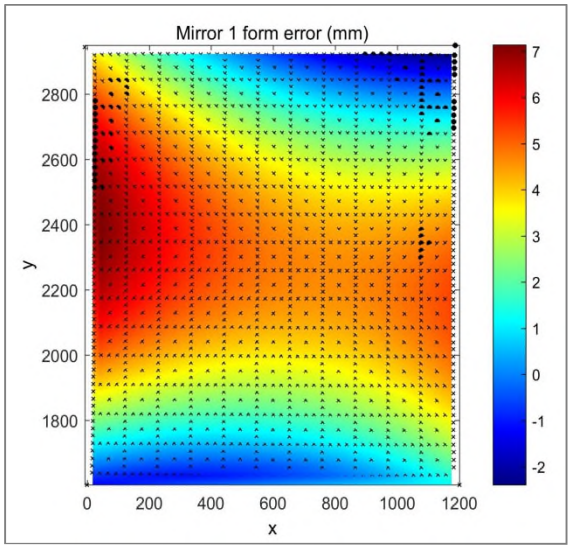

Figure 4.41 - Mirror 1 form error

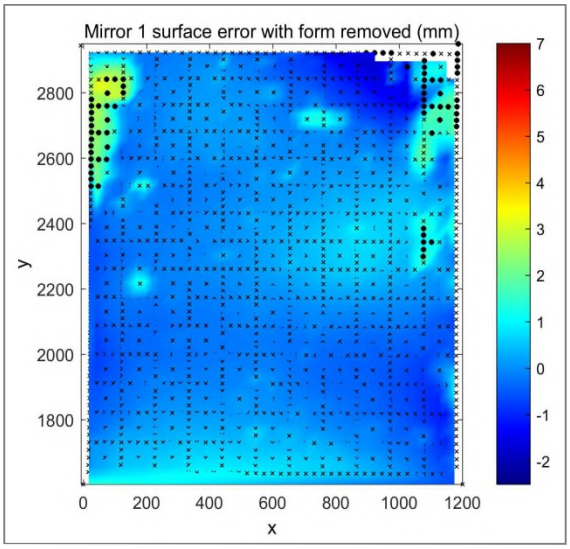

Figure 4.42 - Mirror 1 surface error with form removed

The analysis was repeated with the results from the second mirror as shown in Figure 4.43. In this case Figure 4.44 indicates that there is a large focal length error only, with minimal twisting of the mirror. From this the adjustments necessary should be symmetrical from left to right and may only require the middle supports to be changed. The form error has a peak to valley error of 12 mm and an RMS error of 7.5 mm.

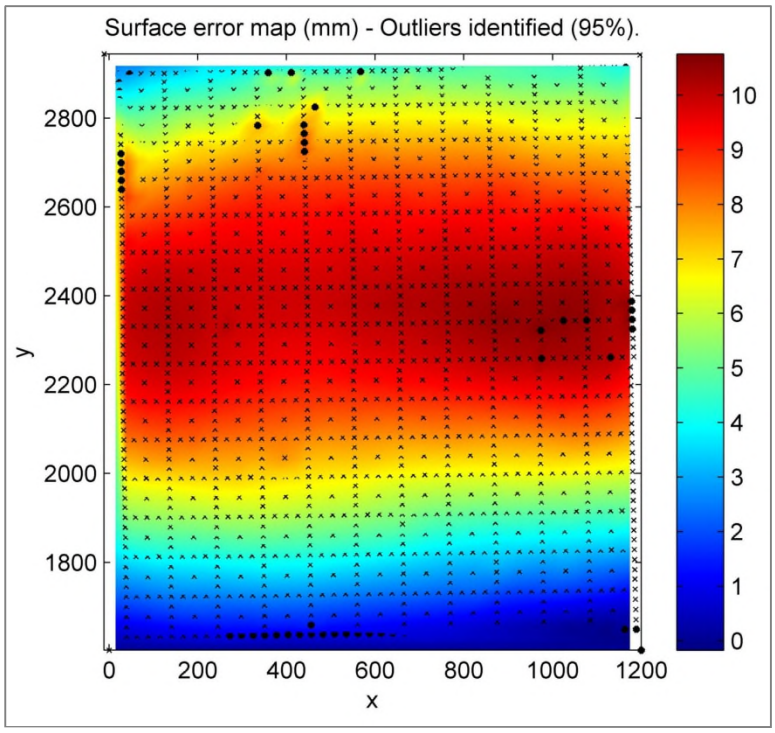

Figure 4.43 - Mirror 2 surface error map (mm) with outliers shown

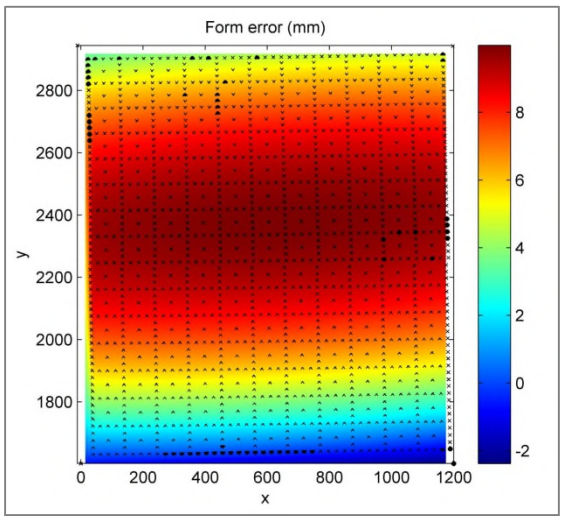

Figure 4.44 - Mirror 2 form error

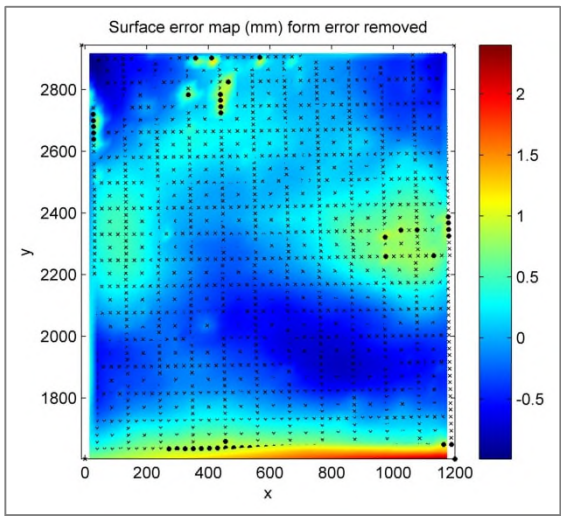

Figure 4.45 - Mirror 2 surface error with form removed

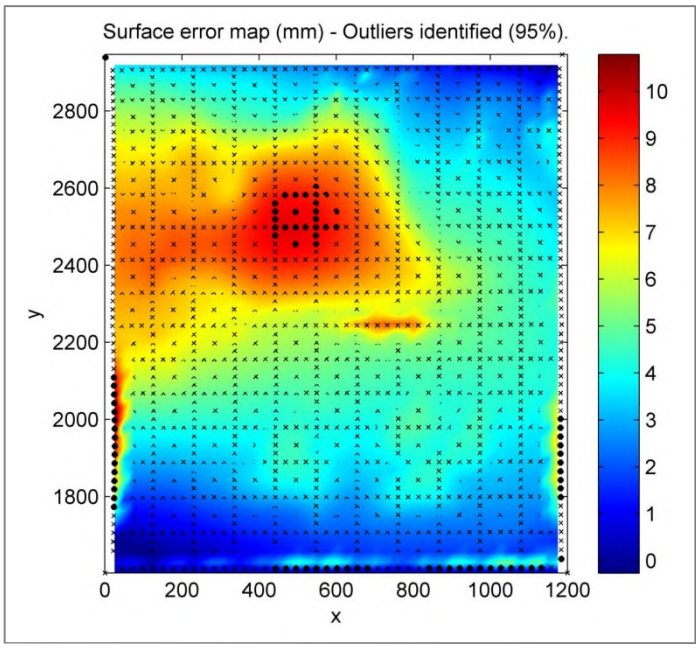

Figure 4.46 - Mirror 3 surface error map (mm) with outliers shown

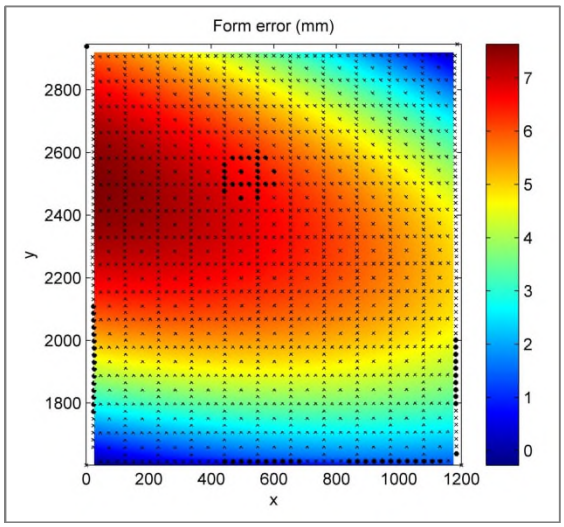

Figure 4.47 - Mirror 3 form error

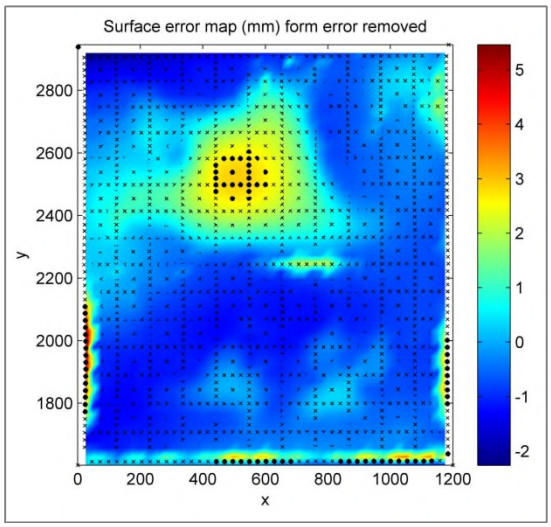

Figure 4.48 - Mirror 3 surface error with form removed

The third mirror shown in Figure 4.46 shows a predominantly focal error with the addition of the top left corner requiring significant adjustment by 7 to 8 mm to balance with the other three. The peak to valley form error is 7.7 mm with an RMS value of 5.4 mm.

Unlike the results from the laboratory measurements there is no clear influence from the supporting ribbed structure that can be seen. During the laboratory

measurements the influence of this structure was measured at less than 1mm, which is small in comparison to the 5 to 10 mm of error seen in the site measurements.

The points across all three mirrors were combined into a single solution within PhotoModeler. This shows how the mirrors are aligned relative to one another and considers the trough as a continuous mirror surface. As was done previously the outliers were identified and the overall second order polynomial form separated.

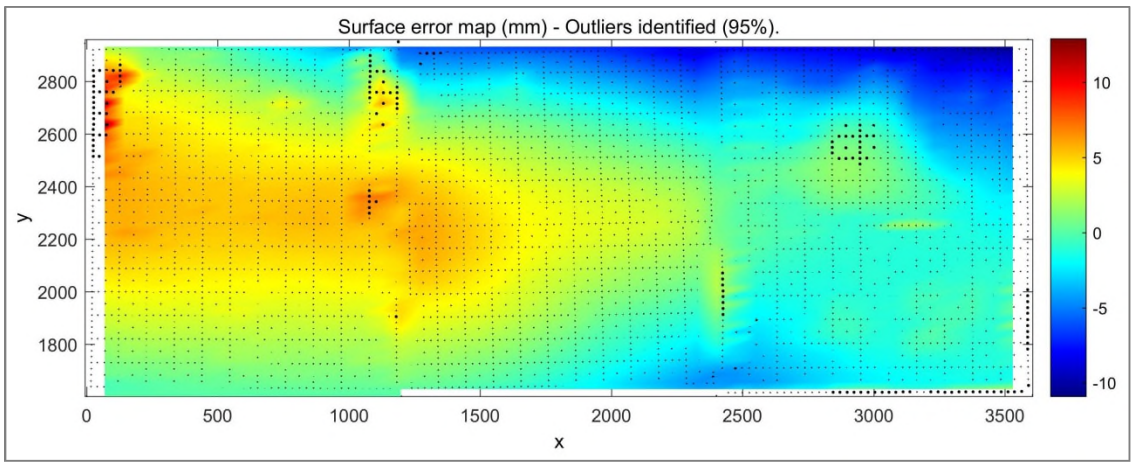

Figure 4.49 - Combined surface error map (mm)

The combined surface error map in Figure 4.49 shows the same distortions and excluded points as for the individual facets, but includes also the longest length distortion which crosses the mirror boundaries as can be clearly seen in Figure 4.50.

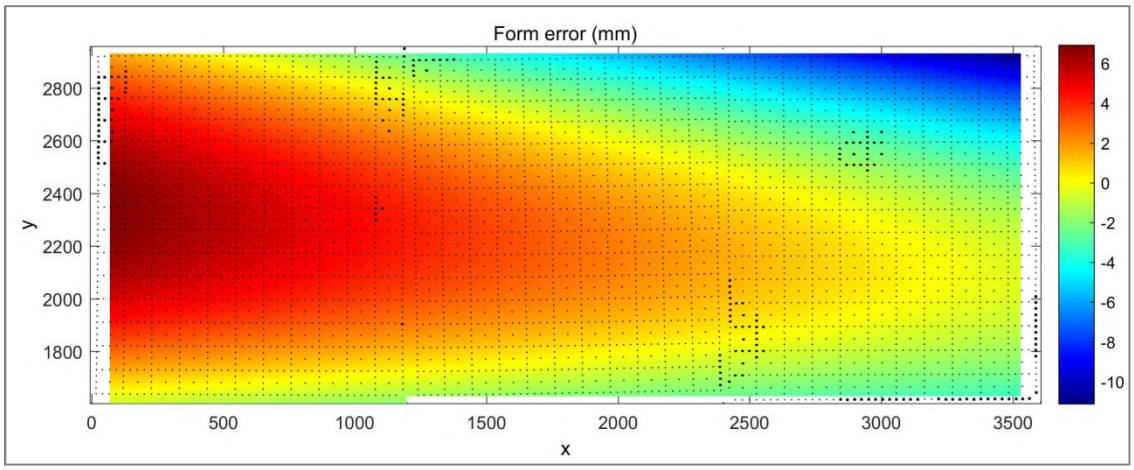

Figure 4.50 - Combined form error map (mm)

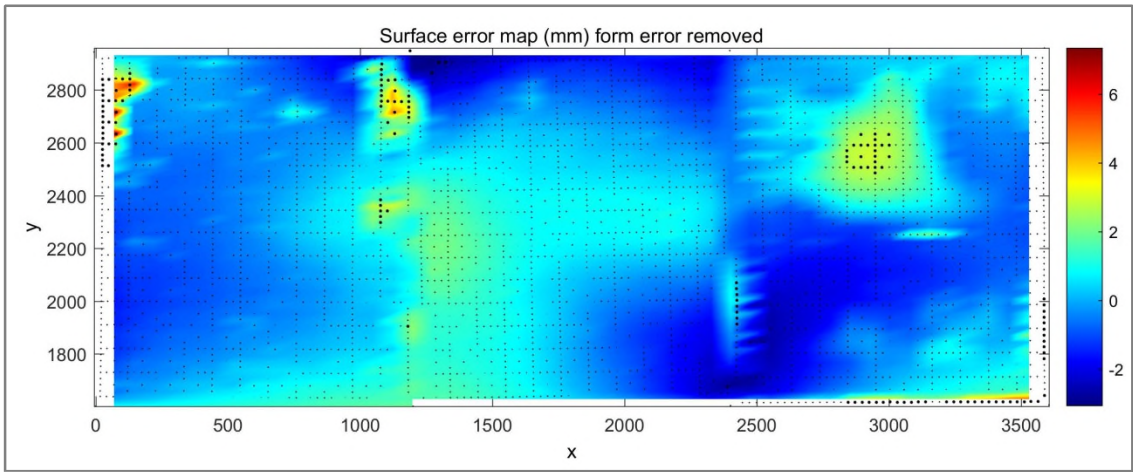

Figure 4.51 - Combined surface error map with form removed

Due to its smooth and continuous shape it is expected that the form error is correctable by using the adjustment screws located at each support point, shown in Figure 4.52.

Figure 4.52 - Ronda mirror support adjustment

The point cloud for each mirror was interpolated to a regular grid with a 35 mm point spacing, similar to the original spacing. The slope between adjacent points in the curved direction was then calculated and compared with that expected from the parabolic equation. This difference is the slope error and is used to trace the light as it is reflected towards the absorber tube.

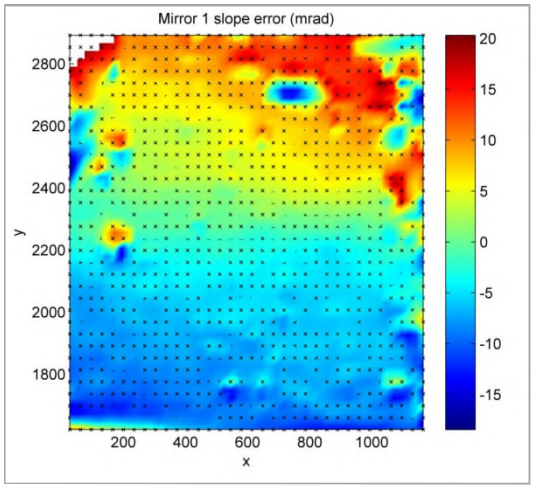

Figure 4.53 - Mirror 1 slope error

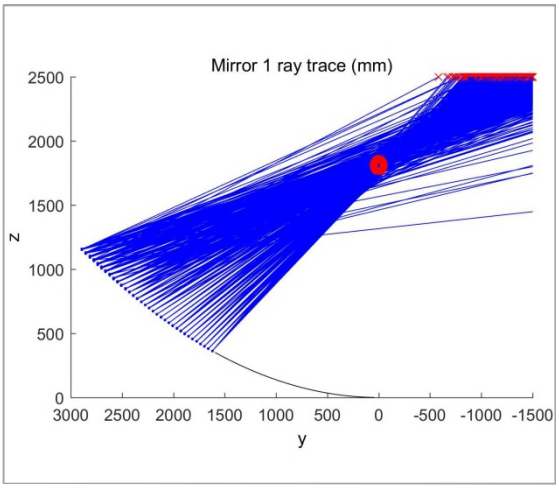

Figure 4.54 - Mirror 1 ray trace

Figure 4.53 shows the calculated slope error map for the first mirror. There are many points that have a large departure from their local neighbours and these points produce the extreme rays seen in Figure 4.54. Such points are caused by the bubbles in the photogrammetry sheet and can be discounted when considering the performance. The focal point of the mirror is beyond the position of the absorber tube at position (0,1810) and indicates that the mirror is not sufficiently curved to focus the light correctly. This can be seen in Figure 4.55 where there is a clear focal point at approximately y = -200 mm. The extent of the rays which are far from the absorber tube can also be seen, for a properly adjusted mirror all these rays should be striking the absorber tube and be focussed at its centre. The RMS slope error for mirror 1 is 11.1 mrad, which is much greater than the target slope error of 2 to 3 mrad. However, the RMS slope found for the laboratory adjusted mirror was 2.7 mrad, which indicates that the target may be achievable with adjustments.

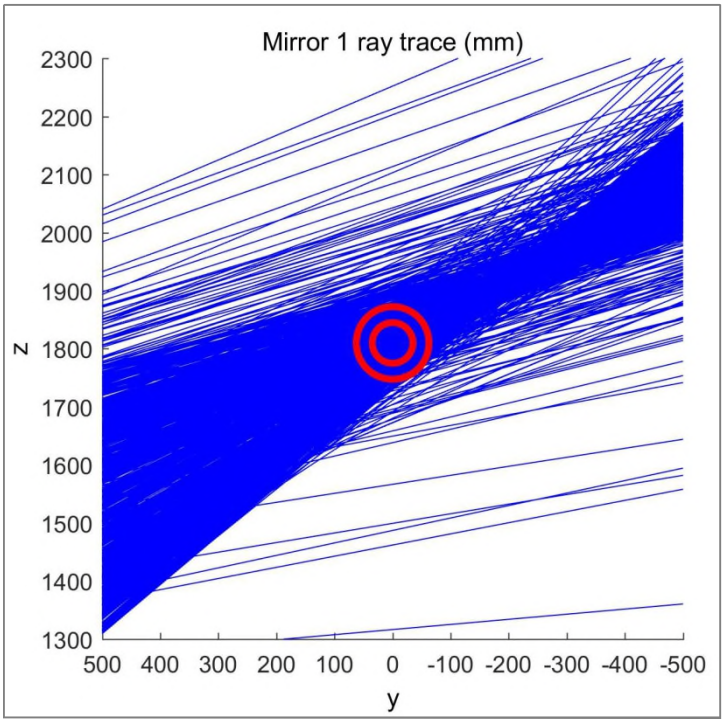

Figure 4.55 - Mirror 1 ray trace close up

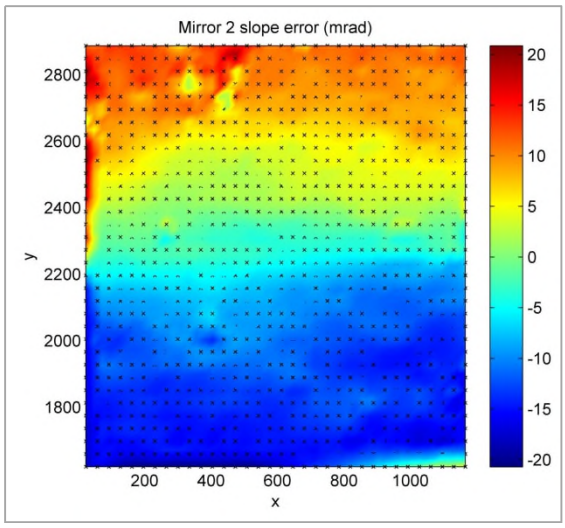

Figure 4.56 - Mirror 2 slope error

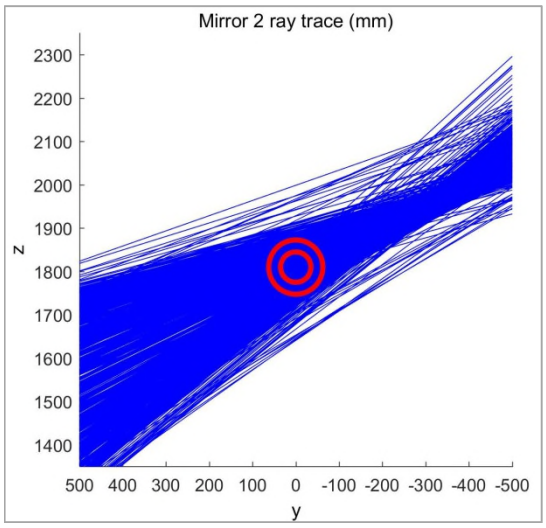

Figure 4.57 - Mirror 2 ray trace

Figure 4.56 shows mirror 2 slope error with fewer extreme points and this is reflected in the ray trace shown in Figure 4.57. The focal point for mirror 2 is 300 mm away from the centre of the absorber tube in the y direction, which is further than for mirror 1. However there are fewer rays which miss the absorber tube and a tighter focus. The RMS slope error for mirror 2 is 10.7 mrad, similar to mirror 1.

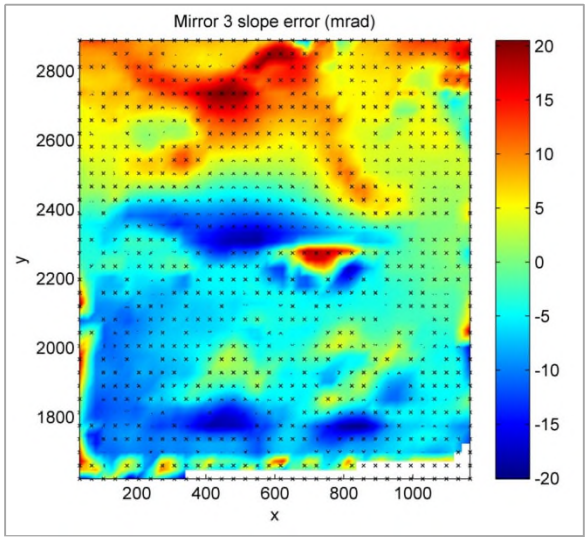

Figure 4.58 - Mirror 3 slope error

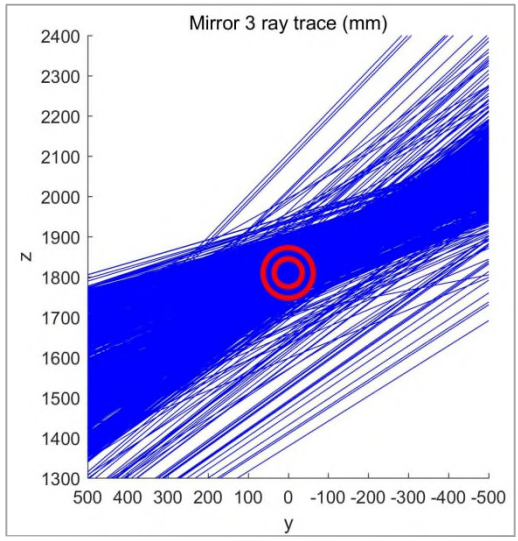

Figure 4.59 - Mirror 3 ray trace

The slope error map for mirror 3 in Figure 4.58 shows large areas of extreme error points as well as numerous individual extreme points, such as those towards the bottom of the map. These points are reflected in the ray trace as

rays that are far from the absorber tube. The focus for mirror 3 is wider than that of mirror 2 and is located approximately 200 to 300 mm from the centre of the absorber tube in the y direction. The RMS slope error for mirror 3 is 12.5 mrad, the greatest of the three mirrors.

From these ray traces it was possible to calculate an intercept factor for each mirror facet. The intercept factor is given by the percentage of incident radiation which successfully strikes the absorber tube. The points in the slope maps are equally distributed and so can be used in calculating the intercept factor. For each point in the slope map there is a corresponding light ray which has been traced toward the absorber tube. The minimum distance that this ray passes the centre of the absorber tube was calculated and those rays which pass within the absorber radius of 35 mm are successful rays. The ratio of successful rays against total rays is then the intercept factor. By using the distance of closest approach of the rays it is also possible to calculate the defocus of the mirror, as shown in Table 4.5.

	Intercept factor (%)	**RMS Defocus (mm)**
Mirror 1	58.3	60.7
Mirror 2	31.8	52.9
Mirror 3	54.9	59.2

Table 4.5 - ENEA intercept factors and defocus

Such intercept factors are significantly below that expected from a fully installed and adjusted collector. It is expected that the intercept factor should be in excess of 90% with minimal defocus. However it is not surprising that the intercept factors measured are so low due to the incomplete installation of the measured collector.

4.1.7 Measurements at CIEMAT-PSA

The following section details the measurements done on a EuroTrough collector at CIEMAT-PSA in Spain. The measurements included both the whole trough and individual facets in three positions to replicates their tracking movements.

The photographs for the whole facet measurements were loaded into PhotoModeler and processed to produce the 3D point cloud as shown in Figure 4.60 and Figure 4.61. The coded targets were automatically identified and points on the four corners of the trough were manually marked to be used in defining the coordinate system.

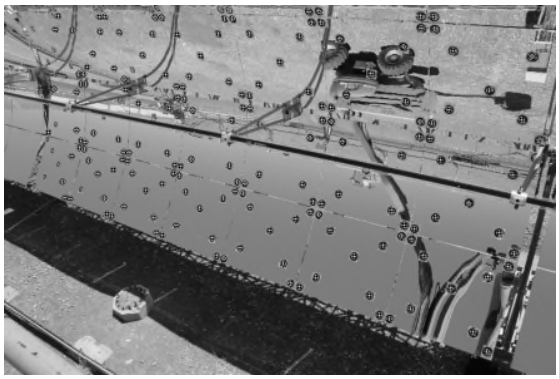

Figure 4.60 - Points marked

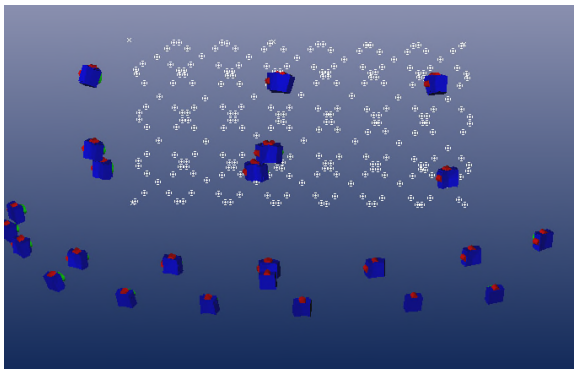

Figure 4.61 - 3D point cloud

The point cloud was loaded into MATLAB and the parabolic equation for the EuroTrough with a focal length of 1.71 m was used to find the surface error map, shown in Figure 4.62, this was repeated for the second and third positions. The rectangles shown on the whole trough surface maps represent the individual facets. The coordinate system for these measurements is such that the x-axis points along the trough axis from left to right and the y-axis is in the curved direction. The origin of the coordinate system is at the vertex of the parabola on the left edge such that the trough extends in the positive and negative y directions. The z axis therefore points parallel to the incoming radiation.

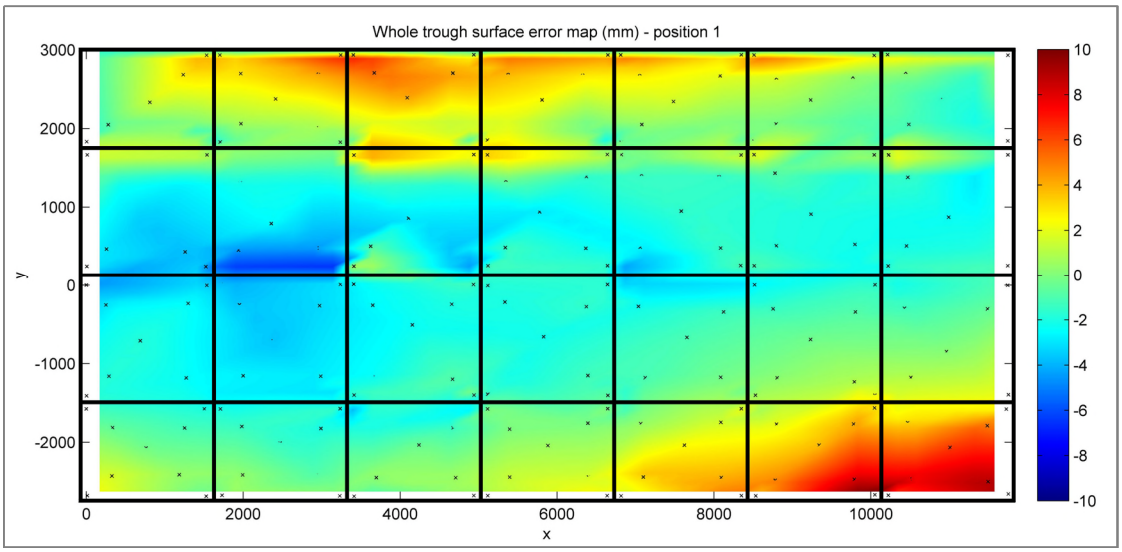

Figure 4.62 - Whole trough surface error map for position 1

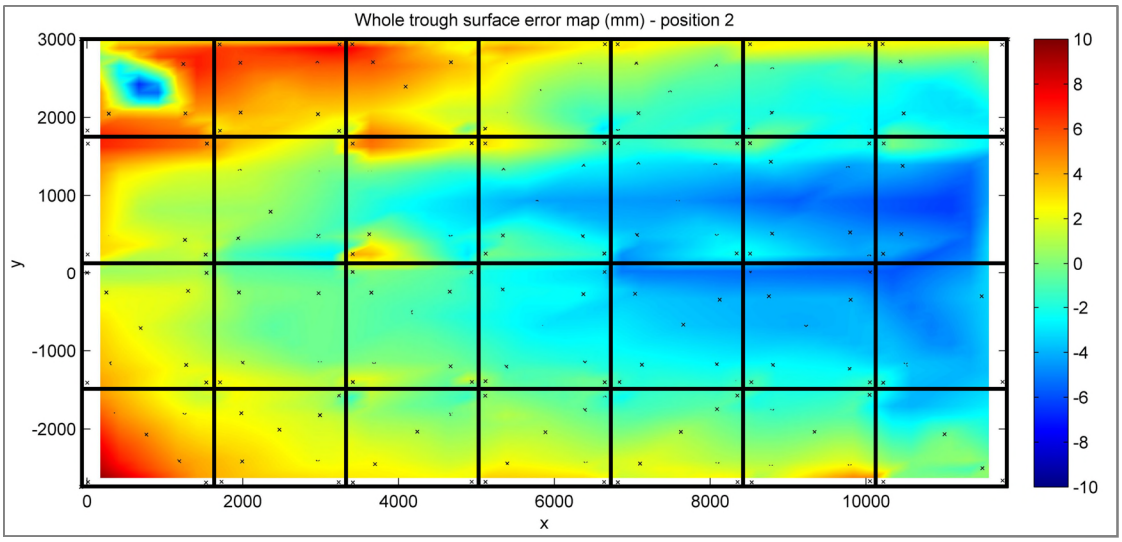

Figure 4.63 - Whole trough surface error map for position 2

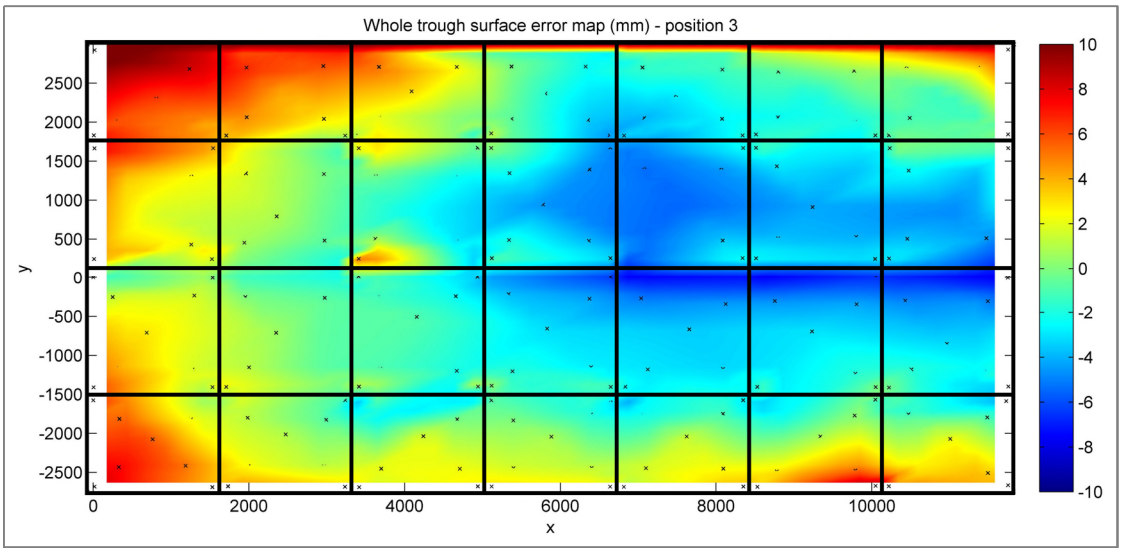

Figure 4.64 - Whole trough surface error map for position 3

The RMS departures from the ideal parabolic shape measured were 2.84 mm, 3.16 mm and 3.72 mm respectively. The overall form error was then removed by fitting with a second order polynomial, the results of which are shown in the following figures.

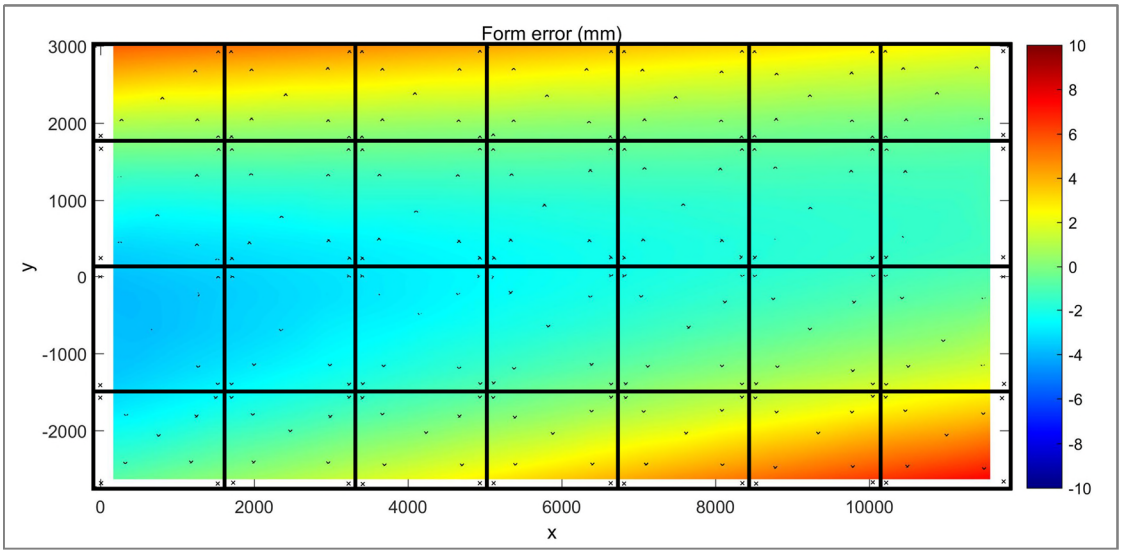

Figure 4.65 - Form surface error map for position 1

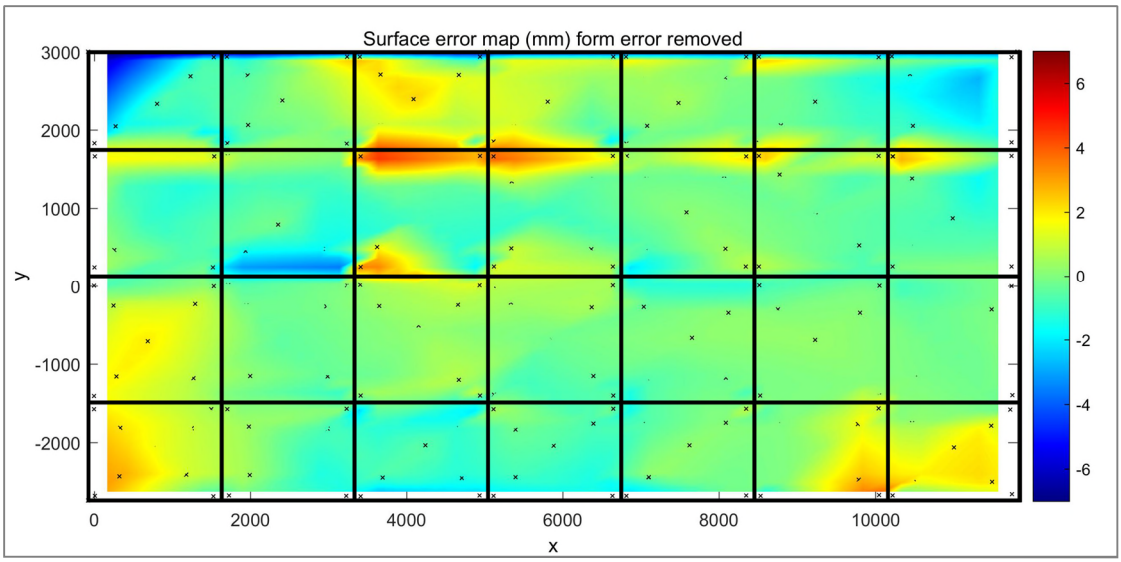

Figure 4.66 - Surface error with form removed for position 1

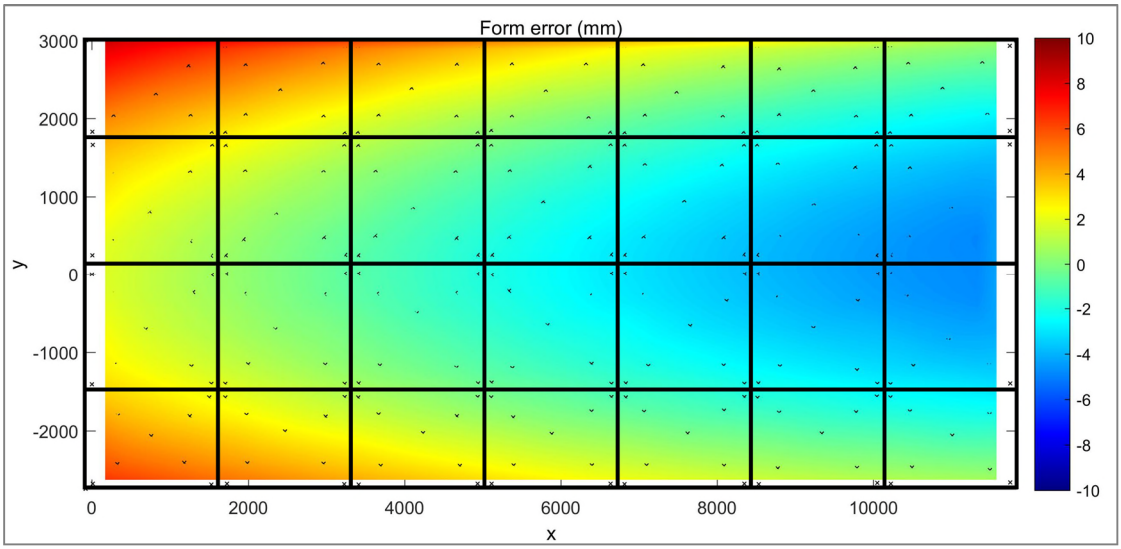

Figure 4.67 - Form surface error map for position 2

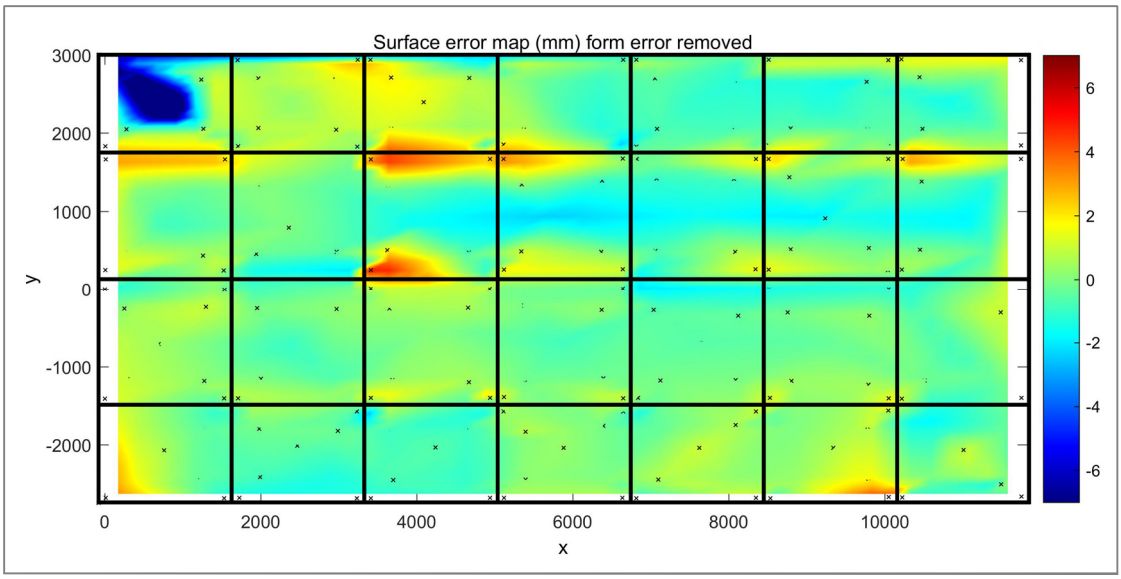

Figure 4.68 - Surface error with form removed for position 2

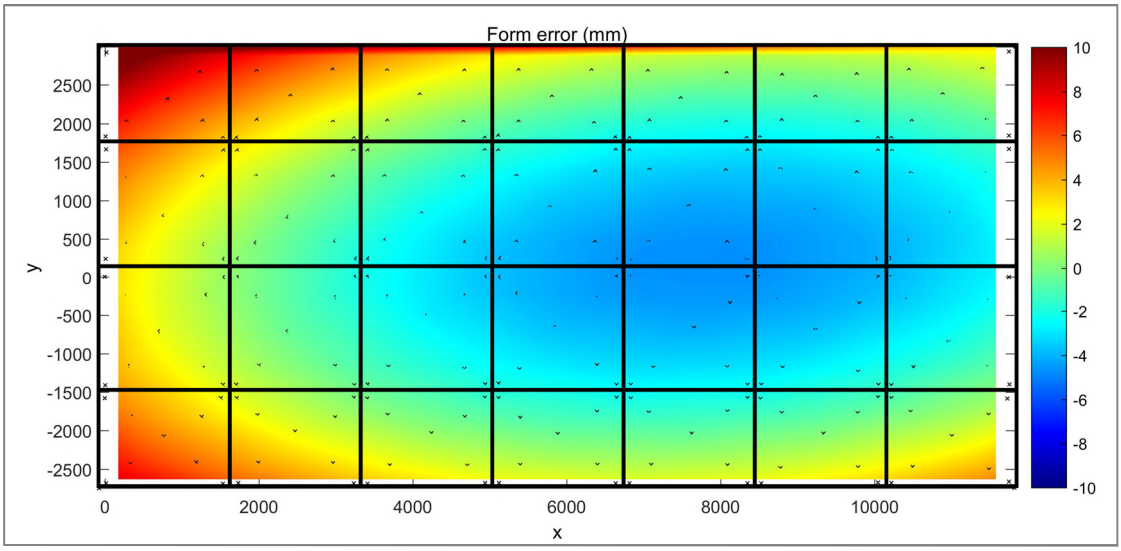

Figure 4.69 - Form surface error map for position 3

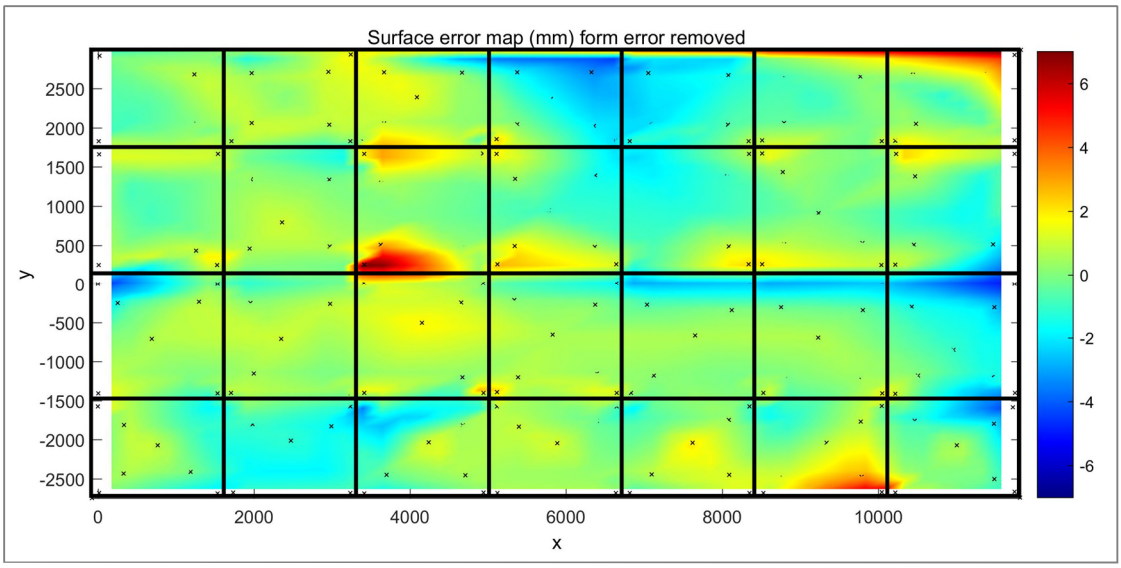

Figure 4.70 - Surface error with form removed for position 3

With the form error removed some boundaries are seen between the mirrors, where adjacent facets are not completely aligned. The form-removed error maps for the three positions are very similar with RMS errors of 1.52 mm, 1.63 mm and 1.77 mm respectively. This indicates that movement of the mirrors that occurs as the trough is rotated does not significantly affect the relative alignment of the facets with respect to one another but creates a distortion that covers the whole trough.

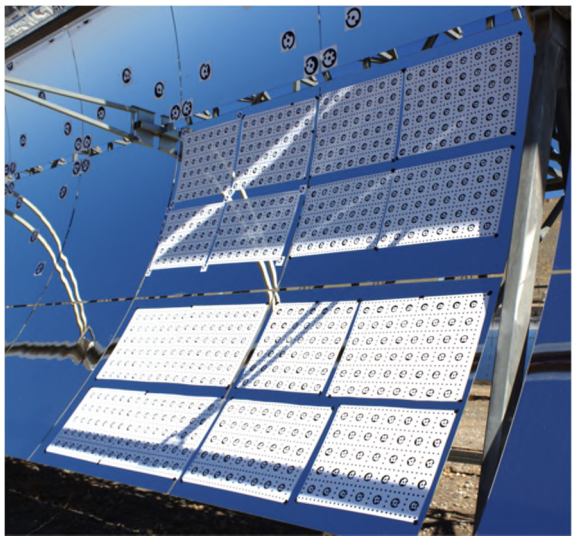

Figure 4.71 - Target sheet placement

Each of the four individual facets were photographed as separate mirrors with some additional overlapping images and solved separately using PhotoModeler. By separating the mirrors the size is close to the mirrors measured in the laboratory and so the accuracy is maintained. The corners of each mirror were identified manually within PhotoModeler and used to define the scale and coordinate system with the known dimensions. These points were subsequently removed from the fitting and surface mapping. The EuroTrough mirrors have different dimensions for the inner, 1640 x 1700 mm, and outer, 1500 x 1700 mm mirrors. The target sheets previously used for measuring the Ronda mirrors measure 1200 x 1600 mm and so were cut into quarters and placed so as to cover the support points shown in Figure 4.73 as well as possible.

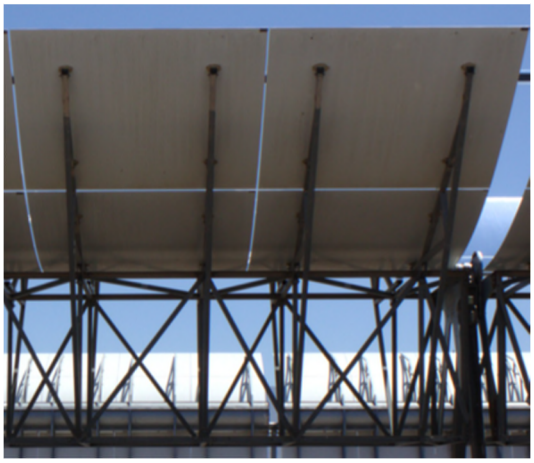

Figure 4.72 - EuroTrough supports

Figure 4.73 - Supports positions

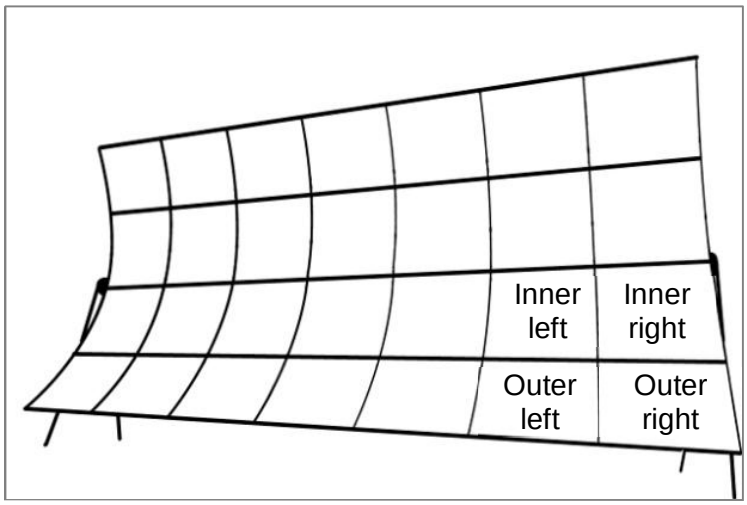

Figure 4.74 - PSA parabolic trough schematic

Figure 4.74 shows a schematic of the PSA trough in position 1, with the bottom rightmost corner four facets used for the measurements. The measurement positions were the same as those used for the whole trough.

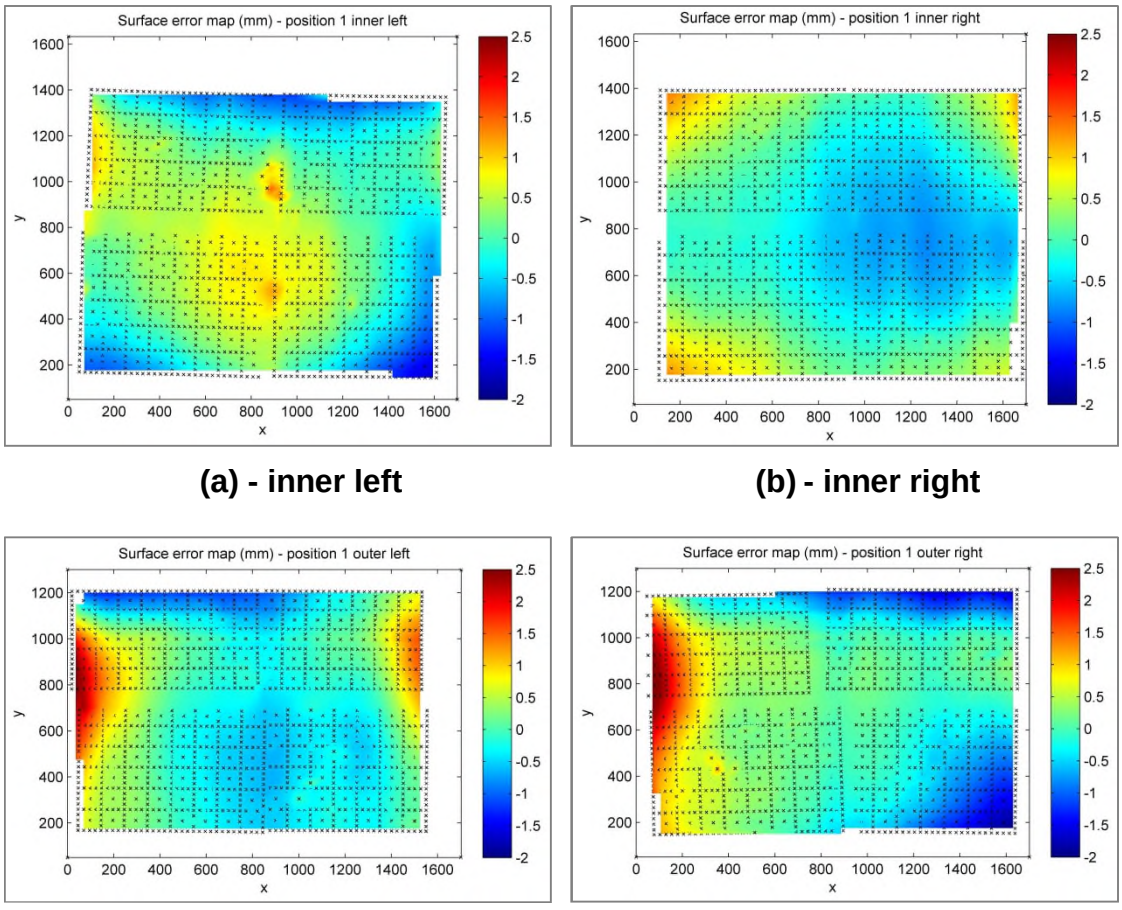

(a) - inner left **(b) - inner right**

(c) - outer left **(d) - outer right**

Figure 4.75 - Surface error maps position 1

The RMS errors are 0.60, 0.48, 0.67 and 0.79 mm respectively, which is significantly less than the values found for the thin glass Ronda mirror; however the Ronda mirror had not been fully installed and adjusted. These values are comparable to the 0.4 mm RMS error value for the Ronda mirror in the lab indicating that it may be possible for the thin glass mirror to achieve these values when fully installed.

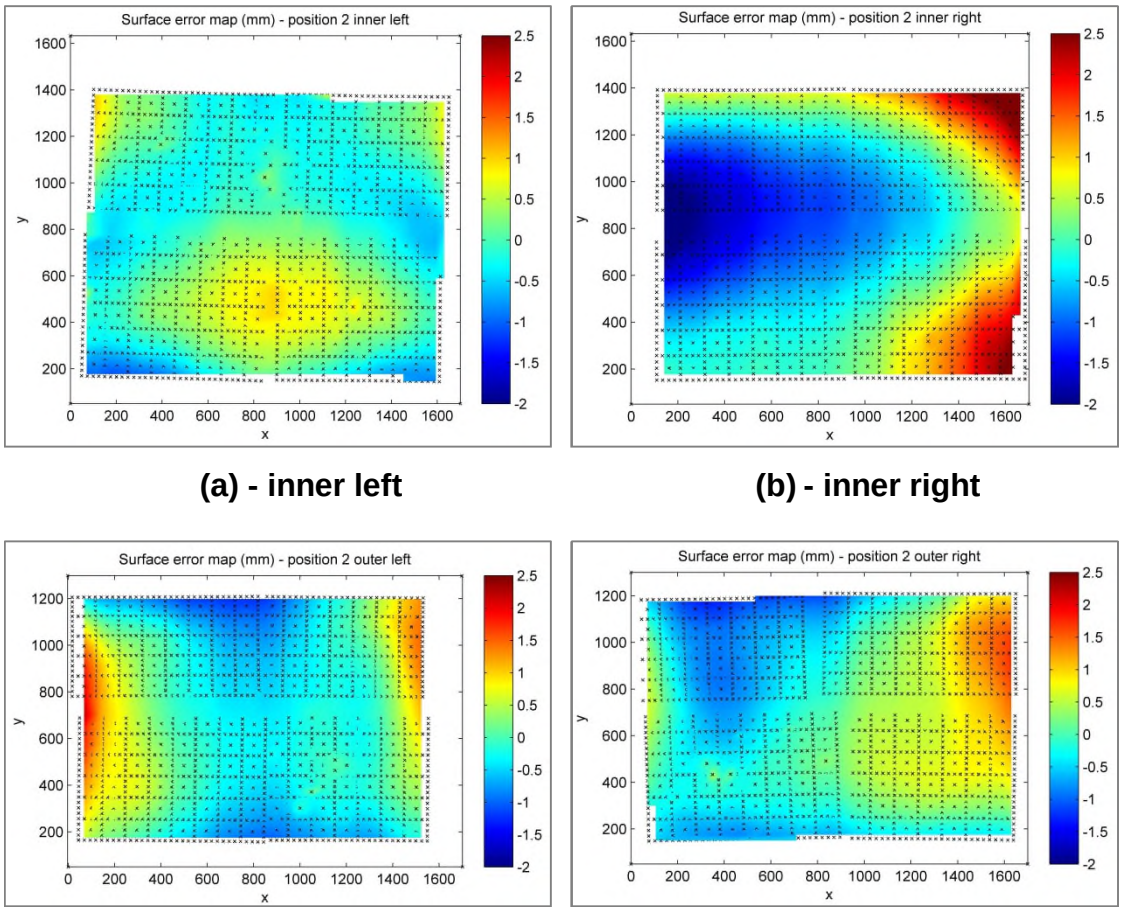

(a) - inner left **(b) - inner right**

(c) - outer left **(d) - outer right**

Figure 4.76 - Surface error maps position 2

The trough was rotated to point skywards and further measurements were made on the four sections. The RMS errors are 0.45, 1.12, 0.68 and 0.67 mm respectively and there appears to be little movement from position 1 with the exception of the inner right position, Figure 4.76b. The errors of the other three mirror facets are slightly reduced in this position, which is desirable as the majority of the energy will be captured while the trough is pointing toward the sky. The trough was further rotated to point horizontally in the opposite direction to position 1 and re-measured. The RMS errors are 0.79, 0.41, 0.86 and 0.87 mm respectively with no significantly high errors. The inner right mirror, Figure 4.77b, has returned to a low error state, with the other three mirrors remaining at similar levels as before, slightly down on position 2.

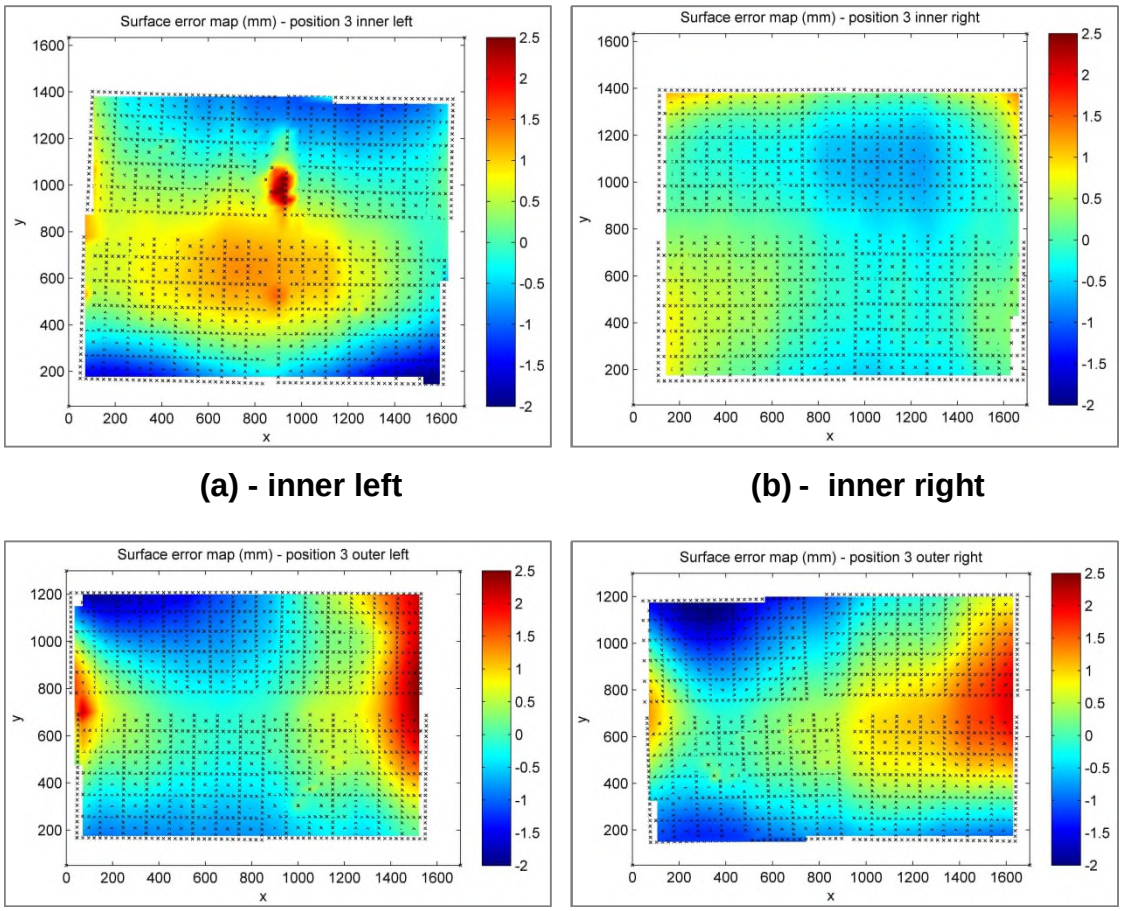

(a) - inner left **(b) - inner right**

(c) - outer left **(d) - outer right**

Figure 4.77 - Surface error maps position 3

The surface form error maps were interpolated to a regular grid and the slopes were calculated at each point. These slopes were then compared to the slope expected for an ideal mirror and the difference was plotted in Figure 4.78, Figure 4.79 and Figure 4.80. Due to interpolating over the large gap between sections of target sheets the slope error map has a horizontal stripe across it, which may be ignored in any calculations. The measured slope was then used to calculate the ray traces, which are also shown, and the RMS defocus and intercept factors for each facet, which are shown in Table 4.6.

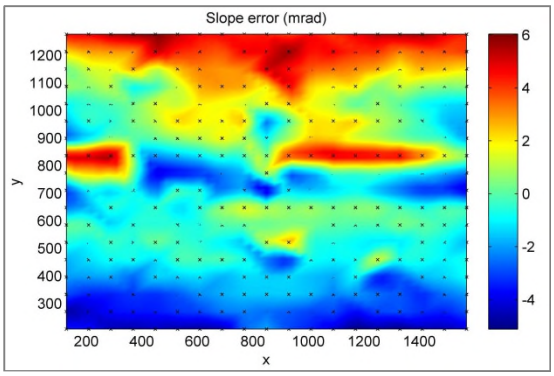

(a) - inner left

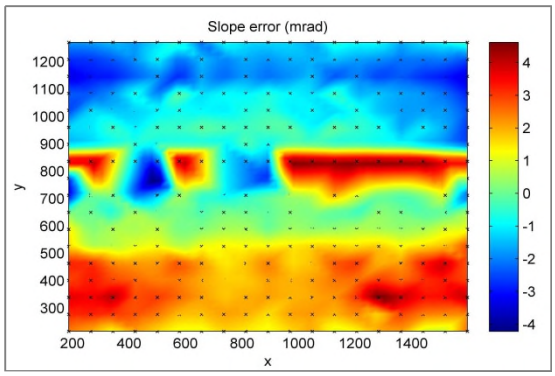

(b) - inner right

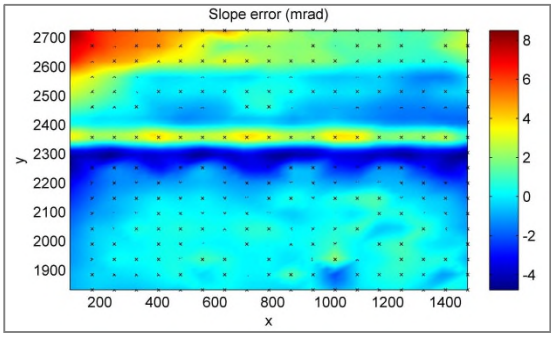

(c) - outer left

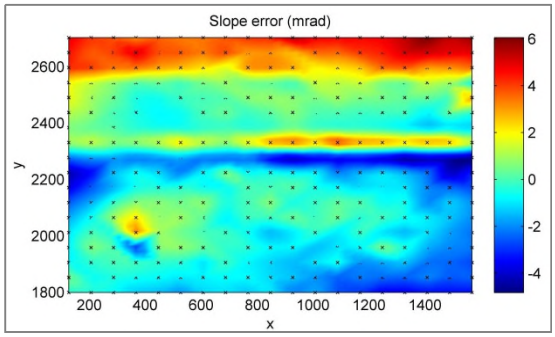

(d) - outer right

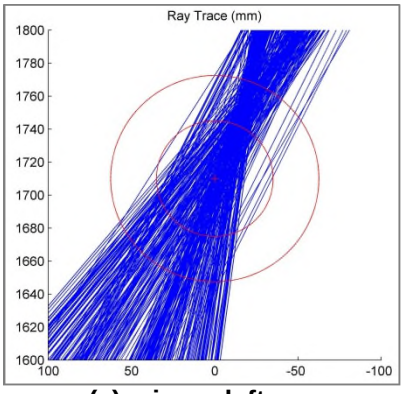

(e) - inner left

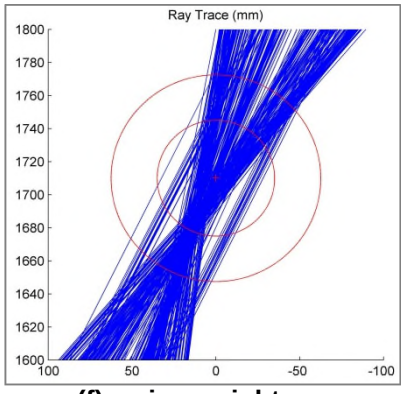

(f) - inner right

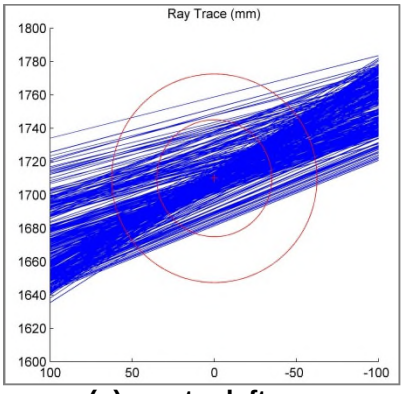

(g) - outer left

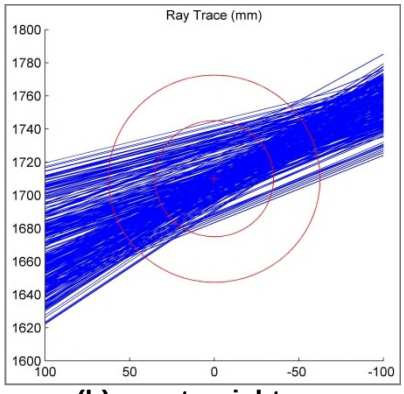

(h) - outer right

Figure 4.78 - Slope error maps and rays traces position 1

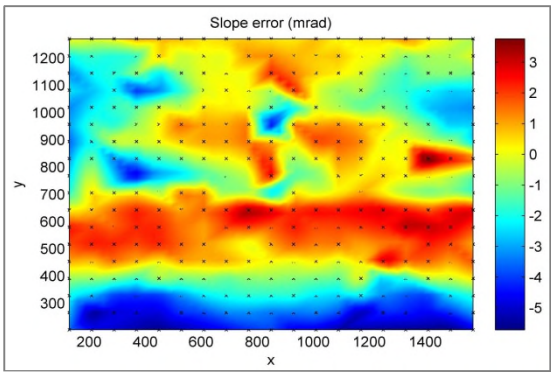

(a) - inner left

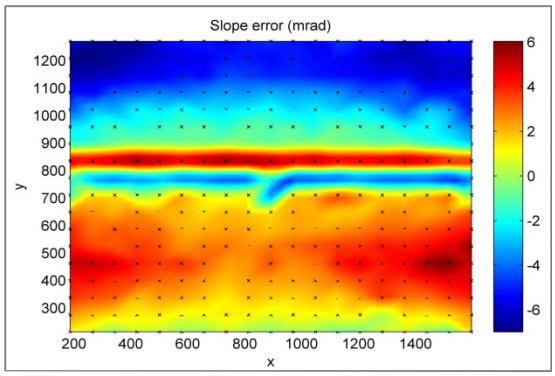

(b) - inner right

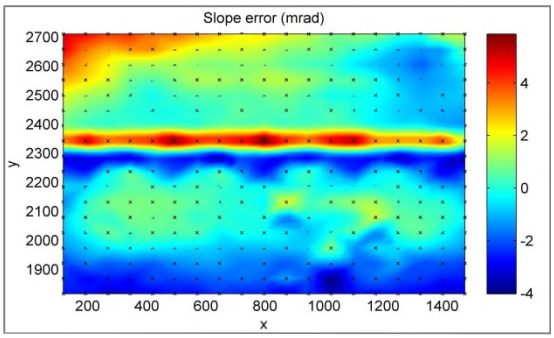

(c) - outer left

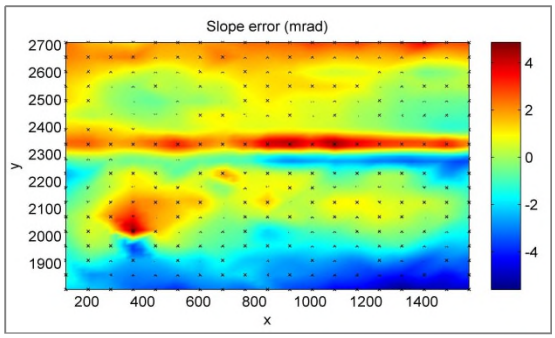

(d) - outer right

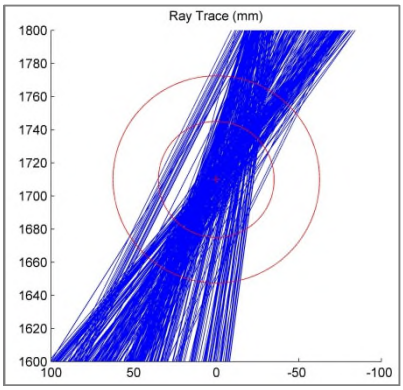

(e) - inner left

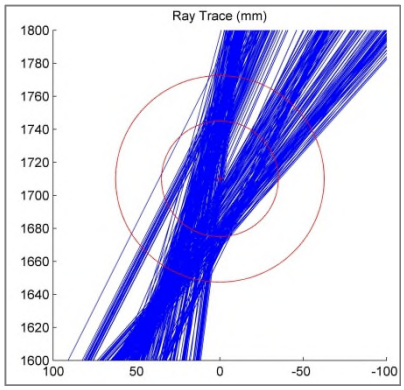

(f) - inner right

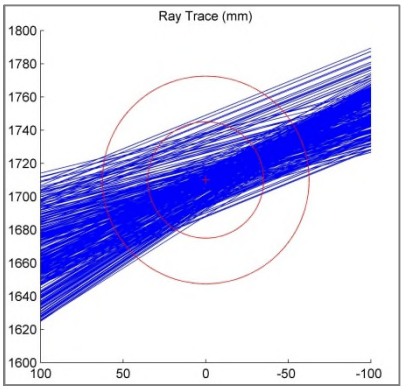

(g) - outer left

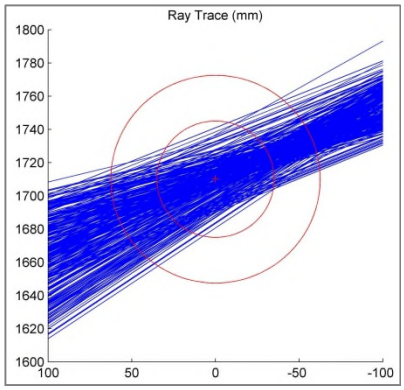

(h) - outer right

Figure 4.79 - Slope error maps and rays traces position 2

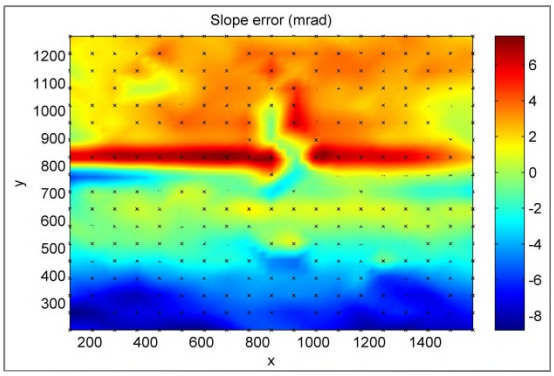

(a) - inner left

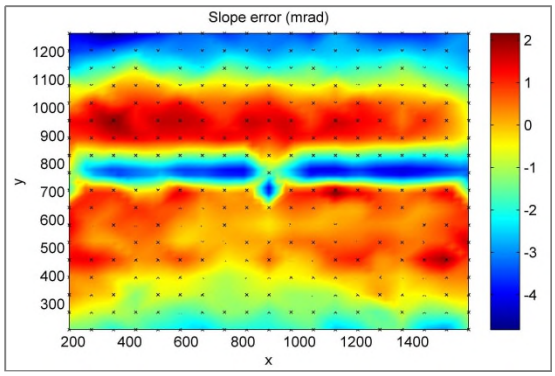

(b) - inner right

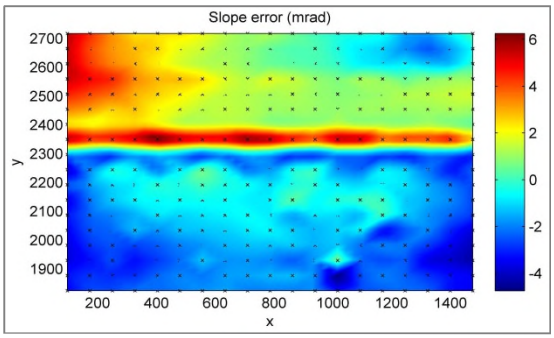

(c) - outer left

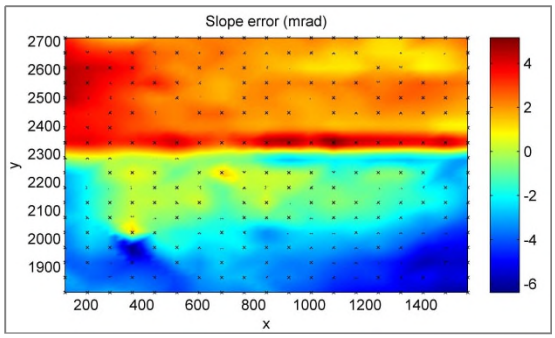

(d) - outer right

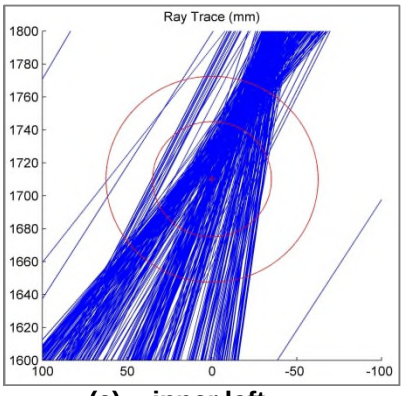

(e) - inner left

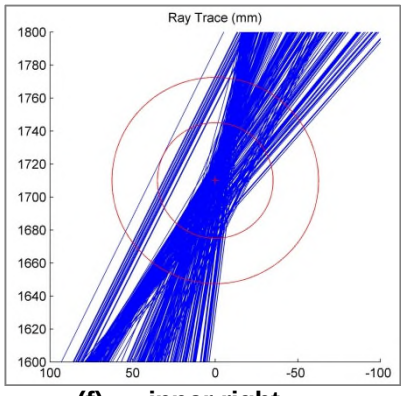

(f) - inner right

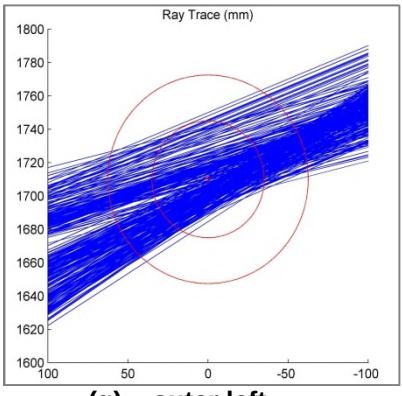

(g) - outer left

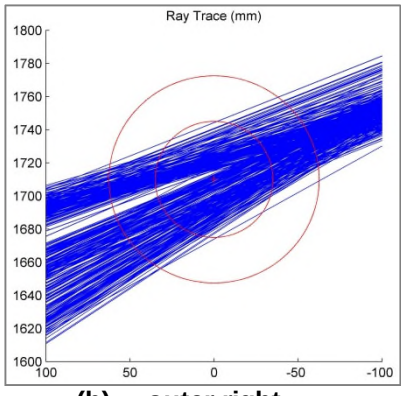

(h) - outer right

Figure 4.80 - Slope error maps and rays traces position 3

Mirror facet	RMS slope error (mrad)	RMS defocus (mm)	Intercept factor (%)
Position 1, inner left	3.06	11.2	100
Position 1, inner right	2.55	9.14	100
Position 1, outer left	2.27	11.8	98.5
Position 1, outer right	2.27	11.75	100
Position 2, inner left	2.89	10.29	100
Position 2, inner right	3.80	13.95	100
Position 2, outer left	2.06	10.21	99.7
Position 2, outer right	2.03	9.67	100
Position 3, inner left	4.65	16.68	98.8
Position 3, inner right	2.44	8.96	99.7
Position 3, outer left	2.49	12.23	99.4
Position 3, outer right	2.87	13.8	100

Table 4.6 - RMS slope error, defocus and intercept factors

The average RMS slope error across all facets is 2.54 mrad for position 1, 2.70 mrad for position 2 and 3.11 mrad for position 3. This magnitude of error is typically found when measuring parabolic troughs, and it is often quoted as a target to achieve for a high level of performance. These are significantly lower than the values found for the Ronda mirrors at ENEA, which were partially installed. The intercept factors are very close to 100%, which implies that all the light striking the mirrors are reflected to the absorber tube. However, it should be noted that these calculated intercept factors do not include other factors such as the finite size of the sun, incidence angle modifiers or effects of scattering.

4.2 Accelerated erosion testing

4.2.1 Air velocity vs. pressure calibration

The air velocity was tested with small anemometer, the collection area of which was close to the size of the nozzle ensuring an accurate reading with little loss of airstream.

Pressure (bar)	Velocity (m/s)
1.0	30-35
0.6	25-30
0.4	20-25
0.2	15-20
0.1	5-10

Table 4.7 - Pressure vs. Air velocity

The velocities measured fluctuated by 2 to 3 m/s depending on the exact position of the anemometer within the test chamber. In addition the pressure gauge installed in the erosion rig has a resolution of 0.2 bar making it impractical to attempt to accurately control the pressure. The values in Table 4.7 reflect the approximate velocity for each approximate pressure value. The calibration table was used to estimate the pressure required and then the anemometer was used to measure the wind speed, which was adjusted with a small valve. In this way it was possible to set the wind speed without relying solely on the pressure readings.

4.2.2 Test parameters used

Two sets of samples were exposed to sand in the erosion rig, the first of these were sample with higher mass of sand and lower velocities to simulate the expected damage using the real climate data. The second set of samples were much lower masses of sand with higher velocities to investigate the damage

caused by gusting winds and short exposures to high velocity sand. The list of tests performed is shown in Table 4.8.

Sample	Air velocity (m/s)	Sand mass (g)
1	10	46.0
2	5	4.0
3	10	4.0
4	15	4.0
5	20	4.0
6	25	0.1
7	25	0.5
8	25	1.0
9	25	0.5
10	30	0.5
11	20	0.5
12	25	0.2
13	25	0.3
14	25	0.4
15	25	0.6
16	25	0.7
17	25	0.8
18	25	0.9
19	25	1.5
20	25	2.0

Table 4.8 - Erosion tests performed

Figure 4.81 shows a typical sample after it has been placed in the erosion rig, with the impact area visible as a lighter circular area. Towards the top left of the image an area where the dust residue was wiped off can also be seen. Each mirror had a fine layer of dust that had deposited onto the glass, which was easily wiped off. This was done before any reflectance measurements were made so as to only investigate the actual damage done, rather than any influence of dust deposits resulting in the image shown in Figure 4.82. This sample is mirror 8, which had been subjected to 1 g of sand with an air speed of 25 m/s.

Sample 1, subjected to 46 g of sand with an air speed of 10 m/s can be seen in Figure 4.83, which shows a significant dust deposit on the surface of the mirror.

An attempt was made, both by dry wiping and then wet wiping, to remove as much dust as possible from the mirror, but some remained as can be seen in Figure 4.84.

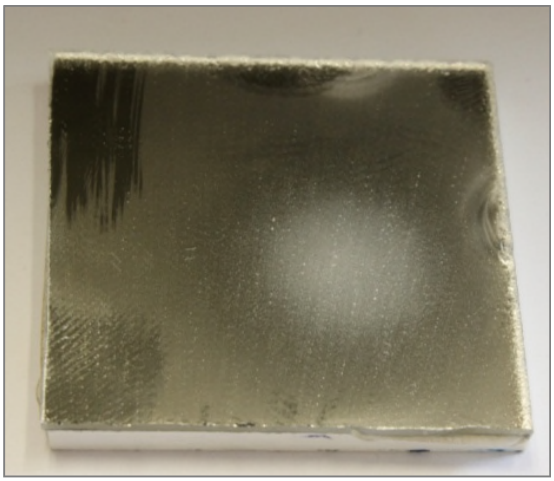

Figure 4.81 - Sample 8 after sand erosion - before cleaning

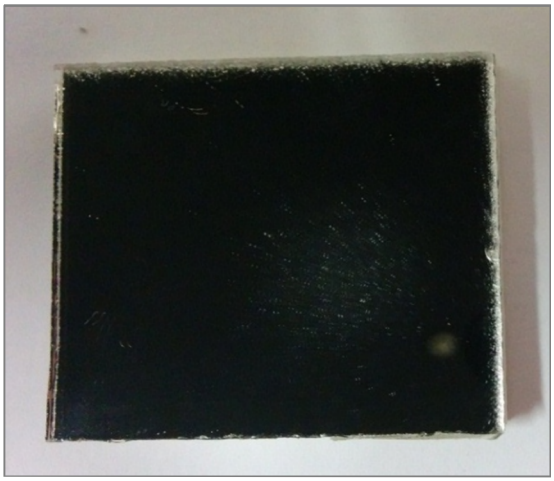

Figure 4.82 - Sample 8 after sand erosion - after cleaning

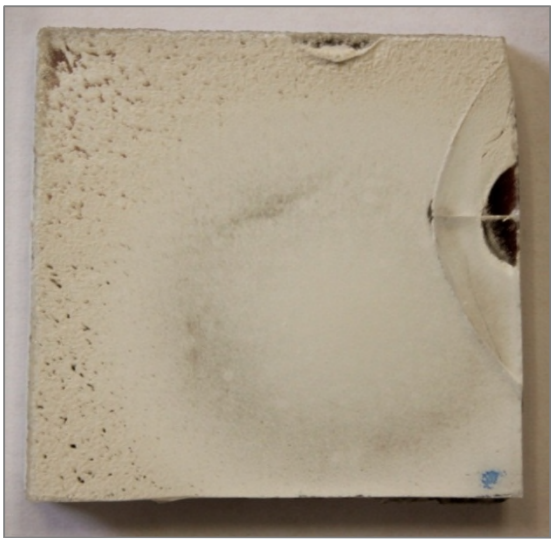

Figure 4.83 - Sample 1 after sand erosion - before cleaning

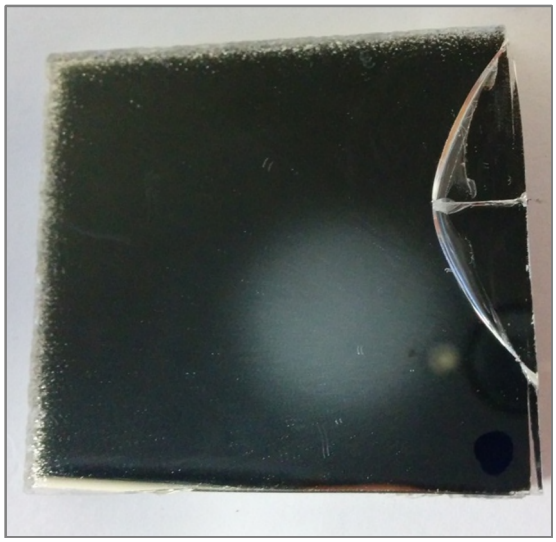

Figure 4.84 - Sample 1 after sand erosion - after cleaning

Upon visual inspection there were few crack sites that were visible to the naked eye, when compared with the higher velocity samples. However the reflectance loss of the 46 g sample was much higher than the low mass samples. This indicates that much of the light is being scattered by the remaining dust that has stuck to the surface of the mirror. This quantity of sand and dust sticking to the

surface of the mirror is not typical of the mirrors that are found on power plant sites. This implies that using such a large amount of sand is not an accurate representation of a year of exposure, as it does not include ‘clean’ wind or washing of the mirrors which following a sandstorm would typically remove much of the sand and dust that would accumulate.

4.2.3 Reflectance

The specular reflectance was measured using the spectrophotometer with a 35 degree incident angle over the full wavelength range of 200 nm to 2500 nm in 0.5 nm intervals. As the reflectance measurement is a relative measurement a baseline spectrum was recorded first. This baseline was a reference aluminium first surface mirror, the spectrum of which can be compared to previous measurements of the same mirror to check the spectrophotometer is correctly set up. Any subsequent measurements are then relative to this aluminium mirror. An uneroded mirror was then measured to provide a reference mirror to compare the eroded mirrors to. The spectrum for the reference mirror is shown in Figure 4.85.

Values of reflectance over 100% indicate where the reference mirror was more reflective than the aluminium calibration mirror. This highlights that the measurements of reflectance are not absolute values, but relative to a constant reference. Spectra recorded were therefore adjusted such that they are relative to a reference mirror rather than a calibration mirror. The peak discontinuity at 800 nm was due to internal switching of the diffraction grating within the spectrophotometer to cover the full range of wavelengths. Each spectrum was weighted against the solar spectrum, as shown in Figure 4.86 and detailed previously, to give single reflectance values for each mirror. These can then be compared to one another.

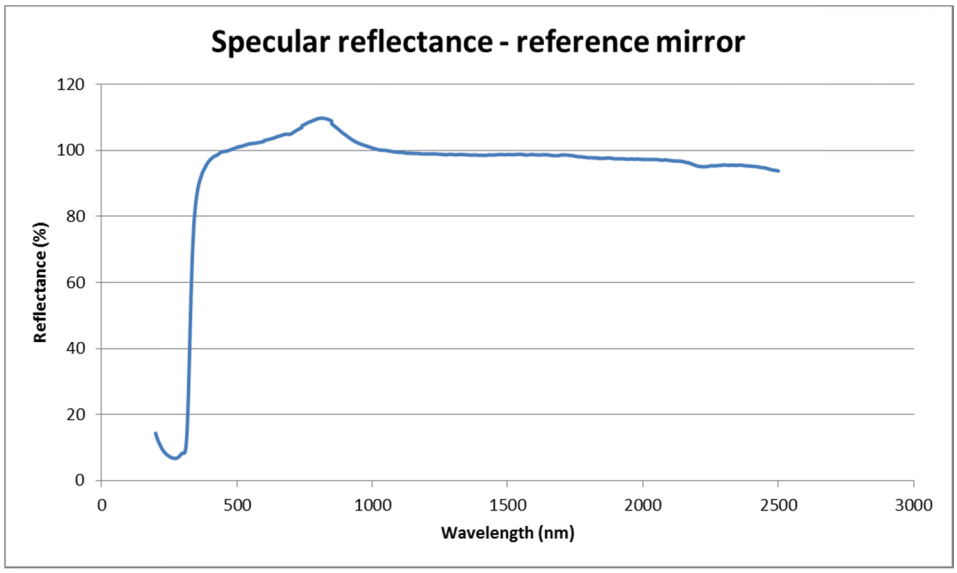

Figure 4.85 - Specular reflectance - reference mirror

The solar spectrum shows a peak in the visible around the same wavelength as the peak reflectance of the mirror sample, indicating a good reflectance and so concentration of the solar energy. The solar weighted specular reflectance values relative to the reference undamaged mirror are shown in Table 4.9.

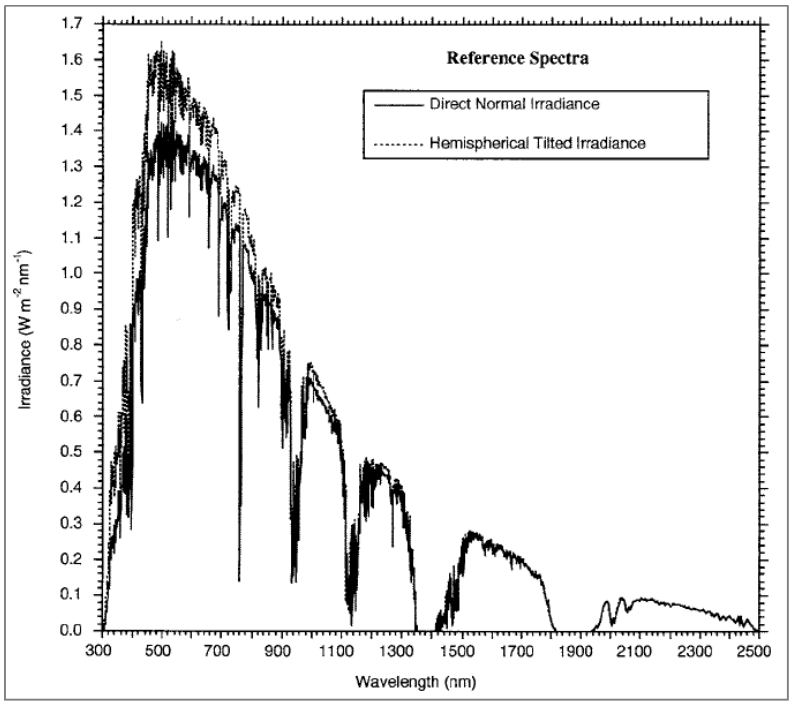

Figure 4.86 - Solar spectrum

Sample	Air velocity (m/s)	Sand mass (g)	Relative specular reflectance (%)
Ref	0	0	100.00
1	10	46	51.29
2	5	4.0	83.45
3	10	4.0	83.55
4	15	4.0	70.91
5	20	4.0	64.60
6	25	0.1	98.57
7	25	0.5	95.36
8	25	1.0	88.94
9	25	0.5	94.78
10	30	0.5	85.61
11	20	0.5	99.22
12	25	0.2	97.98
13	25	0.3	95.74
14	25	0.4	96.79
15	25	0.6	92.36
16	25	0.7	92.73
17	25	0.8	91.69
18	25	0.9	90.76
19	25	1.5	89.76
20	25	2.0	86.18

Table 4.9 - Specular reflectance results

The hemispherical reflectance was measured for each of the samples in the same manner as the specular reflectance and can be seen in Table 4.10. As the hemispherical reflectance measurement captures all the light that is scattered and the specular only captures that which is reflected along the incident angle, the fact that the hemispherical reflectances do not reduce as much as the specular reflectances indicates that majority of the reflectance loss is due to scattering of the light rather than absorption. This is particularly apparent for sample 1, the 46 g sand mass sample, which reduces to 51% specular reflectance but only 95% hemispherical reflectance. There is an overall reduction in both specular and hemispherical reflectances as both the sand mass and air velocities are increased, which is to be expected as more damage will be done to the mirrors in the form of cracks which scatter the light.

Sample	Air velocity (m/s)	Sand mass (g)	Relative hemispherical reflectance (%)
Ref	0	0	100.00
1	10	46	95.05
2	5	4.0	99.57
3	10	4.0	99.24
4	15	4.0	98.20
5	20	4.0	98.12
6	25	0.1	99.76
7	25	0.5	99.19
8	25	1.0	97.54
9	25	0.5	99.10
10	30	0.5	99.01
11	20	0.5	100.04
12	25	0.2	99.77
13	25	0.3	99.62
14	25	0.4	99.56
15	25	0.6	98.54
16	25	0.7	98.59
17	25	0.8	98.59
18	25	0.9	97.52
19	25	1.5	97.97
20	25	2.0	96.05

Table 4.10 - Hemispherical reflectance results

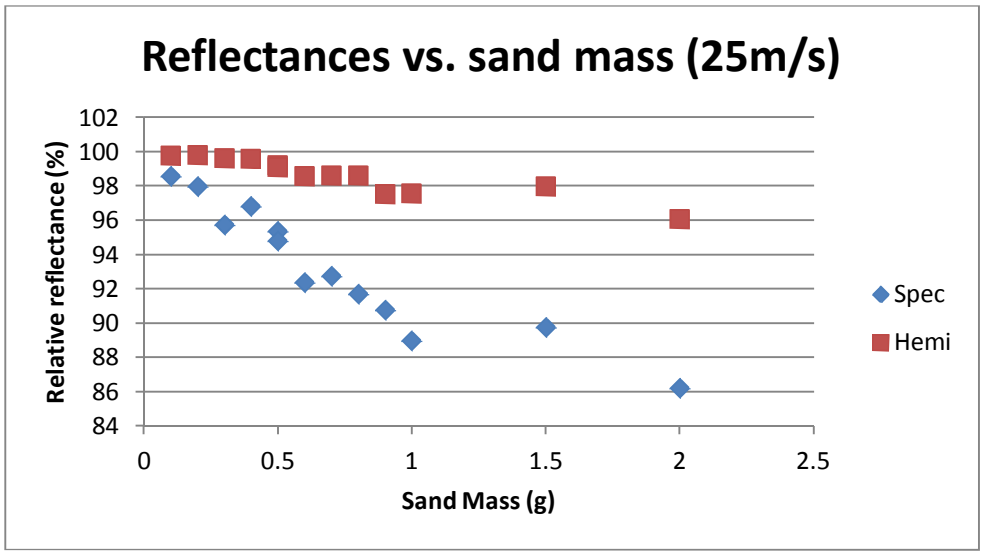

Figure 4.87 - Graph of reflectances against sand mass at 25 m/s

This reduction can be clearly seen in Figure 4.87, where both the specular and hemispherical reflectances are shown as a function of the sand mass with respect to the reference mirror.

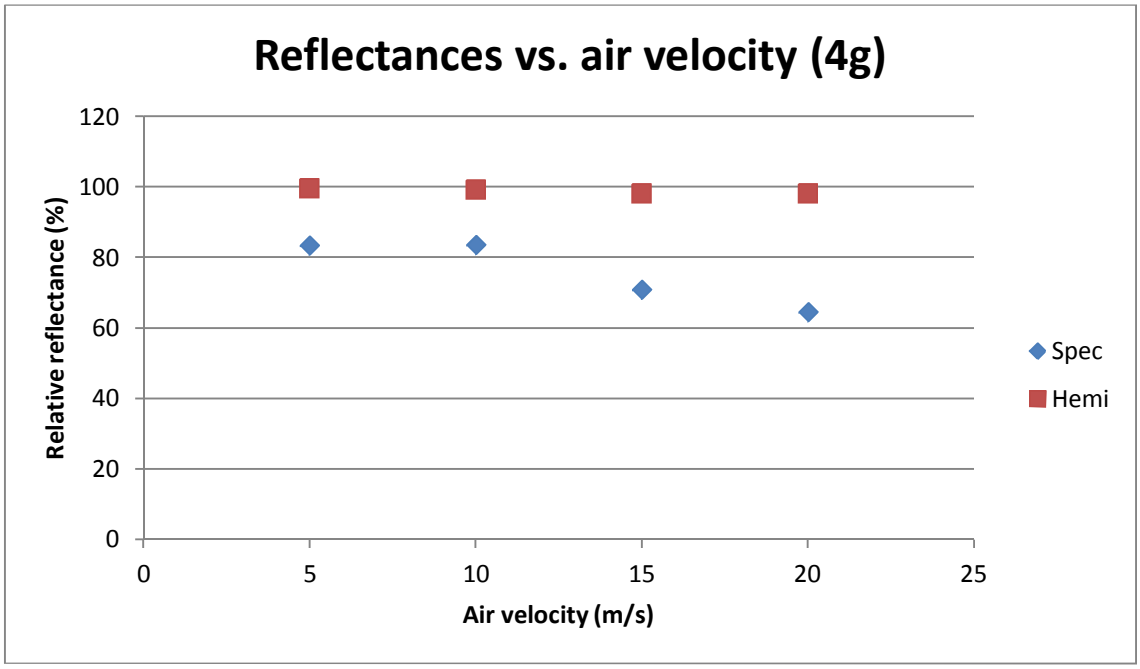

Figure 4.88 - Graph of reflectances against air velocity at 4 g of sand

Figure 4.88 shows the reduction as a function of air velocity for the 4 g of sand samples. The hemispherical reflectance is not significantly affected at these speeds; however the specular reflectance shows an immediate reduction to 83% even at 5 m/s and then continues to decrease to 64% at 20 m/s. This is likely due to the increased quantity of dust that has permanently deposited on the surface, as at these low speeds there is little visible cracking.

4.2.4 Microscopy

Using different magnification lenses the samples were inspected and recorded using the optical microscope, for comparison against one another and to identify any damage that has occurred. The images obtained were visually inspected and then processed through the image analysis software ImageJ to calculate the damage areas.

There were still significant deposits left following the attempts to remove the excess dust from the 46 g sample, which can be clearly seen in Figure 4.89. At higher magnification as shown in Figure 4.90 it is clear that the defects seen are particles stuck to the surface rather than typical crack sites. The specification of the MIL sand indicates that less than 7% of the total weight of sand has a diameter less than 75 microns.

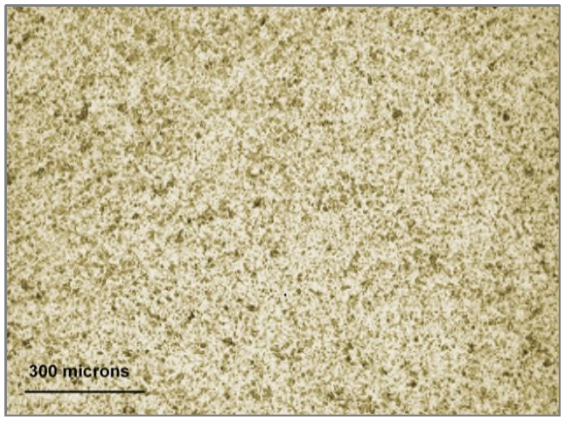

Figure 4.89 - Sample 1 optical microscopy 5X

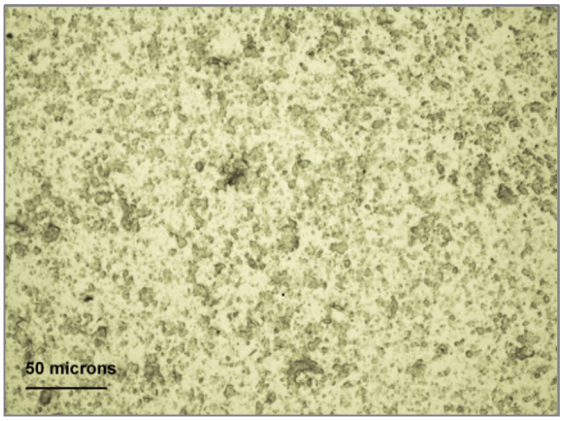

Figure 4.90 - Sample 1 optical microscopy 20X

The sizes of the defects seen in Figure 4.90 are of the order of 10 microns or smaller, implying that the MIL sand has a significant amount of dust within it. This dust can be seen when the MIL sand is inspected under a scanning electron microscope (SEM), shown in Figure 4.92. The grains of sand are clearly seen, along with a significant amount of much smaller particulate matter both surrounding and on the grains themselves. Natural Saharan sand sample, as shown in Figure 4.93, does not contain this very fine dust, which is due to the crushed quartz production method of the MIL sand.

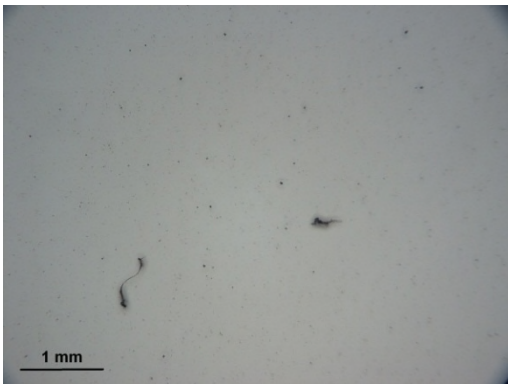

(a) - 5m/s (2.5X)

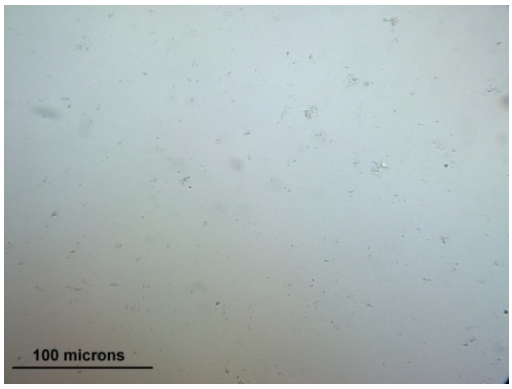

(b) - 5m/s (40X)

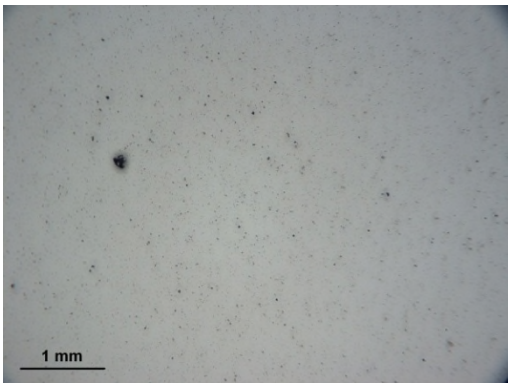

(c) - 10m/s (2.5X)

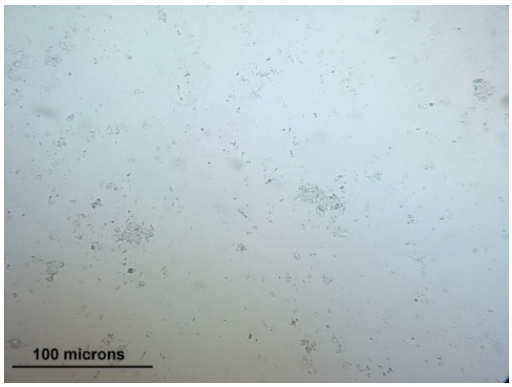

(d) - 10m/s (40X)

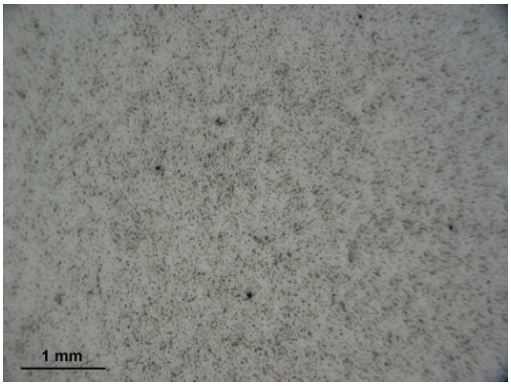

(e) - 15m/s (2.5X)

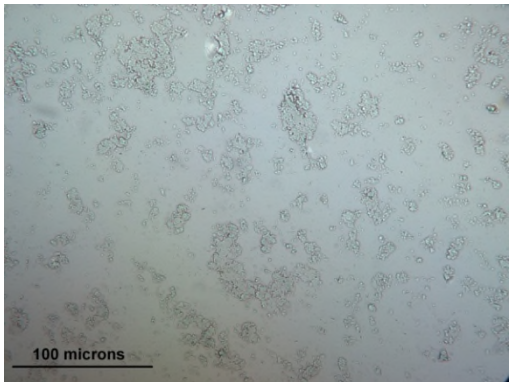

(f) - 15m/s (40X)

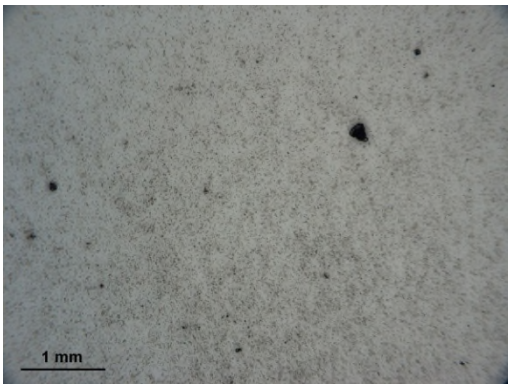

(g) - 20m/s (2.5X)

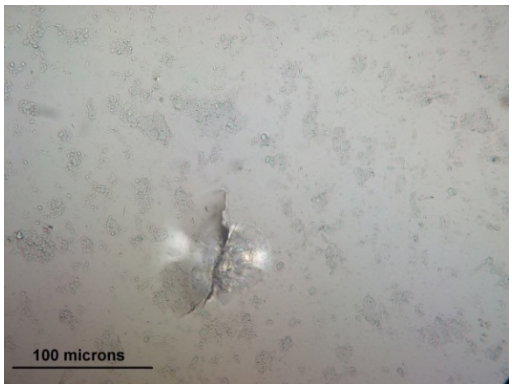

(h) - 20m/s (40X)

Figure 4.91 - 4 g sand microscopy

Figure 4.91 shows the microscope images for the 4 g of sand samples, with the leftmost image of each row at 2.5X magnification and the rightmost at 40X magnification. The air speed increases from top to bottom. It can clearly be seen that as the air speed increases from 5 m/s to 20 m/s the amount of defects visible on the surface increase also. However only in Figure 4.91f and Figure 4.91h, with air speeds of 15 m/s and 20 m/s respectively, can any cracks be seen. These cracks are much larger than the majority of the defects that can be seen, which are particulate matter stuck to the surface. There is an increase in the amount of this stuck material as the speed increases indicating that speed is an important factor in how well the particles adhere, as well as the amount of sand used.

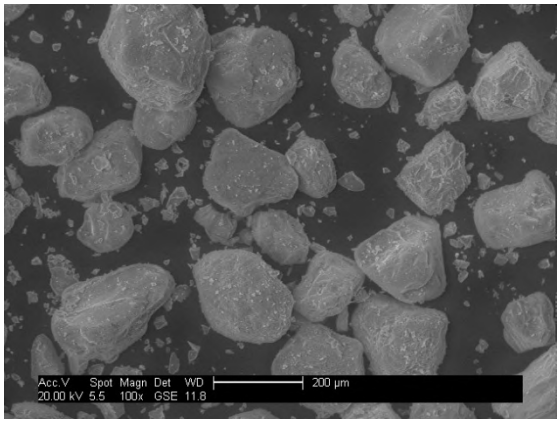

Figure 4.92 - MIL sand SEM image

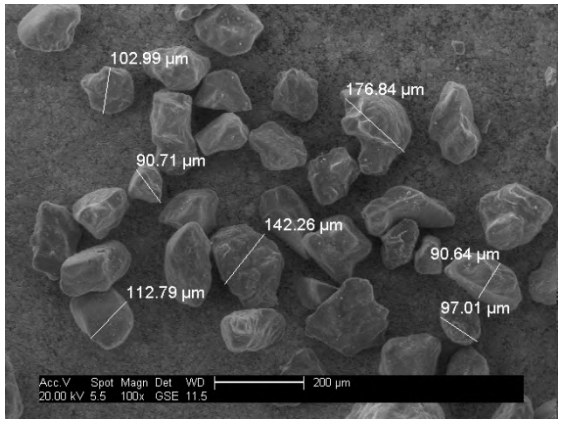

Figure 4.93 - Natural Saharan sand SEM image

Figure 4.94 shows microscopy images captured of samples 11, 9 and 10 respectively. These have been subjected to 0.5 g of sand each at 20 m/s, 25 m/s and 30 m/s respectively. It is clear to see that the number of damage sites increases in line with the air speed. This is to be expected as with a higher air speed there will be more particles at higher velocities. These have higher kinetic energy and when this kinetic energy is high enough the glass will crack upon impact. The large increase in damage seen between 20 m/s and 25 m/s shows that there likely to be a threshold air speed at which the kinetic energy becomes high enough to cause significant damage in the 20 to 25 m/s range. This is an important factor to consider when deciding upon the location for a CSP plant

containing glass mirror surfaces. Extended weather monitoring should be performed prior to installation to check the average and peak wind speeds expected to ensure that they are well below the 20 to 25 m/s range. This will decrease the likelihood of significant damage during sandstorm events and ultimately increase the lifetime of the collectors.

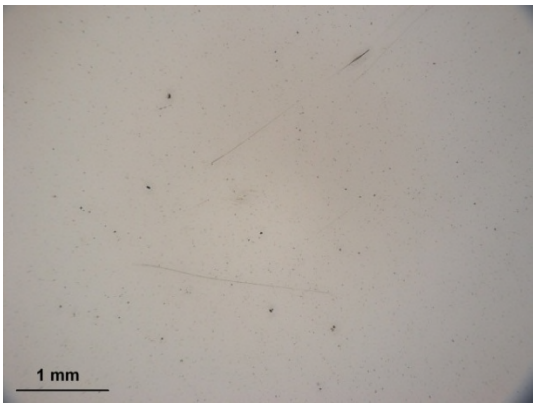

(a) - 0.5 g at 20 m/s

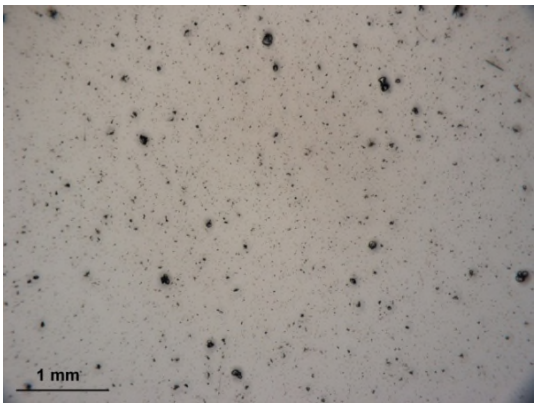

(b) - 0.5 g at 25 m/s

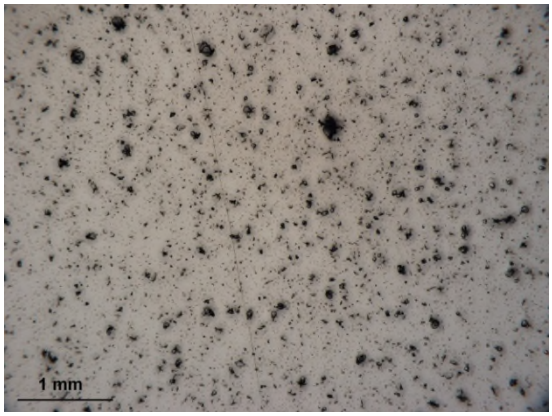

(c) - 0.5 g at 30 m/s

Figure 4.94 - Low sand mass microscopy images, increasing air speed

Figure 4.95 shows how increasing the mass of sand affects the samples with 0.1 g, 0.3 g, 0.5 g, 0.8 g, 1 g and 2 g shown respectively. The number of damage sites seen increases with the sand mass but the size of each of the damage sites does not significantly change unlike with increasing the air speed. This is due to the kinetic energy not increasing with sand mass, only the number of impacts occurring.

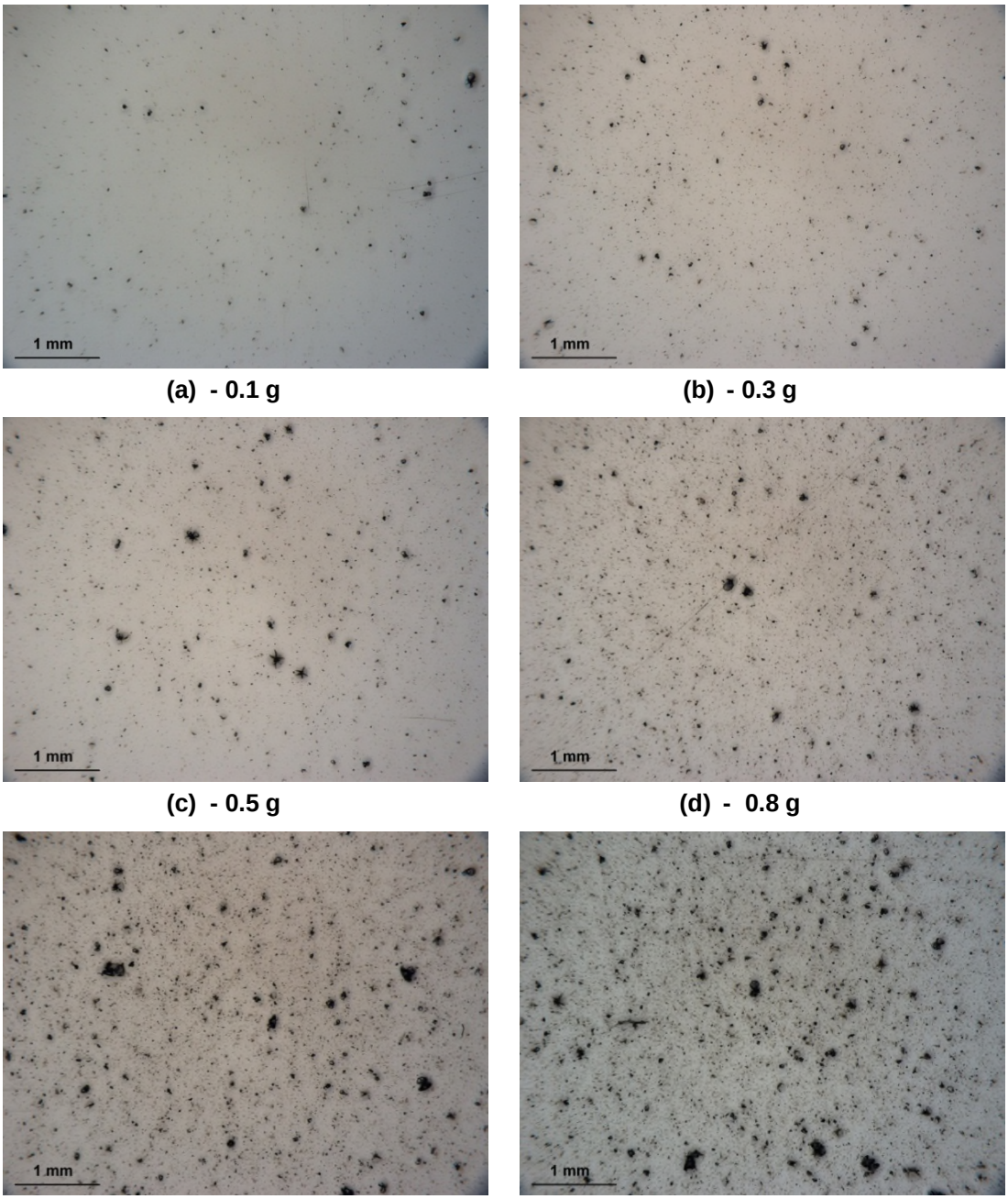

(a) - 0.1 g **(b) - 0.3 g**

(c) - 0.5 g **(d) - 0.8 g**

(e) - 1.0 g **(f) - 2.0 g**

Figure 4.95 - Low sand mass microscopy images, increasing sand mass

To better understand the damage characteristics the microscope images for each sample were studied using the image analysis software ImageJ. The images were thresholded to produce a binary image, which was then analysed using a particle detection algorithm built into the software. This counts the number and size of dark areas on the image and compares it to the total size of the image in pixels and by using the scale bar in the image the results were

calculated in microns. The results of this processing can be seen in Table 4.11, which shows the total number of damage sites found, the average area of each of the individual damage sites, the total area covered by the damage sites as a whole and the percentage of the total image area covered by damage.

Sample	Speed (m/s)	Mass (g)	Spec. Refl. (%)	Hemi. Refl. (%)	Count	Average site area (μm^2)	Total area ($10^3 \mu m^2$)	% of total area
Ref	0	0	100.00	100.00	47	65.16	549.05	0.04
1	10	46	51.29	95.05	9,088	60.41	27.66	25.48
2	5	4.0	83.45	99.57	864	32.01	53.04	0.30
3	10	4.0	83.55	99.24	1,698	31.23	673.55	0.59
4	15	4.0	70.91	98.20	12,848	52.42	793.73	7.49
5	20	4.0	64.60	98.12	16,734	47.43	78.76	8.83
6	25	0.1	98.57	99.76	882	89.29	159.76	0.87
7	25	0.5	95.36	99.19	2,198	72.68	425.80	1.77
8	25	1.0	88.94	97.54	5,419	78.57	169.23	4.73
9	25	0.5	94.78	99.10	1,816	93.19	748.63	1.88
10	30	0.5	85.61	99.01	5,006	149.54	41.58	8.32
11	20	0.5	99.22	100.04	2,926	14.21	119.71	0.46
12	25	0.2	97.98	99.77	1,515	79.02	156.97	1.33
13	25	0.3	95.74	99.62	2,569	61.10	239.31	1.74
14	25	0.4	96.79	99.56	3,872	61.80	336.30	2.66
15	25	0.6	92.36	98.54	5,221	64.41	319.96	3.74
16	25	0.7	92.73	98.59	3,048	104.97	340.58	3.56
17	25	0.8	91.69	98.59	4,938	68.97	477.54	3.78
18	25	0.9	90.76	97.52	6,360	75.08	495.18	5.31
19	25	1.5	89.76	97.97	4,190	118.18	642.13	5.50
20	25	2.0	86.18	96.05	6,956	92.31	549.04	7.14

Table 4.11 - Damage site analysis

Figure 4.96 shows the relationship between the specular reflectance and the total area of damage that is present on the sample. The total damaged area increasing is caused by an increase in the number of cracks present on the surface. It is these cracks that cause the light to be scattered and so the specular reflectance will reduce. The total damaged area is strongly linked to the sand mass that is used to damage the sample. As shown in Figure 4.97, for a constant air speed, as the sand mass is increased the total damaged area also increases almost linearly.

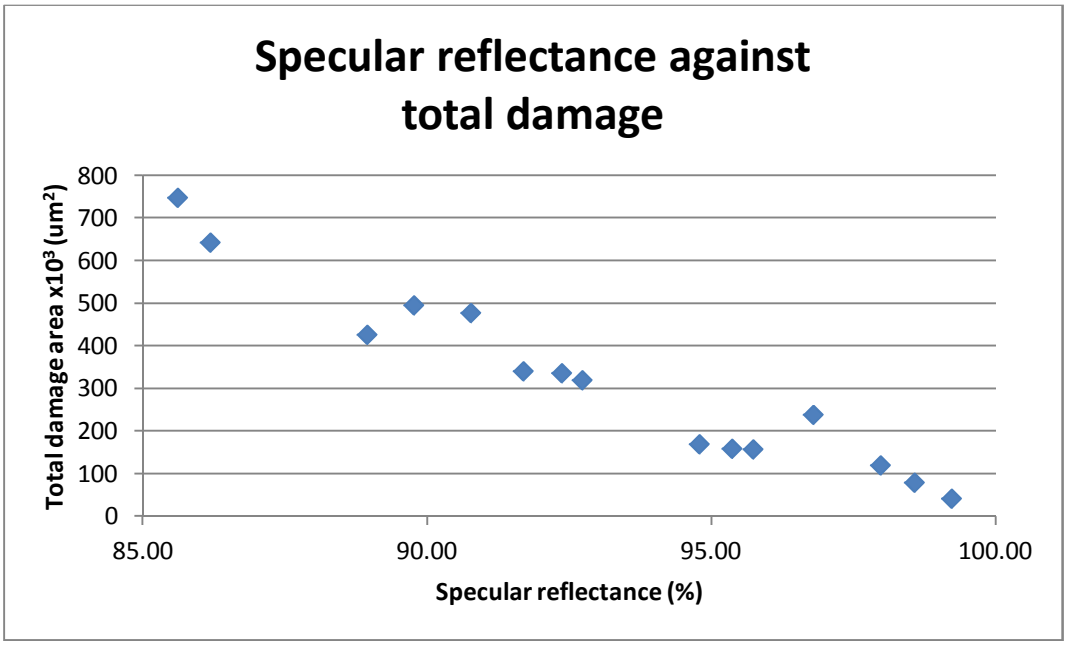

Figure 4.96 - Effect of total damage area on specular reflectance

Figure 4.98 shows again that the size of each of the damage sites does not strongly depend on the mass of sand used. The small increase in damage size is due to the fact that the sand particles are not all travelling at the same speed and only some of them will have the required kinetic energy to crack the glass. By increasing the amount of sand, the same distribution means that there will be a higher number of particles travelling at the required speed. The average damage site area over all the samples at 25 m/s is 81.5 μm^2 with a standard deviation of 16.6 μm^2. The damage site areas for lower air speeds range from 31 μm^2 to 52 μm^2. These are significantly lower than for 25 m/s and outside the standard deviation and similarly for the 30 m/s sample with an average damage site area of 149 μm^2.

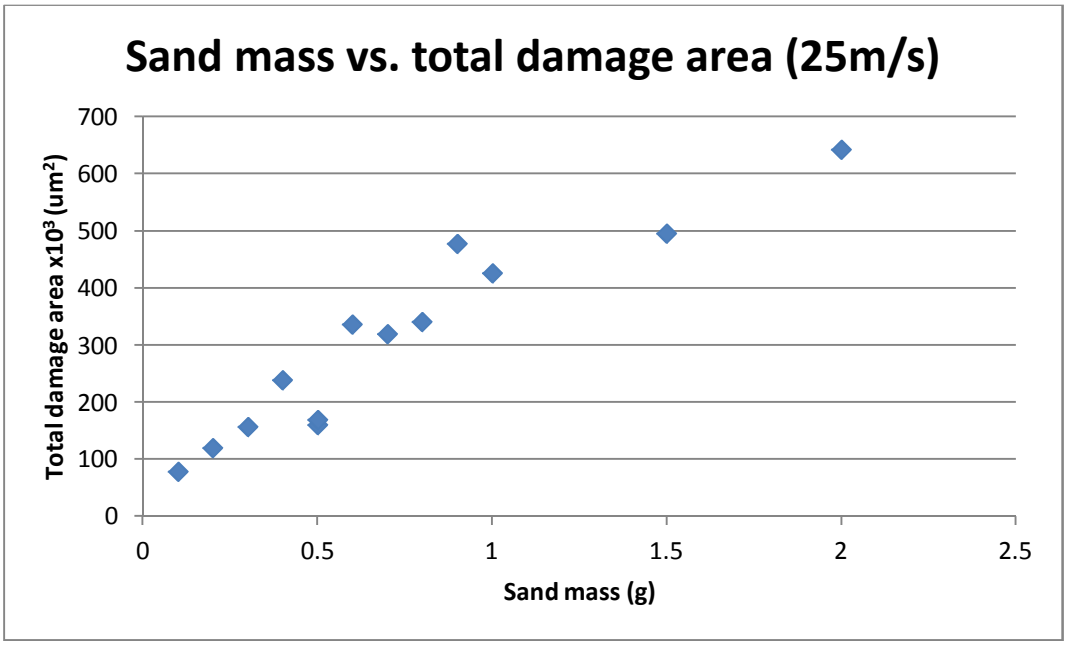

Figure 4.97 - Effect of sand mass on total damage area

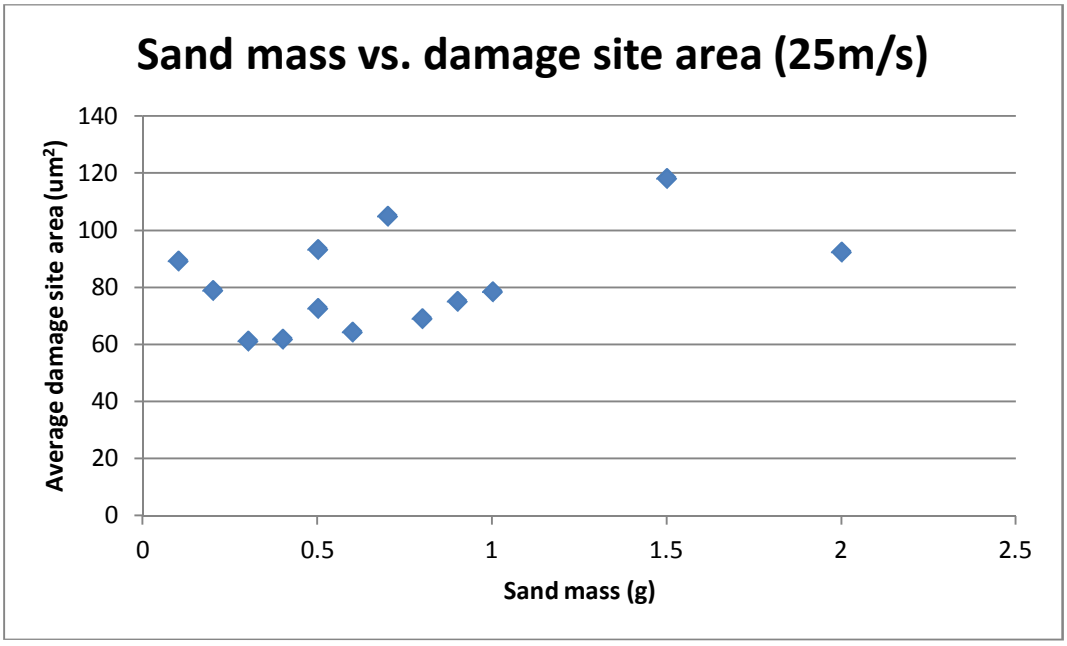

Figure 4.98 - Effect of sand mass on damage site area

5 CONCLUSIONS

The aim of this thesis was to develop and characterise techniques to measure the form and assess the durability of mirror surfaces for concentrating solar power applications. This aim was achieved by selecting and developing photogrammetry as a measurement technique, by validating it to traceable standards and assessing the form of a number of existing CSP installations. Additionally climate data was gathered and assessed to define sand erosion testing, which was performed on real CSP mirror samples.

5.1 Photogrammetry

The requirement for the form measurement technique was a highly portable system with an accuracy of better than 100 µm. Low set up and measurement time, flexibility for different measurement types, and low cost were also requirements. Photogrammetry was selected over deflectometry, VSHOT and laser tracker as it was the most flexible and portable system, was of sufficient accuracy and had a low cost. The portability, flexibility and speed of photogrammetry were demonstrated with measurements taken across a variety of CSP sites globally. The equipment requirements for photogrammetry are minimal and cost effective at less than £2,000, requiring a camera, targets and software only, all of which can be easily transported with the user. This cost is an order of magnitude less than the cost of other systems. Application of targets and measurement of the gross shape of a single 12 m collector assembly can be completed within half a day. Photogrammetry is also capable of measurements independent of the position and direction of the collector, allowing a number of orientations to be examined, without requiring the removal and reapplication of targets. The only restrictions on collector position are due to the requirement of line of sight between camera and targets.

A photogrammetry capability was developed, a Canon 600D DSLR camera and static cling vinyl sheet targets were chosen and the camera settings and measurement parameters defined. The camera settings investigated were the

aperture and the shutter speed, with camera positioning and number of photographs also considered. Photogrammetry has been previously used by several R&D centres for measuring solar concentrators; however the experimental investigations into the definition and analysis of the camera settings and their influence on the measurement accuracy are a key result from this thesis, which will ensure the optimal results from photogrammetry.

Another key contribution is the use of a laboratory based large coordinate measuring machine, traceable to international standards, to validate the developed photogrammetry technique. This showed a correlation between photogrammetry and the CMM of 76 µm RMS over the whole mirror facet surface. Measurements of mirror form showed errors of 0.4 mm RMS over the whole facet with a peak to valley value of 1.4 mm. The determined accuracy of photogrammetry is therefore sufficient to be able to measure the errors of such mirrors, magnitudes of which are typically in excess of 3 to 4 mm.

Successful measurements performed on traditional EuroTrough thick glass mirrors and novel Ronda thin glass mirrors clearly showed differences between the two different parabolic trough constructions. The static shape of the mirror was captured in various positions that it would be in during tracking using the developed photogrammetry technique. Subsequent analysis then identified the adjustments necessary for optimal performance.

The thin mirrors, when adjusted to the optimal shape in the lab, clearly showed effects from the support structure in the form of four high deviation areas, which correspond to four corner support point areas. These areas had form errors in the region of 0.3 mm greater than the other parts of the mirror. The form errors measured on-site covered a range from 3.9 mm to 7.9 mm RMS. The susceptibility of the thin glass mirrors to the local shape deviations cause significant local slope errors, up to 20 mrad, leading to a higher proportion of stray light rays. The proportion of light striking the absorber tube for the on-site measurements was less than 60%, although lab tests showed that optimally adjusted mirrors can achieve 100%.

Measurements of the thick glass mirrors have shown that they maintain their form following movement, with the exception of one of the facets, which may have had an incorrect support adjustment. The thick glass mirror form errors covered a range between 0.41 mm and 1.12 mm RMS. The thick glass mirrors have low magnitude shape errors and features generally cover a large area of the facet. This causes smaller local slope errors and therefore fewer stray light rays. The proportion of calculated light rays which struck the absorber tube exceeded 98.5% in all cases.

A direct comparison of the performance of the thin glass mirrors against the thick glass mirrors is not possible from the results obtained due to the incomplete installation of the thin glass mirrors. The laboratory form error of the thin mirror match the on-site form errors of the thick mirrors. This implies that it is possible to adjust the thin mirrors to achieve the same performance as the thick mirrors. The thin mirrors are lighter and have more adjustment; however they are more susceptible to local distortions than the thick mirrors.

5.2 Sand erosion

There are no current international standards dealing with sand erosion of CSP mirror surfaces. Existing standards, such as MIL-STD-810G, deal with erosion of materials with higher air velocities, 18 to 29 m/s, than are typically found during sandstorm events. Such standards are adapted for lower wind speeds and modified particle concentrations. To establish the testing parameters for CSP mirrors, climate data was downloaded for a two year period for Borg El-Arab in Egypt. This data was analysed and showed that there were 46 hours of sandstorm per year with an average wind speed of 9.6 m/s and wind gusts in excess of 25 m/s. Calculations were done showing that 1 g of sand is equivalent to 1 hour of sandstorm when using the erosion rig. A one year period of time was simulated, consisting of 46 g of MIL-E-5007C synthetic sand at 10 m/s. The sand adhered strongly to the surface of the mirror in the erosion rig and built up a significant layer, acting as a barrier to prevent sand striking the mirror thus reducing the potential damage.

These results question the validity of the current testing procedures used for accelerated erosion testing. A key outcome is that dust removal processes should be incorporated into the ageing process, as sandstorm events are infrequent and during the non-sandstorm periods the wind will remove much of the dust built up during the sandstorm. In addition, following such events and on a regular basis, the mirrors are washed which removes any dust build up to maintain their reflectance. The mirrors on-site are also not plane glass directly facing the incoming sand, as is done in the erosion rig. Typically there will be a range of angles at which the sand will strike the surface, especially for a parabolic trough type configuration with significant turbulent airflows. Additionally the mirrors are usually stowed in a safe position to minimise the surface area exposed. Such turbulence and use of stow positions are difficult to simulate, however they will act to reduce damage done and so the erosion rig can be considered as a worst case setup.

Further erosion testing was performed with a range of air velocities and sand quantities. Across all quantities of sand there was minimal damage of the mirror surface at the sandstorm air speed of 10 m/s, which can be seen when studying on-site mirrors that have been exposed to the environment for many years. Such mirrors show little visible damage on the glass surface, with the majority of defects in the back paint and silvered layers caused by corrosion. Erosion tests were also performed at higher air velocities with small quantities of sand to simulate gusting during sandstorms. At speeds of greater than 15 m/s significant damage was seen with all quantities of sand. This implies that although minimal damage is seen during average sandstorm conditions it is important to consider the extreme cases where substantial damage can be done over a short period of time. It is therefore important that protective collector positions, such as stow, are considered during higher wind speed periods. Additionally the climate of potential CSP sites should be carefully considered with respect to possible sandstorms to determine the damage which may be done to the mirrors during their lifetime.

The damage done to the surface ultimately causes a loss in reflectance of the mirror, both in hemispherical and specular forms. The hemispherical reflectance loss provides the amount of light that is being absorbed by the mirror rather than being reflected. This absorption is caused both by the opaque sand that is sticking to the surface and also by some extreme scattering that causes a much longer path length through the glass towards the edges, leading to a higher probability of light absorption by the glass material. This loss of reflectance increases as the sand mass increases but is less than 5% for all air velocities. The loss of specular reflectance also increases with the sand mass and with the air velocity, due to the damage sites themselves scattering the light sufficiently to not be collected by the detector. This loss is greater than the hemispherical loss, exceeding 14% for sand masses less than 4 g and up to 48% with 46 g of sand. This shows that the dominant performance loss of the mirror is due to the scattering of the light from damage sites, rather than any absorption of light. This scattering becomes a more important factor as the distance from the mirror to the receiver is increased, for instance the distance between a heliostat mirror and a central tower receiver can exceed hundreds of metres. The sandstorm frequency and intensity are therefore key factors in determining which CSP technology to use, as parabolic trough may be more suitable than central towers, due to their smaller distance between collector and receiver. The erosion test simulating a single year of wear produced a 50% drop in performance; however it is clear that such large reflectance losses are not typically seen in operational collectors over such periods of time. This reinforces the fact that attempting to simulate extended periods of time is more complex than simply increasing the quantity of sand used.

The techniques and results obtained have been applied for in field measurements of collector surfaces for the MATS and STAGE-STE FP7 European projects.

5.3 Future possible work

Lighting levels during photogrammetry is an area which would benefit from future work. The light levels within a laboratory setting are ideal and consistent; however these levels can change dramatically between different sites, potentially affecting the accuracy of the results. One approach to investigate the effect that lighting has on photogrammetry accuracy would be the use of a known artefact. This could be characterised in the laboratory and then measured on-site, the results giving an indication of how the accuracy may be affected. Considerations for such artefacts include ensuring a rigid and thermally stable object, the size of which must be of the order of the size of the mirror, whilst also remaining practical for CMM measurements and portability. An example of an artefact may be two perpendicular scale bars of known length with photogrammetry targets at the extremes. It should be made from a material with low flexibility and thermal expansion, remaining lightweight so that it has minimal influence on the mirror shape when attached to the structure.

As technology improves, higher resolution cameras become available at lower cost. By using these higher resolution cameras it would be possible to maintain the accuracy of photogrammetry while increasing the distance from the targets, providing a wider field of view. Combining this wider field of view with an aerial platform, for example with a multi-rotor drone, would enable faster measurements of whole collector fields. Increased resolution cameras would also allow higher resolution measurements to be taken to reveal smaller variations in the mirror surfaces. These smaller scale errors may become important if thin glass mirrors are to be used due to their increases local flexibility and the influence of the moulded backing.

The erosion rig performed well with smaller samples of sand, however when attempting to simulate extended periods of time there was significant build-up of sand on the surface, as discussed. To aid in the removal of this sand the erosion rig may be redesigned to incorporate periodic cleaning processes and times of clean air as would occur naturally. The sand used in the erosion

process was a standard crushed quartz sand containing particles ranging from 75 μm up to 1 mm. Upon inspection of small quantities of natural Saharan sand obtained from the desert floor it was noted that the natural sand was more rounded and had fewer of the smaller particles present than the quartz sand. It should be expected that the actual sand striking the mirror surface would have a different particle size distribution to that collected from the desert floor. Different particle sizes will be lifted to different heights by the wind and as such different parts of the mirrors may be subjected to different particle sizes. To more accurately simulate the sandstorm conditions it would be beneficial to collect the airborne sand during a sandstorm event as a function of height and wind speed. This would then enable a more accurate input sand composition to be used for ageing tests. In addition to validate the ageing technique samples of glass may be left exposed to the site environment for extended periods of time. With the local conditions recorded by weather stations to include wind speeds and sandstorm events, the samples can be compared to mirrors which have been exposed to the same simulated conditions. The erosion procedures may then be adjusted to better match the actual recorded damage which occurs.

REFERENCES

Adjouadi, N., Laouar, N., Bousbaa, C., Bouaouadja, N. and Fantozzi, G. (2007) 'Study of light scattering on a soda lime glass eroded by sandblasting', *Journal of the European Ceramic Society*, 27(10), pp. 3221–3229.

Alhaider, M.A. (1986) 'Radio wave propagation into sandstorms-system design based on ten-years visibility data in Riyadh, Saudi Arabia', *International Journal of Infrared and Millimeter Waves*, 7(9), pp. 1339–1359.

Ali, B.F. (1990) 'Theoretical study of main factors affecting the heliostat field design of tower power plant', *Energy Conversion and Management*, 30(2), pp. 101–106.

Areva Solar (2012) *Areva Solar: Our Technology and Features*. Available at: http://www.areva.com/EN/solar-198/arevasolarour-technology.html (Accessed: 1 October 2012).

Arqueros, F., Jiménez, A. and Valverde, A. (2003) 'A novel procedure for the optical characterization of solar concentrators', *Solar Energy*, 75(2), pp. 135–142.

ASTM (2012) *G173-03: Standard Tables for Reference Solar Spectral Irradiances : Direct Normal and Hemispherical on 37deg Tilted Surface*. West Conshohocken, PA, USA: ASTM International.

Bagnold, R.A. (1941) *The Physics of Blown Sand and Desert Dunes*. London: Methuen and Co.

Barlev, D., Vidu, R. and Stroeve, P. (2011) 'Innovation in concentrated solar power', *Solar Energy Materials and Solar Cells*, 95(10), pp. 2703–2725.

Bokhari, W. (2011) 'Fresnel's concentrators for domestic cooking using heat stored in therminol 72', *Proceedings of SolarPACES 2011*. Granada, Spain, 20-23 September 2011.

Bouaouadja, N., Bouzid, S., Hamidouche, M., Bousbaa, C. and Madjoubi, M. (2000) 'Effects of sandblasting on the efficiencies of solar panels', *Applied Energy*, 65(1-4), pp. 99–105.

Bouquet, F.L. (1980) 'Aging characteristics of glass mirrors for solar thermal power applications', *Journal of Non-Crystalline Solids*, 40(1-3), p. 627.

Bousbaa, C. (2003) 'Effect Of Sand Blasting On Soda Lime Glass Properties', *Engineering Journal of the University of Qatar*, 16, pp. 125–138.

Bousbaa, C., Kolli, M., Madjoubi, M. a., Malou, Z., Mahdaoui, T. and Bouaouadja, N. (2009) 'Damage survey of a vehicle windshield exposed to sandblasting in Sahara', *Physics Procedia*, 2(3), pp. 1141–1145.

BP (2011) *BP Statistical Review of World Energy June 2011*. Available at: http://www.bp.com/assets/bp_internet/globalbp/globalbp_uk_english/reports_and_publications/statistical_energy_review_2011/STAGING/local_assets/spreadsheets/statistical_review_of_world_energy_full_report_2011.xls (Accessed: 1 June 2012).

Brogren, M. (2004) 'Analysis of the effects of outdoor and accelerated ageing on the optical properties of reflector materials for solar energy applications', *Solar Energy Materials and Solar Cells*, 82, pp. 491–515.

Burgess, G., Shortis, M., Kearton, A. and Garzoli, K. (2009) 'Photogrammetry for dish concentrator construction', *Proceedings of Solar09, the 47th ANZSES Annual Conference*. Townsville, Queensland, 29 September - 2 October 2009.

Cappo, M., Harvey, E. and Shortis, M. (2006) 'Counting and measuring fish with baited video techniques - an overview', *Australian Society for Fish Biology 2006 Workshop proceedings: Cutting-edge technologies in fish and fisheries science*. Hobart, Tasmania, Austrailia, 28-29 August 2006.

Chan, C., Chuang, K. and Chen, W. (2008) 'Increasing cardiopulmonary emergency visits by long-range transported Asian dust storms in Taiwan', *Environmental Research*, 106, pp. 393–400.

Chepil, W.S. and Woodruff, N.P. (1957) 'Sedimentary characteristics of dust storms; Part II, Visibility and dust concentration', *American Journal of Science*, 255(2), pp. 104–114.

Chu, T.S. (1979) 'Effects of sandstorms on microwave propagation', *Bell System Technical Journal*, 58(2), pp. 549–555.

Crawford, J.S., Stewart, J. and Pérez-ullivarri, J.A. (2012) 'A Comparison of Three Portable Reflectometers for Use in Operations and Maintenance of CSP Plants', *Proceedings of SolarPACES 2012*. Marrakech, Morocco, 11-14 September 2012.

Deffenbaugh, D.M., Green, S.T. and Svedeman, S.J. (1986) 'The effect of dust accumulation on line-focus parabolic trough solar collector performance', *Solar Energy*, 36(2), pp. 139–146.

Diver, R.B. and Moss, T.A. (2007) 'Practical Field Alignment of Parabolic Trough Solar Concentrators', *Journal of Solar Energy Engineering*, 129(2), p. 153.

EIA (2009) *International Energy Statistics*. Available at: www.eia.gov/countries/data.cfm (Accessed: 1 September 2012).

El-Gamal, A., Rashad, M. and Ghatass, Z. (2010) 'Radiological responses of different types of Egyptian Mediterranean coastal sediments', *Radiation Physics and Chemistry*, 79(8), pp. 831–838.

Estler, W., Edmundson, K., Peggs, G. and Parker, D.H. (2002) 'Large-Scale Metrology – An Update', *CIRP Annals - Manufacturing Technology*, 51(2), pp. 587–609.

Fend, T., Hoffschmidt, B., Jorgensen, G., Küster, H., Krüger, D., Pitz-Paal, R., Rietbrock, P. and Riffelmann, K.-J. (2003) 'Comparative assessment of solar concentrator materials', *Solar Energy*, 74(2), pp. 149–155.

Forsberg, C.W., Peterson, P.F. and Zhao, H. (2007) 'High-Temperature Liquid-Fluoride-Salt Closed-Brayton-Cycle Solar Power Towers', *Journal of Solar Energy Engineering*, 129(2), p. 141.

Fu, P., Huang, J., Li, C. and Zhong, S. (2008) 'The properties of dust aerosol and reducing tendency of the dust storms in northwest China', *Atmospheric Environment*, 42(23), pp. 5896–5904.

García-Cortés, S., Bello-García, A. and Ordóñez, C. (2012) 'Estimating intercept factor of a parabolic solar trough collector with new supporting structure using off-the-shelf photogrammetric equipment', *Applied Energy*, 92, pp. 815–821.

Gee, R., Brost, R., Zhu, G. and Jorgensen, G. (2010) 'An improved method for characterizing reflector specularity for Parabolic Trough Concentrators', *Proceedings of SolarPACES 2010*, Perpingnan, France, 21-24 September 2010.

Gray, A., Lewandowski, A. and Wendelin, T. (2010) *NREL/TP-5500-48482: Visual Scanning Hartmann Optical Tester (VSHOT) Uncertainty Analysis*. National Renewable Energy Laboratory, USA.

Hagen, L. and Skidmore, E. (1977) 'Wind erosion and visibility problems', *Transactions of the ASAE*, 20(5), pp. 898–903.

Hecht, E. (1974) *Optics*. 1st edn. London: Addison-Wesley.

Heimsath, A., Kutscheidt, G. and Nitz, P. (2011) 'Measuring reflectance-overview and influence on optical performance', *Proceedings of SolarPACES 2011*. Granada, Spain, 20-23 September 2011.

Herrmann, U. and Geyer, M. (2002) '*The AndaSol Project*', Workshop on Thermal Storage for Trough Power Systems, February 20-21, 2002. Available

at: http://www.nrel.gov/csp/troughnet/pdfs/uh_anda_sol_ws030320.pdf (Accessed: 1 January 2012).

Herrmann, U., Kelly, B. and Price, H. (2004) 'Two-tank molten salt storage for parabolic trough solar power plants', *Energy*, 29(5-6), pp. 883–893.

Hexagon Metrology (2013) *Portable Measuring Arms*. Available at: http://www.hexagonmetrology.co.uk/Portable-Measuring-Arms_111.htm (Accessed: 1 August 2013).

Hexagon Metrology (2012a) *Leica Absolute Tracker AT401*. Available at: http://www.hexagonmetrology.co.uk/leica-absolute-tracker-at401_955.htm (Accessed: 1 February 2012).

Hexagon Metrology (2012b) *Help files from Quindos version 7*.

Huang, W. and Han, Z. (2012) 'Theoretical analysis of error transfer from the surface slope to the reflected ray and their application in the solar concentrated collector', *Solar Energy*, 86(9), pp. 2592–2599.

Hubert, M. and Kalman, H. (2004) 'Measurements and comparison of saltation and pickup velocities in wind tunnel', *Granular Matter*, 6(2-3), pp. 159–165.

Ibrahim, A. (2011) 'Renewable energy sources in the Egyptian electricity market: A review', *Renewable and Sustainable Energy Reviews*, 16(1), pp. 216–230.

IEA (International Energy Agency) (2010) *Technology Roadmap: Concentrating Solar Power*. Available at: https://www.iea.org/publications/freepublications/publication/csp_roadmap.pdf (Accessed: 1 July 2012).

ISO (2009) *ISO10360-2: Geometrical product specifications (GPS) -- Acceptance and reverification tests for coordinate measuring machines (CMM) -- Part 2: CMMs used for measuring linear dimensions*. International Organization for Standardization.

Jablonski, S., Tarhini, M., Touati, M., Gonzalez Garcia, D. and Alario, J. (2012) 'The Mediterranean Solar Plan: Project proposals for renewable energy in the Mediterranean Partner Countries region', *Energy Policy*, 44, pp. 291–300.

Jaslier, Y. (1995) *Development of EB-PVD TBS's: The role of deposition temperature and plasma assistance*. PhD Thesis. Cranfield University.

Jones, S. (1998) *SAND098-2778C: VSHOT measurements of distal II dish concentrators,*. Sandia National Laboratories, Albuquerque, New Mexico.

Jones, S., Neal, D. and Gruetzner, J. (1996) *SAND96-2272C: VSHOT: a tool for characterizing large, imprecise reflectors*. Sandia National Laboratories, Albuquerque, New Mexico.

Jorgensen, G., Kennedy, C., King, D. and Terwilliger, K. (2000) *NREL/TP-520-28110: Optical Durability Testing of Candidate Solar Mirrors*. National Renewable Energy Laboratory, USA.

Kalogirou, S.A. (2004) 'Solar thermal collectors and applications', *Progress in Energy and Combustion Science*, 30(3), pp. 231–295.

Kearney, D., Herrmann, U., Nava, P., Kelly, B., Mahoney, R., Pacheco, J., Cable, R., Potrovitza, N., Blake, D. and Price, H. (2003) 'Assessment of a Molten Salt Heat Transfer Fluid in a Parabolic Trough Solar Field', *Journal of Solar Energy Engineering*, 125(2), p. 170.

Kennedy, C.E. and Terwilliger, K. (2005) 'Optical Durability of Candidate Solar Reflectors', *Journal of Solar Energy Engineering*, 127(2), p. 262.

Knauer, M.C., Kaminski, J. and Häusler, G. (2004) 'Phase Measuring Deflectometry: a new approach to measure specular free-form surfaces', *Proceedings of SPIE*., Vol.5457, pp. 366–376.

Kuo, H.-W. and Shen, H.-Y. (2010) 'Indoor and outdoor PM2.5 and PM10 concentrations in the air during a dust storm', *Building and Environment*, 45(3), pp. 610–614.

Labsphere (2013) *Spectralon Targets*. Available at: http://www.labsphere.com/products/reflectance-standards-and-targets/reflectance-targets/spectralon-targets.aspx (Accessed: 1 July 2013).

Leitz (2012) *Leitz PMM-F 30.20.10/16*. Available at: http://www.leitz-metrology.com/leitz-pmm-f-30201016_544.htm (Accessed: 1 February 2012).

Li, X. and Zhang, H. (2012) 'Seasonal variations in dust concentration and dust emission observed over Horqin Sandy Land area in China from December 2010 to November 2011', *Atmospheric Environment*, 61, pp. 56–65.

López-Martín, R., Caron, S., Sutter, F., Meyen, S. and Fernández-García, A. (2011) 'Accelerated aging of solar reflectors under sandstorm conditions', *Proceedings of SolarPACES 2011*. Granada, Spain, 20-23 September 2011.

Lupfert, E., Geyer, M., Schiel, W. and Esteban, A. (2001) 'Eurotrough design issues and prototype testing at PSA', *Proceedings of Solar Forum 2001 - Solar Energy: The Power to Choose*. Washington, DC, USA, 21-25 April 2001.

Lüpfert, E. and Ulmer, S. (2009) 'Solar trough mirror shape specifications', *Proceedings of SolarPACES 2009*. Berlin, Germany, 15-18 September 2009.

Madjoubi, M. and Bousbaa, C. (1998) ‘Effects of duration of sand blasting on the properties of window glass’, *Glass Technology*, 39(1), pp. 24–26.

Mahavar, S., Sengar, N., Rajawat, P., Verma, M. and Dashora, P. (2012) ‘Design development and performance studies of a novel Single Family Solar Cooker’, *Renewable Energy*, 47, pp. 67–76.

März, T., Prahl, C., Ulmer, S., Wilbert, S. and Weber, C. (2011) ‘Validation of Two Optical Measurement Methods for the Qualification of the Shape Accuracy of Mirror Panels for Concentrating Solar Systems’, *Journal of Solar Energy Engineering*, 133(3), p. 031022.

Meyen, S., Lüpfert, E., Kennedy, C. and Fernández-García, A. (2010) ‘Standardization of Solar Mirror Reflectance Measurements – Round Robin Test’, *Proceedings of SolarPACES 2010*. Perpingnan, France, 21-24 September 2010.

Meyen, S., Lüpfert, E., Pernpeintner, J. and Fend, T. (2009) ‘Optical Characterization of Reflector Material for Concentrating Solar Power Technology’, *SolarPACES 2009*. Berlin, Germany. Available at: http://elib.dlr.de/61681/1/Paper-Optical-Characterisation.pdf (Accessed: 15 September 2008).

Molnar, A., Hu, J., Cosgrove, D., Tilstra, A., Chen, D., Gray, A., Wendelin, T. and Reynolds, G. (2011) ‘A novel VSHOT geometry for the characterization of large mirror-film based panelized reflectors’, *Proceedings of SolarPACES 2011*. Granada, Spain, 20-23 September 2011.

NASA (2013) *Sun Fact Sheet*. Available at: http://nssdc.gsfc.nasa.gov/planetary/factsheet/sunfact.html (Accessed: 1 August 2012).

Nixon, J.D., Dey, P.K. and Davies, P.A. (2010) ‘Which is the best solar thermal collection technology for electricity generation in north-west India? Evaluation of options using the analytical hierarchy process’, *Energy*, 35(12), pp. 5230–5240.

Panwar, N.L., Kaushik, S.C. and Kothari, S. (2012) ‘State of the art of solar cooking: An overview’, *Renewable and Sustainable Energy Reviews*, 16(6), pp. 3776–3785.

Pappa, R., Jones, T., Black, J. and Walford, A. (2002) ‘*AIAA-2002-1375: Photogrammetry methodology development for gossamer spacecraft structures*’, NASA Langley Research Center, USA.

Pappa, R.S., Jones, T.W. and Black, J.T. (2002) ‘Photogrammetry methodology for gossamer spacecraft structures’, *Sound and Vibration*, 36(8), pp. 12–21.

Patlitzianas, K.D. (2011) ‘Solar energy in Egypt: Significant business opportunities’, *Renewable Energy*, 36(9), pp. 2305–2311.

Pettit, R. and Freese, J. (1980) ‘Wavelength dependent scattering caused by dust accumulation on solar mirrors’, *Solar Energy Materials*, 3, pp. 1–20.

Pitz-Paal, R., Botero, N.B. and Steinfeld, A. (2011) ‘Heliostat field layout optimization for high-temperature solar thermochemical processing’, *Solar Energy*, 85(2), pp. 334–343.

Pottler, K., Lüpfert, E., Johnston, G.H.G. and Shortis, M.R. (2005) ‘Photogrammetry: A Powerful Tool for Geometric Analysis of Solar Concentrators and Their Components’, *Journal of Solar Energy Engineering*, 127(1), p. 94.

Pottler, K. and Shortis, M.R. (2004) ‘Photogrammetry: A Powerful tool for geometric analysis of solar concentrators and their components’, *ISEC*. Portland, Oregon: ASME, pp. 1–8.

Prahl, C., Stanicki, B., Hilgert, C., Ulmer, S. and Röger, M. (2013) ‘Airborne shape measurement of parabolic trough collector fields’, *Solar Energy*, 91, pp. 68–78.

ProtermoSolar (2014) *Map of the solar thermal industry in Spain*. Available at: http://www.protermosolar.com/proyectos-termosolares/mapa-de-proyectos-en-espana/ (Accessed: 1 September 2014).

Quaschning, V. and Muriel, M.B. (2001) ‘Solar power-photovoltaics or solar thermal power plants?’, *Proceedings of VGB Congress Power Plants*. Brussels, Belgium, 10-12 October 2001.

Ronda High Tech (2012) *Accompanying booklet to mirror panels*.

Rybicki, G. and Lightman, A. (2008) *Radiative processes in astrophysics*. New York: Wiley.

Schnatbaum, L. (2009) ‘Solar thermal power plants’, *The European Physical Journal Special Topics*, 176(1), pp. 127–140.

Schott Solar (2012) *Schott PTR 70 Receiver*. Available at: http://www.schottsolar.com/global/products/concentrated-solar-power/schott-ptr-70-receiver/ (Accessed: 20 September 2012).

Shortis, M., Clarke, T. and Short, T. (1994) ‘A comparison of some techniques for the subpixel location of discrete target images’, *Videomatrics III. SPIE*, 2350, pp. 239–250.

Shortis, M. and Johnston, G. (1997) ‘Photogrammetry: An Available Surface Characterization Tool for Solar Concentrators, Part II: Assessment of Surfaces’, *Journal of Solar Energy Engineering*, 119(4), p. 286.

Shortis, M.R., Johnston, G.H.G., Pottler, K., Lüpfert, E. and Commission, V. (2008a) ‘Photogrammetric Analysis of Solar Collectors’, *The International Archives of the Photogrammetry, Remote Sensing and Spatial Information Sciences*, 37(B5) Beijing, pp. 81–88.

Shortis, M.R., Robson, S., Jones, T.W. and Lunsford, C.B. (2007) ‘Parachute model validation using image sequences’, *Eighth Conference on Optical 3-D Measurement Techniques*. Zurich, Switzerland, July 2007.

Shortis, M.R., Seager, J.W., Williams, A., Barker, B.A. and Sherlock, M. (2008b) ‘Using Stereo-Video for Deep Water Benthic Habitat Surveys’, *Marine Technology Society Journal*, 42(4), pp. 28–37.

Snidvongs, S. (2012) ‘Compact Linear Fresnel Reflector with Hydrogen from Water and Garbage in Medium Insolation, Hot and Humid Climate’, *Proceedings of SolarPACES 2012*. Marrakech, Morocco, 11-14 September 2012.

Solar Millennium (2012) *The Construction of the Andasol Power Plants*. Available at: http://www.solarmillennium.de/english/archives/technology/references-and-projects/andasol-spain/index.html (Accessed: 1 October 2012).

SolarGIS (2014) *Solar Radiation Maps*. Available at: http://solargis.info/doc/_pics/freemaps/1000px/dni/SolarGIS-Solar-map-DNI-World-map-en.png (Accessed: 1 September 2014).

Sowelim, M. a. (1983) ‘Characteristics of storm deposited dust at Cairo’, *Atmospheric Environment*, 17(1), pp. 145–149.

Stynes, J. and Ihas, B. (2012) ‘Slope Error Measurement Tool for Solar Parabolic Trough Collectors’, *Proceedings of the 2012 World Renewable Energy Forum*. Denver, Colorado, USA, 13-17 May 2012.

Taggart, S. (2008) ‘CSP: dish projects inch forward’, *Renewable Energy Focus*, 9(4), pp. 52–54.

Tahboub, Z.M., Dahleh, B. and Goebel, O. (2012) ‘Solar Mirrors Soiling Campaign – Abu Dhabi’, *Proceedings of SolarPACES 2012*. Marrakech, Morocco, 11-14 September 2012.

Taketani, H. (1980) ‘Reflectance and aging studies of heliostat mirrors’, *Solar Energy Materials*, 3, pp. 127–134.

Thalib, L. and Al-Taiar, A. (2012) ‘Dust storms and the risk of asthma admissions to hospitals in Kuwait’, *Science of The Total Environment*, 433, pp. 347–351.

Torresol Energy (2012) *Gemasolar*. Available at: http://www.torresolenergy.com/TORRESOL/gemasolar-plant/en (Accessed: 1 June 2013).

Trieb, F., Müller-Steinhagen, H. and Kern, J. (2011) ‘Financing concentrating solar power in the Middle East and North Africa—Subsidy or investment?’, *Energy Policy*, 39(1), pp. 307–317.

Trieb, F., Schillings, C., Pregger, T. and O’Sullivan, M. (2012) ‘Solar electricity imports from the Middle East and North Africa to Europe’, *Energy Policy*, 42, pp. 341–353.

Tsikalakis, A., Tomtsi, T., Hatziargyriou, N.D., Poullikkas, A., Malamatenios, C., Giakoumelos, E., Jaouad, O.C., Chenak, A., Fayek, A., Matar, T. and Yasin, A. (2011) ‘Review of best practices of solar electricity resources applications in selected Middle East and North Africa (MENA) countries’, *Renewable and Sustainable Energy Reviews*, 15(6), pp. 2838–2849.

Ulmer, S., Heinz, B., Pottler, K. and Lüpfert, E. (2009) ‘Slope Error Measurements of Parabolic Troughs Using the Reflected Image of the Absorber Tube’, *Journal of Solar Energy Engineering*, 131(1), p. 011014.

Ulmer, S., Pottler, K., Lüpfert, E. and Röger, M. (2007) ‘Measurement Techniques for the Optical Quality Assessment of Parabolic Trough Collector Fields in Commercial Solar Power Plants’, *Proceedings of ES2007, Energy Sustainability*. Long Beach, California, USA, 27-30 June 2007.

US-DOD (2008) *Mil-STD-810G: Department of Defense Test Method Standard for Environmental Engineering Considerations and Laboratory Tests*. United States Department of Defense.

Wada, S. and Watanabe, N. (1987) ‘Solid Particle Erosion of Brittle Materials (Part 3)’, *Journal of the Ceramic Association, Japan*, 95(6), pp. 573–578.

Wendelin, T.J., May, K. and Gee, R. (2006) ‘Video Scanning Hartmann Optical Testing of State-of- the-Art Parabolic Trough Concentrators’, *Proceedings of the Solar 2006 Conference*. Denver, Colorado, USA, 8-13 July 2006.

Wolfram MathWorld (2013) *Parabolic segment*. Available at: http://mathworld.wolfram.com/ParabolicSegment.html (Accessed: 1 August 2013).

World Bank (2012a) *MA-Ouarzazate Concentrated Solar Power*. Available at: http://www.worldbank.org/projects/P122028/ma-ouarzazate-concentrated-solar-power?lang=en (Accessed: 28 September 2012).

World Bank (2012b) *Kom Ombo Solar Power*. Available at: http://www.worldbank.org/projects/P120191/kom-ombo-solar-power?lang=en (Accessed: 28 September 2012).

World Bank (2012c) *TN STEG Concentrated Solar Power*. Available at: http://www.worldbank.org/projects/P122029/tn-steg-concentrated-solar-power?lang=en (Accessed: 28 September 2012).

Wu, D., Wang, S., Xia, J., Meng, X., Shang, K., Xie, Y. and Wang, R. (2013) 'The influence of dust events on precipitation acidity in China', *Atmospheric Environment*, 79, pp. 138–146.

Xiao, J., Wei, X., Lu, Z., Yu, W. and Wu, H. (2012) 'A review of available methods for surface shape measurement of solar concentrator in solar thermal power applications', *Renewable and Sustainable Energy Reviews*, 16(5), pp. 2539–2544.

Yates, B.W. and Duffy, A.M. (2008) 'Statistical Analysis of the Metrological Properties of Float Glass', *Proceedings of SPIE*, 7077, p. 70770D–70770D–11.

Zhao, M., Zhan, K., Yang, Z., Fang, E., Qiu, G., Wang, Q., Zhang, Y., Guo, S., Li, A. and Zhang, J. (2011) 'Characteristics of the lower layer of sandstorms in the Minqin desert-oasis zone', *Science China Earth Sciences*, 54(5), pp. 703–710.

Zhao, W. (2009) 'Testing an aspheric mirror based on phase measuring deflectometry', *Optical Engineering*, 48(10), p. 103603.

APPENDIX

A.1 MATLAB code

This section details some of the custom developed MATLAB algorithms and code used in the analysis of the point clouds and production of the figures and data found in the thesis.

A.1.1 Photogrammetry repeatability

```
% Repeatability for photogrammetry repeats

%% Load repeat data
filename = 'repeat1.txt';
points = importdata(filename);
assignin('base', 'points_pg_r1', points);

filename = 'repeat2.txt';
points = importdata(filename);
assignin('base', 'points_pg_r2', points);

filename = 'repeat3.txt';
points = importdata(filename);
assignin('base', 'points_pg_r3', points);

filename = 'repeat4.txt';
points = importdata(filename);
assignin('base', 'points_pg_r4', points);

filename = 'repeat5.txt';
points = importdata(filename);
assignin('base', 'points_pg_r5', points);

pg1=points_pg_r1; % set first repeat as baseline

%% calculate departure maps of each repeat from baseline
pg2=pg_precision(points_pg_r1,points_pg_r2);
pg3=pg_precision(points_pg_r1,points_pg_r3);
pg4=pg_precision(points_pg_r1,points_pg_r4);
pg5=pg_precision(points_pg_r1,points_pg_r5);

%% combine departures for x,y,z directions
pg_allx=[pg1(:,1) pg2(:,1) pg4(:,1) pg5(:,1)];
pg_ally=[pg1(:,2) pg2(:,2) pg4(:,2) pg5(:,2)];
pg_allz=[pg1(:,3) pg2(:,3) pg4(:,3) pg5(:,3)];

%% calculate standard deviations for x,y,z and vector distances
SX=std(pg_allx,0,2);
SY=std(pg_ally,0,2);
SZ=std(pg_allz,0,2);
SD = sqrt(SX.^2+SY.^2+SZ.^2);
```

```
%% calculate average coordinates over all repeats
X=mean(pg_allx,2);
Y=mean(pg_ally,2);
Z=mean(pg_allz,2);
%% remove some extra points
X(543)=[];X(542)=[];X(55)=[];
Y(543)=[];Y(542)=[];Y(55)=[];
Z(543)=[];Z(542)=[];Z(55)=[];
SD(543)=[];SD(542)=[];SD(55)=[];
SZ(543)=[];SZ(542)=[];SZ(55)=[];
SX(543)=[];SX(542)=[];SX(55)=[];
SY(543)=[];SY(542)=[];SY(55)=[];

%% plot results
ft = 'linearinterp';
opts = fitoptions( ft );
opts.Weights = zeros(1,0);
opts.Normalize = 'on';
[fitresult, gof] = fit( [X, Y], SZ, ft, opts );

% Plot fit with data.
figure( 'Name', 'untitled fit 1' );
plot( fitresult, [X, Y], SZ );
% Label axes
xlabel( 'X' );
ylabel( 'Y' );
zlabel( 'SZ' );
title( 'Photogrammetry standard deviation (mm)');
set_figure;

%% calculate RMS departure values
SX_RMS=sqrt(sumsqr(SX)/size(SX,1));
SY_RMS=sqrt(sumsqr(SY)/size(SY,1));
SZ_RMS=sqrt(sumsqr(SZ)/size(SZ,1));
SD_RMS=sqrt(sumsqr(SD)/size(SD,1));
%%%%%%%%%%%%%%%%%%%%%%%%%%%%%%%%%%%%%%%%%%%%%%%%%%%%%%%%%%%%%%%%%%%%%%%
```

Figure A.1 - Photogrammetry repeatability code

The function `pntsf=pg_precision(pnts1,pnts2)` takes the point cloud `pnts2` and aligns it to `pnts1` by rotation and translation. The resulting aligned point cloud is returned to `pntsf`. The function `set_figure` is a custom function to set parameters of the plot.

A.1.2 CMM repeatability

```
% Repeatability for CMM repeats

%% custom function that translates the cmm data file to a points
matrix
points=import_cmm;
```

```
%% loop through repeats to assign repeats to separate variables and
apply a radius correction
for i=3:10

    m=598*(i-1)+1;
    n=598*i;
    eval([ 'cmm' num2str(i) '=points(m:n,:);']);
    eval(['cmm=cmm' num2str(i) ';' ]);
    cmm(:,1:3)=cmm(:,1:3)-4*cmm(:,4:6);
    eval(['cmmRC' num2str(i) '=cmm;' ]);

end

X=[];
Y=[];
Z=[];
%% place coordinates of repeats in separate x,y,z matrices
for i=3:10

    eval([ 'X=[X cmmRC' num2str(i) '(:,1)];']);
    eval([ 'Y=[Y cmmRC' num2str(i) '(:,2)];']);
    eval([ 'Z=[Z cmmRC' num2str(i) '(:,3)];']);
end

%% calculate standard deviations and RMS of x,y,z across repeats

SX = std(X,0,2);
SY = std(Y,0,2);
SZ = std(Z,0,2);
SD=sqrt(SX.^2 + SY.^2 + SZ.^2);

RMSX=sqrt(sumsqr(SX)/size(SX,1))
RMSY=sqrt(sumsqr(SY)/size(SY,1))
RMSZ=sqrt(sumsqr(SZ)/size(SZ,1))
RMSD=sqrt(sumsqr(SD)/size(SD,1))

%% calculate mean values of x,y,z
MX_cmm=mean(X,2);
MY_cmm=mean(Y,2);
MZ_cmm=mean(Z,2);

% remove outlier values
out=find(abs(SZ)>3*RMSZ);
MX_cmm(out)=[];
MY_cmm(out)=[];
MZ_cmm(out)=[];
SZ(out)=[];
SD(out)=[];

%% plot results
ft = 'linearinterp';
opts = fitoptions( ft );
opts.Weights = zeros(1,0);
opts.Normalize = 'on';
[fitresult, ~] = fit( [MX_cmm, MY_cmm], SZ, ft, opts );

% Plot fit with data.
```

```
figure( 'Name', 'CMM repeatability' );
h = plot( fitresult, [MX_cmm, MY_cmm], SZ );
% Label axes
xlabel( 'MX' );
ylabel( 'MY' );
zlabel( 'SZ' );
title( 'Repeatability SZ RMS');
set_figure;
daspect([1 1 0.001]);
%%%%%%%%%%%%%%%%%%%%%%%%%%%%%%%%%%%%%%%%%%%%%%%%%%%%%%%%%%%%%%%%%%%%%%%
```

Figure A.2 - CMM repeatability code

A.1.3 PG/CMM correlation

This flow chart shows the process for the comparison of a photogrammetry (PG) measurement against measurement done by the coordinate measuring machine (CMM). The PG points are sorted into columns of increasing x and y to enable a proper interpolation to occur. The PG points are interpolated onto the CMM x, y coordinates to allow a subtraction in the z-direction. The resulting difference is plotted and the RMS difference found.

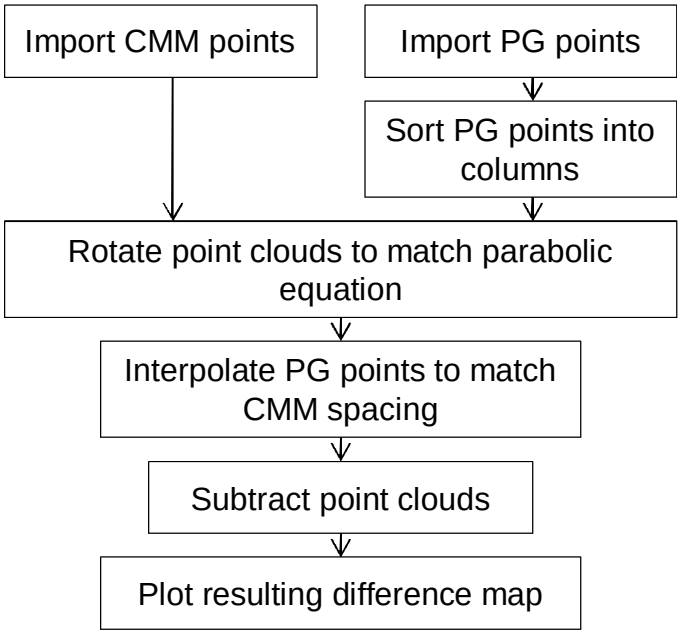

Figure A.3 - Photogrammetry / CMM correlation flow

A.1.4 On-site Measurements

The description below details the program for the ENEA measurements. The EuroTrough measurements follow the same procedure, with minor modifications to allow for the design difference between the mirrors.

```
%% ENEA measurements

%% point clouds loaded for each mirror and for the combined points
points1=load('enea_1.txt');
points2=load('enea_2.txt');
points3=load('enea_3.txt');
pointsA=load('merged2.txt');

%% point clouds rotated by 32.19 deg to match parabolic equation
points1_r = rotat(points1, -32.19,0,0);
points2_r = rotat(points2, -32.19,0,0);
points3_r = rotat(points3, -32.19,0,0);
pointsA_r = rotat(pointsA, -32.19,0,0);

%% outlier points identified and stored
out1=rm_out(points1_r);
out2=rm_out(points2_r);
out3=rm_out(points3_r);
outA=rm_out(pointsA_r);

%% error maps plotted excluding identified outliers
plot_m(points1_r,1,out1);
plot_m(points2_r,1,out2);
plot_m(points3_r,1,out3);
plot_m(pointsA_r,1,outA);

%% point clouds interpolated and slope errors found
%% ray tracing is also performed and intercept factors found.
slope_interp(points1);
slope_interp(points2);
slope_interp(points3);
slope_interp(pointsA);
%%%%%%%%%%%%%%%%%%%%%%%%%%%%%%%%%%%%%%%%%%%%%%%%%%%%%%%%%%%%%%%%%%%%%%%%%%%
```

Figure A.4 - ENEA on-site measurement code

`rotat` is a custom function that rotates the point clouds by 32.19 degrees according to the design specification such that the cloud aligns with the parabolic equation.

`rm_out` is a custom function that fits a second order polynomial to the point cloud. Points with residuals greater than twice the RMS residual value are identified as outlier points, keeping greater than 90% of the points.

`plot_m` is a custom function that finds the difference between the point cloud and the parabolic equation then separates the form from the underlying errors by fitting a second order polynomial. This results in the form error maps and the form removed error maps.

`slope_interp` is a custom function that interpolates the point cloud to a regular grid then calculates the slope between sets of adjacent points. This calculated slope is then compared to the slope from the parabolic equation and the difference found. Additionally within this function are the `ray_trace` and `defocus_abs` functions.

`ray_trace` is a custom function that takes the slope values calculated previously and assuming vertical incoming light rays calculates the direction the light would reflect. This is then plotted along with the ideal position of the absorber tube.

`defocus_abs` takes the rays previously calculated and finds the closest distance that the ray passes the centre of the absorber tube. When this distance is less than the radius of the absorber tube, the ray can be said to strike the absorber. By counting the number of rays striking the absorber tube against the total number traced, an intercept factor is found.

A.2 Climate data

Shown in Figure A.5 is example raw data for Borg El-Arab airport on 22nd January 2012, which may be downloaded from the Wunderground.com website. Data given are the temperature, dew point, humidity, pressure, visibility, wind direction, wind speed, gust speed, precipitation, conditions, wind direction in degrees and the date-time.

http://www.wunderground.com/history/airport/HEBA/2012/1/22/DailyHistory.html?format=1

TimeEET,TemperatureC,Dew PointC,Humidity,Sea Level PressurehPa,VisibilityKm,Wind Direction,Wind SpeedKm/h,Gust SpeedKm/h,Precipitationmm,Events,Conditions,WindDirDegrees,DateUTC
12:00 AM,8.0,3.0,71,1019,-9999.0,SSW,11.1,-,N/A,,Clear,200,2012-01-21 22:00:00
1:00 AM,10.0,3.0,62,1019,-9999.0,SW,14.8,-,N/A,,Clear,230,2012-01-21 23:00:00
2:00 AM,9.0,3.0,66,1018,-9999.0,SW,14.8,-,N/A,,Clear,230,2012-01-22 00:00:00
3:00 AM,9.0,2.0,62,1017,-9999.0,WSW,22.2,-,N/A,,Clear,240,2012-01-22 01:00:00
5:00 AM,9.0,2.0,62,1016,-9999.0,SW,22.2,-,N/A,,Clear,230,2012-01-22 03:00:00
8:00 AM,11.0,3.0,58,1015,6.0,WSW,35.2,-,N/A,,Scattered Clouds,240,2012-01-22 06:00:00
9:00 AM,11.0,6.0,71,1015,4.0,WSW,27.8,-,N/A,,Sand,250,2012-01-22 07:00:00
10:00 AM,12.0,9.0,82,1017,4.0,West,29.6,-,N/A,,Sand,260,2012-01-22 08:00:00
11:00 AM,12.0,12.0,100,1016,6.0,West,31.5,-,N/A,,Scattered Clouds,270,2012-01-22 09:00:00
12:00 PM,14.0,11.0,82,1016,6.0,NW,33.3,-,N/A,,Scattered Clouds,310,2012-01-22 10:00:00
2:00 PM,16.0,9.0,63,1016,10.0,WNW,33.3,-,N/A,,Scattered Clouds,300,2012-01-22 12:00:00
3:00 PM,16.0,6.0,52,1017,10.0,WNW,38.9,-,N/A,,Scattered Clouds,300,2012-01-22 13:00:00
4:00 PM,15.0,6.0,55,1017,10.0,WNW,31.5,-,N/A,,Scattered Clouds,300,2012-01-22 14:00:00
8:00 PM,13.0,6.0,63,1019,10.0,NW,16.7,-,N/A,,Scattered Clouds,310,2012-01-22 18:00:00
10:00 PM,12.0,6.0,67,1020,10.0,WNW,11.1,-,N/A,,Scattered Clouds,300,2012-01-22 20:00:00
11:00 PM,11.0,7.0,76,1020,10.0,WNW,7.4,-,N/A,,Scattered Clouds,290,2012-01-22 21:00:00

Figure A.5 - Example data from website

Figure A.6 shows the normalised distribution of the wind directions both with and without sandstorms indicating that during sandstorms the predominant wind direction is from the west. This means that the source of the sand is the Sahara desert, which is located to the west of Alexandria.

Figure A.7 shows the distribution of the durations of sandstorm events at Borg El-Arab, during 2012-2013. This shows that the most common duration is 4 hours of sandstorm.

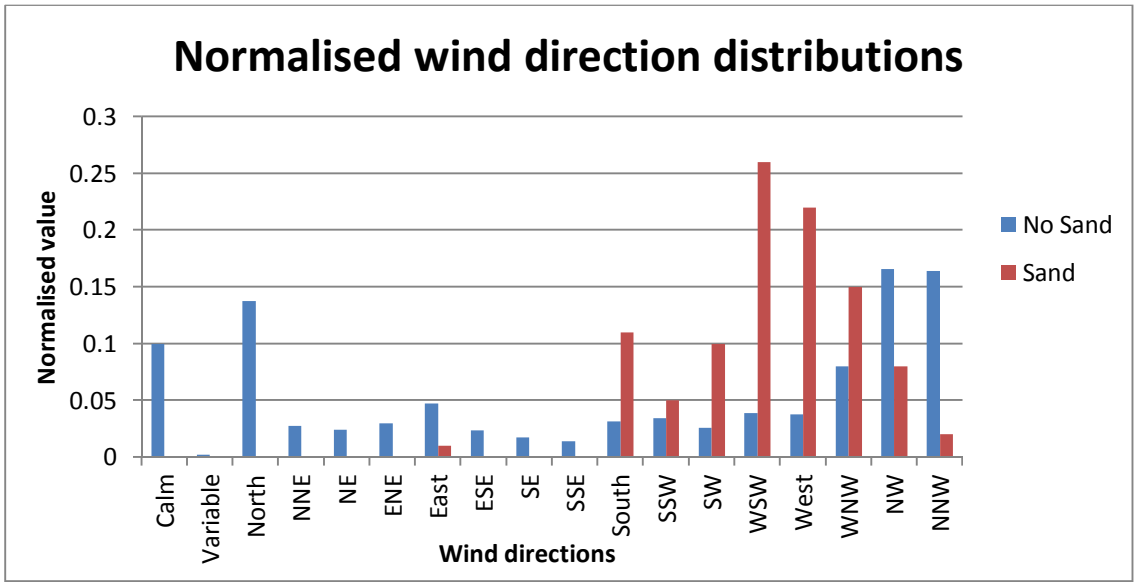

Figure A.6 - Wind direction distribution

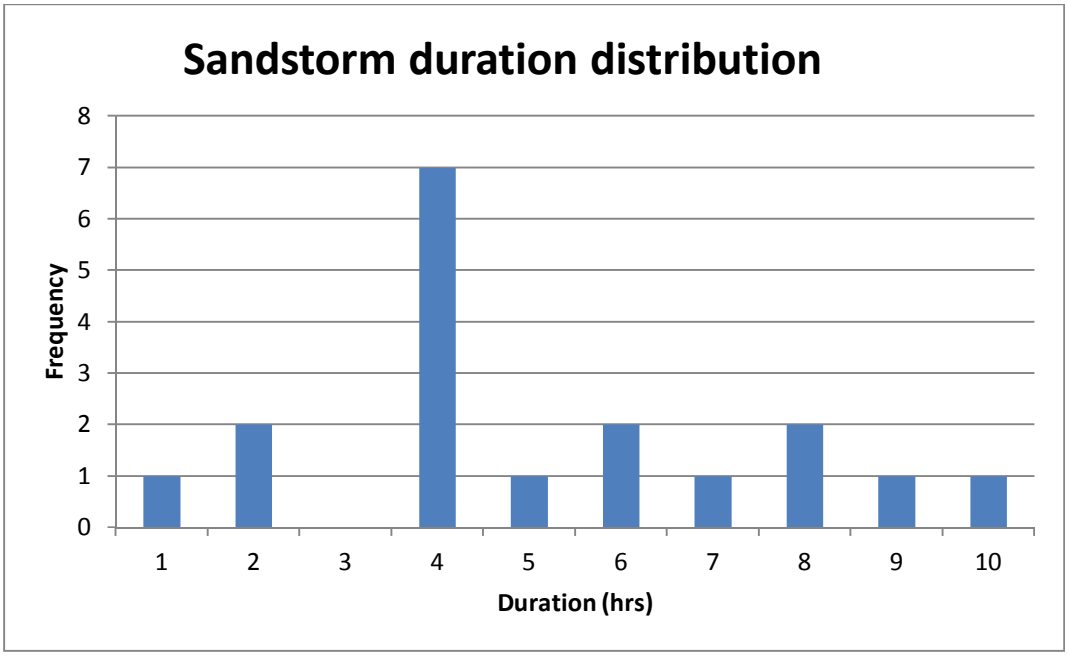

Figure A.7 - Distribution of sandstorm durations